Investigating the evolution of fault scarps in jointed volcanic rock through field evidence, morphometric techniques and novel methods

Cassandra Brigham

A dissertation

submitted in partial fulfillment of the

requirements for the degree of

Doctor of Philosophy

University of Washington

2023

Reading Committee:

Juliet G. Crider, Chair

Alison R. Duvall

John Stone

Program Authorized to Offer Degree:

Earth and Space Sciences

University of Washington

Abstract

Investigating the evolution of fault scarps in jointed volcanic rock through field evidence, morphometric techniques and novel methods

Cassandra Brigham

Chair of the Supervisory Committee:
Dr. Juliet G. Crider
Earth and Space Sciences

The morphology of fault scarps in jointed volcanic rock records information on the tectonics, volcanism and geomorphology of a region. The evolution of scarp form has been modeled to extract information varying from the age of faulting events and the recurrence time between earthquakes to variations in erosion rates between glacial cycles in other lithologies, but no similar model exists for jointed volcanic rock. In this thesis, I investigate the evolution of fault scarps in jointed volcanic rock. In chapter 2, I present field observations and synthesize previous work on fault scarps in jointed volcanic rock to produce a conceptual framework based on the along-strike variation in profile form through time depending on process. In chapter 3, I quantify the along-strike variations in profile form by defining morphologic classes, using a supervised learning algorithm to automatically classify profiles. I define the "morphologic variability metric" which calculates the number of classes and their proportions in a moving window along a fault scarp. In chapter 4, I apply the morphologic variability metric to a controlled experiment in which a single-age scarp cuts three lithologies and show that the metric reports different variability values along the scarp for each lithologic unit. In chapter 5, I adapt

the metric to increase its suitability for large datasets and explore the most appropriate use cases and statistical methods with which to use it depending on the scale of the analysis.

TABLE OF CONTENTS

LIST OF FIGURES

LIST OF TABLES

ACKNOWLEDGEMENTS

Many mentors, collaborators, colleagues, friends and family members made the journey of this dissertation possible with support, guidance, encouragement, and laughter when I needed it the most. I would first like to acknowledge my advisor, Juliet Crider, for guiding me into the world of fault scarps and giving me the intellectual freedom to pursue many divergent avenues, all the while keeping me grounded in a field-based, observation-rich approach. Thank you to the members of my committee: Alison Duvall, John Stone and Ben Marwick. Thank you to Alison Duvall and Ben Marwick for their thoughtful feedback on the manuscript of Chapter 3 before publication.

Thanks to Robert Craddock, who provided support for two incredible seasons of fieldwork in Hawai'i and mentorship during an NSF internship at the National Air and Space Museum, all based on a very serendipitous encounter at GSA. Thanks to Chelsea Scott, who invited me to participate in her field season in the Volcanic Tablelands back in 2018 based on our shared interest in scarps, photogrammetry and Carleton College, which has lead to years of her mentorship, a fruitful collaboration and a wonderful friendship. Thanks to Owen Callahan for welcoming me as warmly as the Nevada desert heat in June onto his ongoing project and the fun and supportive collaboration that has come of it.

I have been very fortunate in my company out in the field and I would like to acknowledge all of my amazing field assistants: Ayla Heinze Fry and Peter Ingram (Iceland); Emma Kahle and Karen Brigham (Modoc Plateau) and Megan Mueller (Hawai'i).

To my ESS community, I am grateful for the supportive environment among the graduate students, the faculty and the staff and the life-long friendships that I have developed throughout the years.

Thanks to my parents, my grandfather, Fabienne, Christian, and all of my family for fostering my curiosity of the world and encouraging me along this path. Thank you, Jackson, for making the hard things bearable and the bearable things a true joy.

This work was funded by a National Science Foundation Graduate Research Fellowship, awards from the department of Earth and Space Sciences (University of Washington), a grant from the Quaternary Research Center (University of Washington) and a Graduate Research Grant from the Geological Society of America.

CHAPTER 1: INTRODUCTION

Fault scarps are steps in the landscape created by surface-rupturing faults and subsequently modified by geomorphic processes. The frequent coupling of volcanic activity and tectonic extension means that many fault scarps on Earth are in jointed volcanic rock, be it at divergent plate boundaries, back-arc basins, continental rifts or other zones of crustal extension. Fault scarps in volcanic rock have also been identified on other planetary bodies, including the Moon, Mars and Mercury. The evolution of scarp form has been modeled to extract information varying from the age of faulting events and the recurrence time between earthquakes (e.g., Mattson & Bruhn, 2001) to variations in erosion rates between glacial cycles (e.g., Tucker et al., 2011). Studies have described and simulated the degradation of small fault scarps in poorly consolidated Quaternary sediment (e.g. Wallace, 1977; Bucknam & Anderson, 1979; Nash, 1980; Hanks, 2000) as well as the changes with time in roughness of the fault slip surface preserved on fault scarps in limestone (e.g., Stewart, 1996; Stahl & Tye, 2020; Zielke et al., 2022; Tesson & Benedetti, 2019). Despite the common occurrence of fault scarps in volcanic rock, there is no comparable literature on these landforms.

In this thesis, I investigate the evolution of fault scarps in jointed volcanic rock. In chapter 2, I present field observations from seventeen fault scarps in jointed volcanic rock from five sites in Iceland, California and Hawaii. The sites have different rock mass characteristics, fault slip rates, fault zone structure, types and rates of volcanism, climatic conditions and ages. Field observations include rock and rock mass characteristics, joint distribution, fault structure, vegetation and evidence for weathering, rock topple, hillslope processes or other geomorphic modification. I collected low-elevation aerial photography to produce high-resolution digital topography along

these scarps, resulting in a dataset that includes high-density point clouds, orthophotograph mosaics, three-dimensional mesh models and DEMs. I systematically review the current state of the literature on the factors that govern fault scarp form in jointed bedrock along three main axes: rock mass characteristics, fault structures and modification processes (volcanic and geomorphic), and I present my observations in the context of this prior work.

To produce a conceptual model for the degradation of fault scarps in jointed volcanic rock equivalent to those in alluvium or limestone, I look at a single profile of a simple shared geometry (a free face) and determine which processes are shared between scarps of equivalent scale. I find that rock mass characteristics coupled with the frequency of rockfall are the most important factors in determining final scarp form. As the scarp evolves, rockfall ceases and mechanical, then chemical, weathering will break down the fallen blocks and smooth profile form. This simple conceptual model does not adequately reflect the broad array of forms and processes that I observed in the field, however. The complexity of these landforms and their evolution include: an initial profile form that varies along strike; continued growth events which simultaneously trigger rockfall and interactions between scarps and volcanic flows. I illustrate this complexity with summary diagrams of the evolution of a generic fault scarp in each of the field areas, incorporating the variations in geometry and the site-specific processes that I observed.

I suggest that patterns in scarp profile form, rather than a single profile, may better reveal which processes influence scarp form at a given stage of evolution and how the forms and processes change as the scarp evolves. I thus develop a whole-scarp conceptual model based on its along-strike variation in profile form (or morphologic variability) through time. Initial variation in scarp profile form is governed primarily by fault structures and secondarily by rock mass characteristics. Rockfall and small-scale sliding then concentrate in areas where structures have

made the scarp more unstable, first increasing, then decreasing morphologic variability, as rockfall buries the initial structures. Talus processes and mechanical and chemical weathering smooth profile form and decrease the scarp's overall morphologic variability. If scarps continue to grow, heterogeneity can be introduced again with mass wasting events. Throughout the lifetime of the scarp, volcanic activity can decrease or increase morphologic variability. Furthermore, the ratio of fault slip rate to volcanic resurfacing rate sets the maximum height that the scarp can attain, which has implications for the types of processes that can be active upon it, its structure, and its form.

My conceptual models of fault scarp growth in jointed bedrock highlight the variety of factors that determine scarp form and the complexity of their relationship to each other. The scarps do not record a single process like diffusion or roughening, as scarps in alluvium or limestone do; so it is more challenging to connect scarp form to scarp age. However, a path forward is possible with an understanding that dominant modification processes tend to change with time in scarps in jointed volcanic bedrock, and that patterns in profile form change with these dominant processes. By taking a data-first approach, I argue that the along-scarp complexity can be leveraged to untangle dominant process, and thus evolutionary stage.

In chapter 3 (Brigham and Crider, 2022), I develop a methodology to quantify variations in profile form and define a "morphologic variability metric." I first identify six morphologic categories defined through my observations of common forms across scarps in chapter 2. Then I use machine learning to train and apply an automated classifier to hundreds of fault-normal scarp profiles extracted from the digital topographic data I produced. Principal component analysis with singular value decomposition, a data-reduction technique, is used to quantitatively define the distinctions among the morphologic classes on a training data set that I manually classified. A supervised learning algorithm, the support vector machine (SVM) method, classifies the remaining

profiles. Classification performance was assessed using 5-fold cross validation (81% accuracy) and with independent test data (80% accuracy). Finally, I define a morphologic variability metric and calculate it by determining the number of classes represented and the standard deviation of their proportions in a moving window along the scarp. This metric is then normalized, so that a value of 0 represents a section of scarp where all profiles belong to the same class, and a value of 1 represents a section where all classes are represented in equal proportion. With this tool, I can objectively and reproducibly characterize the variation in profile form along a single scarp. I can also compare the mean morphometric variability among different scarps. This chapter has been published in the journal Geomorphology (Brigham & Crider, 2022).

In chapter 4, I apply the morphologic variability metric to a natural laboratory: fault scarps in geothermal fields provide a chance to run a controlled experiment on how material properties affect scarp form, since hydrothermal alteration and mineral precipitation modify the properties of the host materials over short distances. I present a case study from Dixie Valley, Nevada, where three adjacent units (alluvial and colluvial gravels, quartz-rich hot spring sinter and silicified gravels, and a zone of clay-rich, acid sulfate alteration) are offset by a single Holocene fault rupture. The study site provides the opportunity to apply the morphologic variability metric to a scarp where age and climate are kept constant, but where lithologic characteristics vary substantially between units. This work was done in collaboration with postdoctoral scholar Dr. Owen Calhan (University of Washington). I acquired UAV-flown imagery of the study site which Dr. Callahan used to create a high-resolution DEM and orthophotograph-mosaic. Dr. Callahan also made a detailed map of the hydrothermal deposits and alteration of the site. I documented the morphologies present along the fault scarp in these three units to determine common morphologies to be used in the classification training model, and then ran the morphologic variability tool along

topographic models from scarp sections in each lithology. We find that each lithologic unit has a distinct mean morphologic variability value. The fault scarp in the fumarole-altered section exhibits the lowest morphologic variability, the fault scarp in alluvium and colluvium shows intermediate morphologic variability, and the scarp in sinter and cemented gravel, the most similar to that of jointed bedrock, shows the most variability in form. This controlled experiment shows that the morphologic variability metric changes with lithology and is thus sensitive to parameters such as rock strength and mode of degradation. This work was presented at the Seismological Society of America 2022 Annual Meeting and the 2022 Geothermal Rising Conference.

In chapter 5, I explore generalizing the morphometric variability metric to situations where many more of the parameters are unknown. I return to the question of fault scarps in jointed volcanic rock, probing the relationship between process and form at several scales: a portion of a scarp, a whole scarp, a regional group of scarps and between regional groups. The basic methodology of this study involves taking a measure of scarp form adapted to the scale of the analysis (e.g., profile class, morphologic variability value, scarp mean morphologic variability, regional mean morphologic variability), testing its relationship to a suitably scaled parameter (e.g., vegetation cover, profile height, regional annual precipitation) using an adapted statistical method (e.g., pairwise comparisons, principal component analysis, dominance analysis). Based on the results of these analyses, I develop suggested use cases for the morphologic variability metrics and statistical methods that are meant to guide future workers in understanding the usefulness and limitations of these methods.

This chapter aims to make the morphologic variability metric as generalizable as possible on a wide variety of spatial scales. Given the large increase in the number of profiles (~1.2 k to ~56 k), manual inspection and construction of a training dataset is not feasible, so I adapt the

method in chapter 3 from a supervised learning method to an unsupervised one. I use a pre-trained convolutional neural-network model commonly employed in computer vision problems, VGG16 (Simonyan & Zisserman, 2015), to separate and group profiles in the dataset. I use K-means clustering to separate the profiles into groups of similar form, manually inspecting the first 100 members of each cluster group. Expert decision making comes into play during the selection of the number of classes: I look at results of different number of classes, and once I reach classes that begin to repeat profile types that I consider to be "similar enough" (e.g., forms that are likely the result of the same geomorphic processes), I choose the lower number of classes. I find that this unsupervised approach distinguishes between profiles of different forms using similar standards as my manual classification (e.g., concavity of the slope, number of free faces, aspect ratio of the normalized profile).

Armed with this generalized morphologic variability metric, I tackle the issue of how rock mass characteristics influence scarp form along an Icelandic scarp using data extracted from photogrammetry. Jacyn Schmidt (former Carleton College undergraduate) developed a method to map joint-bounded block facets onto a three-dimensional digital outcrop models. Using this method, she mapped joints exposed in three scarps from my Iceland study sites. From these 3D maps, I extract joint orientation, dimensions and spacing. Using pairwise comparisons between morphologic variability values along the scarp and metrics derived from Schmidt's dataset, I can determine some specific first-order relationships (e.g., variability increases as the range in fracture plane strike increases) with a good degree of confidence. However, obtaining these datasets is very time- and work-intensive, so these studies are by definition local in scale and not easily applicable to other scarps in the region, let alone to other sites.

I continue by computing pairwise correlations between morphologic variability and scarp-specific parameters that I can obtain with remotely sensed datasets (profile height as a proxy for structural position along the scarp and gravitational potential, aspect as a proxy for microclimate, and vegetation cover as measured through the Enhanced Vegetation Index). I find that, given the limited spatial resolution of the measurements that can be gleaned from high-resolution raster datasets and the high amount of variance inherent in a natural system, correlations tend to be weak ($R<0.3$). Using the method of pairwise comparisons, I observe that the relationship between scarp and environmental parameters and morphologic variability at one scarp can be different at another, even within the same site. For example, variations in form correlated negatively to profile height in many scarps, but this relationship was far from universally true.

At the regional scale, I compute summary statistics of the parameters measured along the scarp (e.g., mean variability, maximum scarp height). I use two approaches to examine relationships among parameters: pairwise comparisons of parameters at a single site and principal component analysis to determine primary influence on variance across all sites. I find that fault structure attributes (scarp height and fault length) differentiate between scarps the most, but that morphologic variability and mean EVI account for a significant proportion of variance in the data and are inter-related. I suggest that pairwise comparisons of mean morphologic variability and other scarp parameters between scarps of a single region are a good way to determine potential drivers of scarp evolution at that site, given enough scarps and parameter datasets. On the other hand, principal component analysis is excellent for exploratory analysis, a means to generate hypotheses before collecting data in the field, for example.

At the inter-regional scale, I use dominance analysis to inform how parameters might relate to changes in scarp form. This analysis allows us to see how parameters are inter-related and how

important they are to predicting morphologic variability. I find that the most important parameters relate to vegetation cover and temperature, suggesting that differences in morphologic variability between sites might be related to geomorphic and biologic processes. This implies that more data at sites with differing climates and vegetation profiles is necessary to isolate how scarp form evolves through time. Inter-region dominance analysis of scarp form and a large database of parameters from many regions would be a robust method to extract more universal traits of scarp evolution across different settings and to build a quantitative model of fault scarp evolution in jointed volcanic rock, but essential parameters are likely to be measurable only in the field (e.g., rock mass characteristics), making the construction of such a database difficult work which likely needs to be a community effort, versus the work of an individual researcher.

The point clouds and DEMs that I derived from SfM photogrammetry based on images collected during fieldwork are available at https://doi.org/10.5281/zenodo.7747304. The Jupyter notebooks containing the code used for chapters 3, 4 and 5 are available at https://doi.org/10.5281/zenodo.7747311.

CHAPTER 2: THE MORPHOLOGIC EVOLUTION OF FAULT SCARPS IN JOINTED VOLCANIC ROCK: A SYNTHESIS OF OBSERVATIONS FROM SCARPS IN SOUTHWEST ICELAND, HAWAI'I, AND CALIFORNIA

2.1 INTRODUCTION

Fault scarps are landforms born of both tectonic action and geomorphic modification: to understand one set of processes acting on scarps, it is commonly necessary to constrain the other. Knowing and quantifying the geomorphic processes that affect scarp form can allow researchers to derive important elements of faulting history, such as the total offset, slip rates and recurrence time between earthquakes. If the structural parameters of a scarp are well known (e.g., timing of faulting events, location and dip of fault slip surface, initial dip of a fold limb, depth of a fissure), the characteristics and rates of modification processes can be determined (e.g., rate of talus accumulation, failure slope of mass movements, erosion rates). Scarp-normal profiles integrate both tectonic and geomorphic features into their form. The profiles and how they change (both laterally along the scarp and through time) provides the integrated record of structural and geomorphic evolution of a fault scarp.

Wallace (1977) was one of the first to recognize that the profile form of a fault scarp could provide information on the age of fault activity: he described a sequence of fault scarp degradation for normal faults in alluvium. Normal-fault scarp modification in regolith was further characterized, revealing that slope angles decrease with age and height (Bucknam & Anderson, 1979), and that this change can be modeled by linear hillslope diffusion (e.g. Nash, 1980; Hanks et al., 1984; Andrews & Hanks, 1985), thus providing a basis for morphometric dating of fault scarps. Application of these models has yielded dates of fault initiation, age of faulting events,

rates of movement along faults and recurrence time between earthquakes (e.g., Mattson & Bruhn, 2001). With the advent of high-resolution topographic data, semi-automated methods of morphometrically dating scarps were developed using diffusion models (DeLong et al., 2010; Sare et al., 2019). Tectonic setting and fault zone structure also influence a fault scarp's geomorphic evolution. Fault scarps have been used to study processes such as climate-driven bedrock erosion rates (Tucker et al., 2011), submarine mass wasting (Hughes et al., 2021) or cementation of colluvial sheets (Mason et al., 2017).

Fault scarps in volcanic rock are common on Earth, including Iceland (e.g. Villemin et al., 1994), the East African Rift (e.g. Strecker et al., 1990) and the northwestern Basin and Range (e.g. Pezzopane & Weldon, 1993; Crider, 2001). In these areas, the rock mass characteristics and active volcanism add additional complexity to the evolution of scarp form. The presence of cooling joints precludes describing the geomorphic processes through simple hillslope diffusion or scarp relaxation. Instead, we have to consider both stochastic processes, such as rockfall (e.g., Ayonghe et al., 1999; Ayenew & Barbieri, 2005; Abellán et al., 2011; Rood et al., 2015), and more continuous ones, such as soil-developing physical and chemical weathering processes (e.g., Arnalds, 2004; Rasmussen et al., 2010; Vitousek & Chadwick, 2013; Tangari et al., 2018). Furthermore, certain tectonic structures are more likely to be preserved in jointed rock and strongly influence scarp profile form, such as monoclines (e.g., Macdonald, 1957; Grant & Kattenhorn, 2004; White & Crider, 2006; Smart & Ferrill, 2018). Finally, the interaction of volcanic flows with existing fault scarps can fundamentally alter scarp profile form. Volcanic resurfacing, defined here as the process of complete scarp burial by one or more lava flows, can even erase all traces of scarp growth.

Here, we seek to develop a conceptual model of the morphologic evolution of fault scarps in jointed volcanic bedrock, based on field observations and geospatial analyses of fourteen fault scarps in four regions. We build on existing conceptual models relating to fault growth in volcanic rock (e.g., Grant & Kattenhorn, 2004; Martel & Langley, 2006; Pinzuti et al., 2010; Hardy, 2013; Bubeck et al., 2018) and the interaction between volcanism and faulting (e.g., Holland et al., 2006; Sonnette et al., 2010). Our model considers the relationships among volcanism, faulting and geomorphic modification. We show that the dominant processes that affects scarp profile form, be it tectonic activity, volcanism or geomorphic modification, changes through time and determines the degree of lateral variability along the scarp. Furthermore, the interaction between slip rates and volcanic flow resurfacing and climate are important in determining the factors most influential on scarp form.

2.2 METHODS

In order to characterize the processes acting on fault scarps in tectonically active volcanic settings, we made observations at fault scarps in four settings around the world with varying age, tectonic activity and climate. We used field observations, UAV-acquired imagery, published geologic maps and published Digital Elevation Models (DEMs) with resolution from 0.5 to 10 m^2 to describe the forms of the scarps and infer the processes acting on them. Field observations include fault structure mapping and geomorphic mapping. Scarp form is extracted from bespoke, high-resolution digital elevation models. In this section, we describe our methods for gathering and extracting this information.

2.2.1 Assigning relative ages of scarps in volcanic rocks

Fully determining the age of a fault scarp requires obtaining three pieces of age data: the time of scarp initiation, the time since the last tectonic activity along the scarp and the rate of growth of the scarp. Obtaining these data precisely requires detailed paleoseismic investigations. Here, we instead use the relationship between volcanic flows and fault scarps to bracket scarp ages. First, simple cross-cutting relationships dictate that scarps that cut a single volcanic unit must be younger than that unit. Both the time of scarp initiation and the time since last scarp activity must be younger than the age of that volcanic flow. A minimum rate of scarp growth can be estimated by dividing the maximum scarp height by the volcanic unit age; this rate could be much higher if scarp initiation occurred long after the emplacement of the volcanic unit.

Second, in volcanic settings, scarps may cut multiple units along their length. Comparing the geometry (e.g., number and orientation of fractures) and height of the scarp segments in each of the flows can give information about scarp growth and its relationship with volcanic activity. For example, if scarp segments in older flows are continuous with higher throw and those in younger flows are more segmented with smaller throw, we can infer that scarp initiation in the older flows occurred before emplacement of the younger flows. The geometry of the scarp in the younger unit is thus the result of the underlying fault propagating through the younger unit (e.g. growth model of Sonnette et al., 2010). If scarp initiation had occurred after the deposition of both units, we would expect similar throw and segment geometry in both.

Third, volcanic flows that drape the scarp provide further chronological constraints. If the scarp has cut the draped unit, we can use the age of that unit to set a new maximum time since the last tectonic activity along the scarp. Units that drape the tips of faults scarps are particularly helpful since the tips will most likely record any signs of scarp growth as the fault lengthens. If

the unit is not cut, we can assign a minimum age of scarp initiation. Units that abut the scarp provide similar information. Even if ruptured, an abutting unit will in any case give a maximum age of scarp initiation. If not ruptured, it might provide a minimum age of last episode of scarp growth, depending on the geometry of the unit and the scarp. These gross age constraints allow us to group our field examples by scarp age and relative tectonic activity (Table 1.)

2.2.2 Field work

The goal of the field investigations was to systematically document features of jointed-rock fault scarps in a variety of contexts. At each field site, we made detailed observations of the forms of the scarps, the processes that might influence form and how variations in these features could affect scarp profile geometry. We mapped structures at the scale of the fault zone: length and width of the fault zone, length of the fault segments, orientation and aspect of fault segments, degree of overlap between segments, throw along the faults and presence of fractures, fissures and monoclines. At the scale of an individual fault scarp, we characterized the rock mass of the volcanic units, mapping lobe and flow boundaries, tumuli, lava tubes, areas of increased vesicularity, cooling joints and any other type of fracture. We also systematically documented instances of geomorphic modification along the scarps, such as topple, rockfall or slides, making note of the spatial extent of these features and the size, shape and approximate orientation of the displaced material. We mapped areas of soil and vegetation cover, identifying the vegetation if present.

To obtain high-resolution topographic profiles for sections of scarps at each site, we used Unmanned Aerial Vehicles or a helium-filled balloon to capture aerial imagery of over 20 kilometers of scarp sections from eleven scarps, using between five to ten ground control points for each survey to georeference the images. We processed the imagery using structure-from-

motion (SfM) photogrammetry, where features are extracted from overlapping images and are used to solve for 3-D positions, resulting in high density, georeferenced point clouds (e.g., Westoby et al., 2012). SfM also allows for the creation of high-resolution orthorectified images, upon which measurements can be taken. We used these ortho-images to extract data such as bedrock fracture density, type and amount of vegetation cover and size distribution and characteristics of geomorphically modified areas.

2.2.3 Topographic analyses

Using our SfM-derived DEMs, along with lidar (0.5 to 1 m^2 resolution) and SRTM topographic data (2 to 10 m^2), we derived a variety of attributes describing the morphometric features of our scarps. We applied an algorithm described in Brigham and Crider (2022) to automatically detect the crests and toes of scarp-normal profiles and calculate scarp height at regular intervals (dependent on DEM resolution) along each scarp. We also computed the profile curvature, plan curvature, slope and aspect of the studied regions using the System for Automated Geoscientific Analyses program (Conrad et al., 2015).

2.3 FIELD SITES

We selected five locations to examine fault scarps in jointed volcanic rock: the east flank of Kilauea on the island of Hawai'i (United States), the northern flank of Medicine Lake Volcano in California (United States), the Volcanic Tablelands north of Bishop in California (United States), the Vogar fissure swarm on the Reykjanes Peninsula (Iceland) and the Thingvellir graben (Iceland) (Figure 2.1). The variety in scarp age, tectonic activity, volcanic effusion rate, scarp height, initial structure, rock mass characteristics and climate allow us to describe the range of processes that influence the initial form and subsequent degradation of these scarps. Age and tectonic activity

provide first-order groupings (A – E Table 1), but the settings also vary in volcanic activity and in climate.

2.3.1 Groups A and C: Kilauea, Hawai'i

The scarps of Group A and C are located on Kīlauea Volcano, an active basaltic shield volcano on Hawai'i Island, Hawai'i. Kilauea is the youngest of the Hawaiian volcanoes, with its oldest strata, collected on the volcano's southern submarine flanks, dating to approximately 275 ka (P. Lipman et al., 2002). Volcanic activity is concentrated in the summit caldera and the two rift zones that extend from it (the East Rift Zone and the Southwest Rift Zone). Subaerially, Kilauea's eruptive sequence can be divided into two major basaltic units: the Hilina Basalt and the Puna Basalt. The Hilina Basalt is best exposed in the Hilina Pali fault system escarpments, as a 300 m-thick sequence of ʻaʻā and pāhoehoe basaltic flows, interspersed with scattered tephra-fall deposits (Easton, 1987). Radiocarbon dating of organic material found between flows (Riley et al., 1999) and known geomagnetic excursions in the Hilina Basalt section (Teanby et al., 2002) suggest a maximum age of 70-50 kya (Sherrod et al., 2021), while carbon dating of material in the overlying Pahala Ash suggest a minimum age of approximately 25 ka (Kelley et al., 1979). Within the Hilina Basalt, individual pāhoehoe flows range in thickness from 0.5 to 16 m, and ʻaʻā flows range from 1 to 6 m thick. The Puna Basalt is a sequence of pāhoehoe and ʻaʻā flows, with the oldest flow dating to 16 ka (Kelley et al., 1979) and the youngest to 2018, during Kilauea's eruptions at the summit crater and East Rift Zone. Most of the Puna Basalt flows at the surface of Kilauea are less than 1500 years old (Neal & Lockwood, 2003).

The scarps of group A are in the Koa'e Fault Zone, a zone of active normal faults that link the two rift zones, approximately 15 km long and 2 km wide, with the Kalanaokuaiki Pali (East and West) marking its southernmost extent. Current fault scarps reach maximum heights of

approximately 15 m and are hosted in the young Puna Basalt flows. However, the Koae fault zone appears to play a key role in accommodating motion of the south flank of Kilauea (e.g., Swanson et al., 2018, Ge et al., 2019), suggesting that the age of these faults is much older than what their scarp heights imply given their frequent resurfacing by lava flows (Duffield, 1975; Podolsky & Roberts, 2008). The Hilina Fault Zone includes the Hilina Pali (group C scarp). The Hilina and Koa'e Fault Zones separate the summit caldera from the mobile southern flank of the volcano, which is moving seaward at a rate of up to 10 cm/year (Owen et al., 1995, 2000) by continuous creep along a basal detachment fault (e.g., Owen et al., 2000), magmatic intrusions (e.g., Delaney et al., 1998), large detachment earthquakes (e.g., Chen et al., 2019; S. E. Owen & Bürgmann, 2006) and slow slip events (e.g., Brooks et al., 2006; Montgomery-Brown et al., 2009; Syracuse et al., 2010). Both fault zones are active, with observable slip on many of the faults during historic earthquakes, such as 1.5 m of slip on segments of the Hilina Pali Fault Zone during the 1975 M 7.2 Kalapana earthquake (e.g., Lipman et al., 1985) or approximately 1.2 m of vertical displacement and 3 m of opening along the Kalanaokuaiki Pali during an eruption-triggered seismic swarm in 1965 (Fiske & Koyanagi, 1968; Podolsky & Roberts, 2008). Both groups of scarps are also subject to frequent strong ground motions from nearby earthquakes, with 178 M>4.5 events in the past 200 years (USGS Earthquake Catalog), resulting in ground motions at the group A and C scarps with PGAs exceeding 80% g (Wyss & Koyanagi, 1992).

The climate at the Hilina Pali and the Koae Fault Zone is tropical submontane. Mean annual rainfall is approximately 1500 mm, much of which is accumulated during large rainfall events, such as subtropical cyclones known as Kona storms (Simpson, 1952), which can deliver upwards of 400 mm of rainfall in a 24-h period (Kodama & Barnes, 1997), generating ephemeral floods

through surface runoff. Average monthly temperatures vary little throughout the year, ranging from 14.6°C to 17.7°C (Figure 2.2).

2.3.2 Group B: southwest Iceland

The scarps of Group B are in southwestern Iceland, where the subaerial expression of the Mid-Atlantic rift currently accommodates between 18 and 22 mm/year of spreading unevenly across different rift zones (LaFemina et al., 2005; Einarsson, 2008). Scarps Sodulholagja and Gildruholtsgja are in the Thingvellir graben, situated in the central part of the 030° striking Western Volcanic Zone, with subsidence rates of approximately 4 mm/yr (Islam et al., 2016) across the graben. Forslund and Gudmundsson (1991) estimated slip on normal faults during rifting episodes to be on the order of 1 m, based on field data and historical accounts on earlier rifting episodes in Iceland. The northern section of the Thingvellir region experiences low to moderate modern seismicity: only 11 earthquakes M>2.5 recorded in the past 100 years in the general area where shaking might affect these scarps (USGS Earthquake Catalog). Approximately 44 km^3 of basaltic lavas were erupted in post-glacial times, with 64% in the first 3000 years after deglaciation (Sinton et al., 2005). Volcanic production declined after this period, with two peaks in eruptive rates from approximately 6-3.5 ka and 1.5-1 ka (Sinton et al., 2005).

Scarps Stora-Aragja and Nydri-Mosadalagja are situated in the northeast of the Reykjanes Peninsula, an obliquely spreading ridge striking 076°, 30° to the spreading direction, characterized by recent volcanism and high seismicity, separating the Reykjanes Ridge to the west from the Western Volcanic Zone and South Iceland Seismic Zone to the east (P. Einarsson, 1991). GPS station velocities indicate left-lateral shear of 17-19 mm/yr, with a significant opening component of 7-9 mm/yr (Árnadóttir et al., 2008). The scarps are part of the Vogar fissure swarm, one of five groups of normal faults, tension fractures and eruptive fissures that accommodate spreading across

the plate boundary in this area (Einarsson, 2018). Stora-Aragja and Nydri-Mosadalagja are likely to experience moderate ground-shaking from regional seismicity. In the past 60 years, the immediate area surrounding the faults (5-mile radius) experienced more than 50 earthquakes M>4, often with PGAs exceeding 10%g at the scarp sites (USGS Earthquake Catalog). On the Reykjanes Peninsula, periods of rifting and volcanism occur at intervals of 800 – 1000 years (P. Einarsson, 1991; Sæmundsson et al., 2020), but both Stora-Aragja and Nydri-Mosadalagja cut through a single volcanic shield dated to 13 ka (Saemundsson et al., 2016).

The climate of southwestern Iceland is maritime, with cool summers and mild winters. Mean monthly temperatures range from 0.3°C to 10.2°C. Mean annual precipitation is approximately 1300 mm/year. Snow alone is only about 5 to 10 % of the total precipitation in southern Iceland. Wind velocities are generally high, particularly along coastal areas like Vogar and during the winter. The Iceland Low, a low-pressure center off the coast of southwest Iceland, brings in frequent cyclones, particularly during winter, that can cause rapid changes in temperature and precipitation (Einarsson, 1984).

2.3.3 Group D: Volcanic Tablelands, Bishop, California

The scarps of group D are part of a group of normal faults in the Volcanic Tablelands in northern Owens Valley, California. Range-front normal fault systems bound both sides of the Owens Valley graben, with the Sierra Nevada fault system to the west and the White Mountain fault to the east. The extensional faulting that formed the valley is thought to have begun between 2 and 6 Ma and resulted in each fault system accumulating 3 to 4 km of normal throw (Bateman et al., 1965; Bachman, 1978; Pinter & Keller, 1995; Lueddecke et al., 1998; Phillips & Majkowski, 2011). The Bishop Tuff was emplaced in Owens Valley at 760 ka during a six-day, 600-650 km^3 eruption (Hildreth & Wilson, 2007) which formed the Long Valley Caldera. The emplacement of

the approximately 70- to 140-m thick Bishop Tuff at 0.76 Ma likely buried pre-existing extensional structures that were reactivated and influenced current day fault patterns (Bateman et al., 1965; Ferrill et al., 2016). The tuff is not uniformly welded. Localization of fracturing appears to be a function of welding, with faults and fractures concentrated in units with greater degrees of welding (Evans & Bradbury, 2004). The scarps in group D are situated in the caprock of the Tableland, a densely welded and jointed ash-flow tuff. The normal faults of the Volcanic Tablelands range widely in both length (approx. 24 m. to 2.2 km) and throw (<1 m to 145 m), with the largest fault being the Fish Slough Fault (Dawers et al., 1993). The Volcanic Tablelands are situated in an arid climate, receiving approximately 120 mm/year of precipitation. Mean monthly temperatures range from 3.2°C to 24.8°C, and mean diurnal temperature variation is 17.1°C.

2.3.4 Group E: Medicine Lake Volcano, California

The scarps of group E are located within a zone of dominantly north-south-trending, regional-scale normal faults on the north-flank of Medicine Lake volcano, which is undergoing east-west extension, due to its position within the tectonically active terrane behind the volcanic front of the Cascades arc and at the west edge of the Basin and Range province (Donnelly-Nolan, 2010). A large portion of the scarps of group E occur in basaltic flows that pre-date Medicine Lake Volcano activity, dating to approximately 910 ka (Donnelly-Nolan, 2010). Volcanic activity at Medicine Lake volcano began at 500 ka, unfolding in multiple eruptive stages (Donnelly-Nolan, 2010). There are indications of Holocene faulting at Medicine Lake Volcano as young as 12.5 ka (Donnelly-Nolan et al., 2007). Few earthquakes have occurred near the group E scarps during historic times (22 in the past 100 years, none greater than M 4.3, USGS Earthquake Catalog) and they were centered 10 to 20 km away from the scarps. The northern flank of Medicine Lake Volcano is situated in an arid climate, receiving approximately 482 mm/year of precipitation on

average, 65 mm/year of which falls as snow. Mean monthly temperatures range from -0.3°C to 19.3°C, and mean diurnal temperature variation is 14.3°C, with freezing temperatures that can occur any night of the year (Donnelly-Nolan, 2010).

2.4 FIELD OBSERVATIONS OF ATTRIBUTES AND PROCESSES THAT INFLUENCE SCARP FORM

The morphology of fault scarps in jointed rock differs from scarps in other lithologies along three main axes: rock mass characteristics, fault zone structure and modification processes. We synthesize the cross-disciplinary work existing in each of these three areas, along with our field observations. We use scarp-perpendicular topographic profiles to illustrate the influence of these attributes or processes on the morphology of the scarps.

2.4.1 Rock mass characteristics

2.4.1.1 Background

The distribution of cooling joints in a basalt flow is a result of thermal processes and form perpendicular to the cooling front (Spry, 1962), which provides a first order framework in which to consider these discontinuities (Figure 2.3a). Since higher cooling rates result in smaller joint spacings (Degraff & Aydin, 1993) and flows cool from the top down at a higher rate than from the bottom up (Long & Wood, 1986; Degraff & Aydin, 1987; Lyle, 2000), the rock mass is characterized by two tiers of column-bounding fracture that meet below the flow centers, with increasing spacing the further they are from the flow edge. The resulting architecture is one governed by cooling joint density, with more densely jointed flow tops and bases and a massive core. Beyond this simple cooling-rate framework, the types of discontinuities that are present in the rock mass are influenced by the lava emplacement process and the volume of the flow. Rubble-

cored ‘a‘ā flows are formed by channelized high-discharge lavas (S. K. Rowland & Walker, 1988), but most basaltic fields are emplaced via inflation of pāhoehoe lobes, where the upper surface of a flow is lifted by the injection of additional liquid lava into the molten core of the flow, allowing the flow to advance (Hon et al., 1994). In cross-section, this style of emplacement is characterized by vertical and lateral heterogeneities set by the dimensions of the elliptical lobes. The lava effusion rate is an important parameter in determining these dimensions (Figure 2.3b), with lower effusion rates creating a larger number of smaller lobes and a high degree of vertical and lateral variability and higher effusion rates creating large sheet-like lobes with less cross-sectional variability (Self et al., 1998). Long-lived flows continue to propagate downslope thanks to systems of well-developed lava tubes in the seemingly stagnant upslope lobes (Hon et al., 1994), adding another source of heterogeneity to the flow architecture. The topography encountered by the flow can also introduce irregularities in the rock mass, with steeper irregular surfaces favoring the production of hummocky flows with many discrete tumuli and inflation pits (Self et al., 1998). Given the complexity of the inflated flow architecture, determining the number of flows in a sequence can be difficult, but pauses in eruptive activity can be marked by interflow units of varying origins: alteration products of flow bases (e.g., Duraiswami et al., 2008), paleosols developed on flow tops (e.g., Sheldon, 2003; Hobbs & Parrish, 2016), altered volcanic ash (e.g. Wilkins et al., 1994), inter-flow sediments (e.g., Duraiswami et al., 2003;Srivastava et al., 2012) or weathering products of flow-top and flow-bottom breccias (e.g., Duraiswami et al., 2020).

2.4.1.2 Observations

At our field sites, the rock mass is most commonly intact basalt separated into irregular blocks by networks of irregular, discontinuous fractures. Joint spacing, orientation and aperture are not constant at a single outcrop. Given this variability, it is difficult to construct a blueprint for

the structure of a 'typical' volcanic flow from our observations; here, we describe common rock-mass features among sites and identify the most variable rock mass attributes. We consider the attributes of the bedrock at three scales: the jointing patterns within a single lobe or unit (Figure 2.3a, 2.3d, 2.4a), the partings created by the interaction of multiple lobes (Figure 2.3b, 2.4b) and the layering characteristics created by multiple flows (Figure 2.4c).

The rock mass at all field sites is characterized by pervasive vertical to sub-vertical jointing that varies in spacing and form, attributable to the cooling of the volcanic flows. Vertical joint spacing ranges significantly, from decimeters to multiple meters, and can vary both laterally along the scarp and vertically along the free face of the scarp. Joint aperture also ranges two orders of magnitude, from extremely wide (approx. 30 cm) to tight (<1 mm). Vertical joints tend to be sub-planar but can be curved and exhibit more complex geometry. Horizontal partings are also widely present at all field sites and are linked to either vesicle banding, cooling fronts causing changes in vertical joint spacing or layering between different lobes or flows. The spacing of horizontal partings are roughly the same as vertical jointing, ranging from 10s of cm to approximately 10 m. At the basaltic sites, we can often distinguish the horizontal boundaries created by the three characteristic components of a typical basalt lobe: a densely vesicular and jointed flow top, a massive core and a base with pipe vesicles and/or platy jointing (Figure 2.3a). Within a single lobe, horizontal boundaries tend to be gradational, occurring as changes in vertical joint spacing (e.g., joint spacing decreases at the edges of a flow). However, distinct horizontal fractures are also present, such as when planes containing abundant vesicles (Figure 2.3a) form zones of weakness through which horizontal fractures propagate. In the welded ignimbrite of the Volcanic Tablelands, horizontal partings form between sub-parallel vertical joints but tend to be discontinuous

throughout the rock mass as a whole (Figure 2.3d), suggesting that many of these sub-horizontal fractures are younger than the vertical cooling joints.

For the basaltic sites, we observe in the free faces of the scarps that the flows are made up of multiple lobes that vary in size and shape among sites and to a lesser extent, between scarps. This suggests that the primary mode of emplacement at all sites is inflation of pāhoehoe lobes, although we do find ‘a‘ā flows interlayered in the Koae Fault Zone, which create laterally-continuous rubble-rich zones. In Hawaii, lobes range in width from less than a meter to approximately ten meters and in height from tens of centimeters to several meters. In the Medicine Lake Volcano flows, lobes range in width from several meters to tens of meters and in height from a meter to ten meters. In the Icelandic flows, lobes range in width from several meters to hundreds of meters and can reach heights of greater than 10 meters. These differences in average dimensions likely reflect changes in eruptive styles between the sites, e.g., the large volume Icelandic flows creating larger sheet lobes due to higher effusion rates than the smaller volume Kilauea flows. Filled and unfilled lava tubes are another source of mechanical heterogeneity at the decimeter- to meter-scale and are present at all basaltic sites. In the welded ignimbrite of the Volcanic Tablelands, no lobe-like structures are observed and overall jointing patterns set the scale of the discontinuities. At the surface of the flows, we observe tumuli at all basaltic sites, with Hawai’i having the most numerous with the highest degree of preservation.

Identifying the contact between flows, the number of eruptive events and the thickness of the flows remains difficult at our basaltic sites, given the heterogeneities present within a single flow and the complexities of the overall flow architecture. For most of the Icelandic scarps, the scarp is shorter than the flow thickness, so we do not see the flow boundaries. In Hawai’i, it is difficult to distinguish lobe boundaries and flow boundaries in the scarp faces. Vegetation and

talus make finding flow boundaries difficult in most of the Medicine Lake Volcano scarp faces, though thick exposures of ash can be observed in landside-modified portions of the Gold Digger Pass scarp. Identifying flow boundaries in the debris-flow incised valleys of the Hilina Pali (Figure 2.4c) is relatively simple. We observe highly oxidized reddish surfaces corresponding to paleosols, as well as thin beds of yellowish to brown ash.

The heterogeneities observed in the rock mass have implications for scarp form at multiple scales. Joint spacing is a primary control on the size of blocks that can be detached from the free face of the scarp. The ratio of average joint spacing to scarp height determines the degree to which block size affects scarp form: as the ratio decreases, the detachment of individual joint-bounded blocks is less likely to have a noticeable effect on scarp profile form (Figure 2.4a). The presence of partings between different lobes also has effects on scarp form that are dependent on both the size of lobes and the height of the scarp. If the height of the lobe approaches that of the scarp (e.g., Stora-Aragja, Nydri-Mosadalagja), fewer horizontal boundaries are present and the initial profile form will tend to be a uniform, steep free face (Figure 2.4b-panel 1). If the height of the scarp allows for multiple lobes to be exposed (e.g., Gold Digger Pass Scarp), both initial fault propagation and preferential erosion along the lobe partings will tend to create a stepped scarp-normal profile (Figure 2.4b-panel 2). If lobe size is low compared to that of scarp height (e.g., Kau Desert Fault Scarp), minor irregularities will be present in the scarp profile (Figure 2.4b-panel 3). Laterally, lobes and surficial features like tumuli are responsible for lenticular increases then decreases in scarp height (e.g., Stora-Aragja), which can mask true changes in fault offset when the size of these features is large relative to scarp height. At the scale of multiple flows, inter-flow units can serve as planes of mechanical weakness, allowing for landslides (e.g., Golddigger Pass

Scarp, Crumes Lake Scarp) and debris flows (Hilina Pali) to alter scarp form dramatically (Figure 2.4c).

2.4.2 Fault zone structure

2.4.2.1 Background

Correctly interpreting morphological information from a fault scarp requires knowledge of its initial form. The normal fault scarps we examine here owe their initial form to structural processes, influenced by extension rate and lithology. Because the initial morphology of a fault scarp is influenced by the style of faulting, many workers have used scarp metrics such as length and throw to illuminate faulting characteristics at depth (e.g., Gudmundsson, 1992; Willemse, 1997; Acocella et al., 2000; Sonnette et al., 2010; Villemin & Bergerat, 2013). Though displacement variation along faults is common, idealized throw profiles are elliptical, commonly with the steepest displacement gradients near the fault tips (Dawers et al., 1993; Dawers & Anders, 1995). In a young extensional setting, populations of normal fault scarps are discontinuous in map view. As the fault system matures, these segments grow, overlap and form relay ramps between segments (Trudgill & Cartwright, 1994; Peacock & Sanderson, 1994; Crider & Pollard, 1998). As these faults overstep, the dip of the relay ramp increases until the ramp is breached by a connecting fault, producing a single, irregular fault (Peacock & Parfitt, 2002). As deformation proceeds, the throw profile of the linked segments will approach that of a single fault (e.g., Dawers et al., 1993). Though this general conceptual model aids scarp interpretation, complexities specific to fault initiation and growth in jointed bedrock have driven numerous studies on near-surface deformation patterns in basaltic regions, allowing us to construct a more detailed framework (Figure 2.5). Most workers have concluded that normal faults in jointed rock nucleate at depth and propagate upwards (e.g., Grant & Kattenhorn, 2004; Martel & Langley, 2006; Kaven & Martel, 2007; Bubeck et al.,

2018). Propagation of the fault causes monoclinal flexure at the surface, with more steeply dipping faults producing narrower monoclines (Grant & Kattenhorn, 2004; Martel & Langley, 2006; White & Crider, 2006). Stress distributions in this early stage of faulting cause fissuring on the footwall and cavities on the hanging wall side (Martel & Langley, 2006). If spreading is oblique, en echelon fractures form oblique to the spreading direction. If spreading is perpendicular to the fracture zones, fractures are typically parallel to the fracture zones except at bends in the fault traces (Grant & Kattenhorn, 2004). As the fault tip nears the fissure, buckles form near the base of the scarp and small subsurface antithetic faults cause fractures to open on the hanging wall (Martel & Langley, 2006; Kaven & Martel, 2007). Discontinuous monoclines can form during the propagation of these antithetic faults from a fault-bound rotation of the immediate hanging wall (Bubeck et al., 2018). As the main fault breaches the surface, the monocline collapses or becomes progressively steeper, and the fissure links with the fault (Martel & Langley, 2006). Stress concentrations shift to the end of the fault trace, allowing previously formed and preferentially oriented en echelon fractures to slip laterally and link as the fault propagates (Kaven & Martel, 2007).

Recent studies have added detail relevant to the interpretation of scarp form to this framework of near-surface deformation in basalt. Sonnette et al. (2010) considered how the resurfacing of older scarps might affect the fault zone geometry of fault scarps in lavas of three different age groups. They found that the overall fault zone length was similar for all age groups but that the mean and maximum throw of the zone increases significantly with lava flow age. They suggested that this was due to fault growth being governed first by an increase in length at the fault tips, followed by an increase in vertical throw. Their results also show that the maximum fracture length in the youngest lava is shorter than those from the two other age groups.

Several types of fault-parallel folds, with different surface characteristics and attributed mechanisms, could affect scarp profile form. Bubeck et al. (2018) distinguishes between scarps with monoclines that are continuous at the kilometer scale, scarps with monoclines that are discontinuous and have maximum lengths of approximately 150 m and scarps with no monoclines. They attribute these differences in scarp style to variations in strain rate, both spatially and temporally: low strain rates will result in continuous monoclines, whereas high strain rates lead to scarps with no monoclines or just discontinuous monoclines caused by the rotation of hanging wall blocks. Kettermann et al. (2019) refer to the monoclines as large tilted blocks and propose that variations in scarp form due to tilting are a result of differences in mechanical heterogeneity.

2.4.2.2 Observations

Fault zone lengths in our field sites range over an order of magnitude, from 1.8 km to 18.6 km, and maximum scarp height along the faults ranges from 8 m to 475 m (Table 2). The faults from our field sites roughly follow the displacement-length scaling relationships for faults presented in Cowie & Scholz (1992), with the exception of the Medicine Lake Volcano faults, which have lower maximum displacement values relative to fault length than the fault populations presented in the study (Figure 2.5b). Looking across age groups, fault zone length does not vary systematically with any of the three metrics we use to characterize scarp age. For example, the Koae faults are the youngest scarps, in terms of both time since initiation and time since the last growth episode, but they have lengths that are more than double that of the longer-lived Volcanic Tablelands scarps. Maximum scarp height seems to increase generally with scarp initiation age, but the significant exception of the Hilina Pali casts doubt on the reliability of this relationship. Given the differences in volcano-tectonic histories between the sites, we expect certain sites to be influenced by the geometry and mechanics of faults underlying the current scarp, buried by

younger lava flows (e.g. Ohale Scarp, Sodulholagja). Other sites (e.g., Bishop Scarp 2, Hilina Pali) have undergone little or no volcanic resurfacing and thus are less likely to be affected by older scarp forms. To explore this difference quantitatively, we compare displacement to length (D/L) ratios between the two groups and find that fault scarps with a history of volcanic resurfacing have D/L values that are an order of magnitude smaller than those of that have no resurfacing. We also consider the ratio of the length of the longest individual fault segment to the total length of the fault zone, finding that the group that has not experienced as much resurfacing had proportionally longer scarp segments (Figure 2.5a). Though Sodulholagja and Ohale have longer fault zone lengths (6.5 and 4.9 km, respectively) than Bishop Scarp 2 (2.6 km), the length of their longest individual fault segment accounts for a much smaller proportion (6.1 and 6.5%, respectively) than that of Bishop Scarp 2 (39.6%). This suggests that the overall fault zone length for resurfaced scarps accounts for structural inheritance of the buried fault segments, whereas the individual segment lengths represent the stage development of the present scarp.

Beyond the length and height of the scarp, surface structures can also control scarp profile form. We observe three main types of structures identifiable in profile form: monoclines, relay zones and secondary fractures and fissures (Figure 2.6). In profile, monoclines are characterized by convex upward slopes, with an abrupt change in curvature where the flexure ends. Using the terminology of Bubeck et al. (2018), we distinguish between monoclines that are laterally continuous on the hundreds-to-thousands-meter scale and those that are discontinuous. We also consider whether monoclines are breached by a free face, broken by a fissure or unbroken. We identify the majority of monoclines in scarps where there has not been enough geomorphic modification to obscure the faulting-related structures, namely in groups A, B and D. Discontinuous, unbroken monoclines occur at fault zone tips (e.g. Bishop Scarp 2) or linking non-

overlapping fault segments within the fault zone (e.g. Sodulholagja) and produce slopes that range from approximately 15 to 20 degrees. We did not observe laterally continuous (> 150 m), unbroken monoclines in the scarps that we selected for study, but some were present in the greater Koae Fault Zone, ranging from approximately 400 m to 900 m in length, 3 to 6 m in total scarp relief and 10 to 20 degrees in slope. Laterally continuous broken and breached monoclines were common in the scarps of group A, particularly along the Ohale Fault scarp, ranging in length from 200 m to 2.7 km, in average slope from 20 to 40 degrees and reaching scarp reliefs of approximately 5 m. Many of these continuous monoclines have buckle zones at their toe (synclinal hinge), where the monoclinal limb steepens and the jointed rock is brecciated. The scarps of group D also showed continuous breached monoclines, with lengths ranging from 180 to 350 m. Discontinuous, breached or broken monoclines exist along scarps in groups A, B and D. The Kalanaokuaiki Pali (group A) has discontinuous, broken and breached monoclines that range in length from 70 to 120 m and in average limb slope from 10 to 35 degrees. Discontinuous, breached monoclines in Gildruholtsgja (group B) range in length from 75 to 90 m and in average limb slope from 25 to 45 degrees.

In groups A, B and D, fault segments are linked by relay ramps that create broad slopes as the fault steps over. In profile form, the relay ramps are characterized by linear to convex upward slopes of variable widths separating two scarp steps (e.g., group E scarp Bishop Scarp 3). As fault growth continues, the segments become hard-linked and breach the ramp, introducing heterogeneities in the profile form (e.g., group B scarp Nydri-Mosadalagja). Relict relay ramp fragments may persist in scarp form after the breach, even after being partially buried by colluvium, creating a second step at a lower height (Figure 2.6). This lower step could be confused as a scarp from a younger rupture, which might lead to errors in paleoseismic interpretation: for

example, if one were to use cosmogenic dating techniques on material from the lower scarp free face, the age would be older than that of the free face higher in the same scarp-normal profile, since that section of the relay ramp was older than the event that breached the relay or any other growth event after that. Fault zone structure can give some indication of these features being ramp fragments, since the trace of these small scarps tends to bend toward the main scarp trace.

2.4.3 Modification processes

Structural deformation, paired with rock mass characteristics, determine the original form and growth rate of a fault scar and can continue to influence scarp morphology throughout its history. Geomorphic and volcanic activity modify the original form of the scarps during faulting itself, between periods of tectonic activity and after tectonic activity has ceased. The wide range in types and rates of modification processes and their interplay with structural processes can produce a wide variety of scarp forms.

2.4.3.1 Volcanic activity

Volcanic flows interact with fault scarps in active volcanic terrains and modify scarp morphology at a variety of scales, depending on the size of the scarp, the position and volume of the flow and the relative rates of scarp growth and volcanic activity. We consider three types of scarp-flow interactions: draping, abutting and resurfacing. Draping results from a flow coming from the footwall and flowing over the scarp. The effect of draping on the scarp-normal profile form depends on the overall height of the scarp relative to the thickness of the flow. For example, in the case of the Hilina Pali, the morphologic effect of draping younger flows is small relative to scarp height, though thick ‘a‘ā flows create large lobes at the base of the scarp. In the Koae fault zone, relatively thin lobes (approximately 0.5 to 1 m thick) alter the profile morphology significantly. The crest and the toe of a draped scarp decrease in absolute curvature, and the mid-

slope angle of the scarp decreases. These flows are draped over toppled blocks or rockfall deposits, resulting in void spaces below the flow. When slip reoccurs on the fault, these thin, mantling flows are brecciated. Draped flows can confuse interpretation of scarp structures, since their profile form and the orientation of the surficial cooling joints can resemble those of a monoclinal fold (e.g., southern section of the Gold Digger Pass Scarp). Some surficial features give hints whether the flow cooled horizontally or at an angle, such as the orientation of pāhoehoe ropes relative to the scarp slope.

If the flow comes from the hanging wall side of the scarp and the total height of the flow is less than that of the scarp, the flow will pond against the scarp. Abutting flows can alter the profile form of scarps by decreasing scarp height, obscuring fault structures such as monoclines or geomorphic processes such as rockfall and/or creating small-scale morphologic discontinuities due to the contraction of the abutting flow during cooling (e.g., Kau Desert Fault, Appendix 2).
Volcanic flows resurface fault scarps when the volume of the flow is sufficient to completely mask the topographic signature of the scarp. Scarps can be partially (e.g., Sodulholagja) or fully (e.g., Gildruholtsgja) resurfaced along their length. Volcanic resurfacing erases scarp relief and thus structural information on the throw and length of the scarp. However, as noted in the fault zone structure section, the structural characteristics of an active resurfaced system may continue to differ from a fault zone that had not experienced volcanic resurfacing. The rate of volcanic resurfacing relative to that of scarp growth is an important metric in determining the possible longevity of a scarp and thus the maximum height it can obtain and the time-scale at which other modification processes can occur.

2.4.3.2 Hillslope processes

2.4.3.2.1 Background

Once the fault and volcanic flow structure have set the initial scarp form, the type, scale and tempo of the hillslope processes that move material downslope are crucial in determining the morphologic evolution of the fault scarp. These processes include rockfall, talus reworking, debris flows and landslides.

A rockfall is an event in which joint-bounded rock fragments are detached from a free face and fall, roll and bounce along the slope, either maintaining its original shape or breaking into smaller fragments (Hungr et al., 2014). Toppling is a specific type of rockfall in which a rock column pivots at a basal discontinuity and collapses once the center of gravity of the block rotates beyond the edge of the base (e.g., de Freitas & Watters, 1973; Crider, 2008). Triggering mechanisms for rockfall include seismicity-related ground shaking (e.g., Mackey & Quigley, 2014; Massey et al., 2022), climatic conditions (e.g., Abellán et al., 2010; D'Amato et al., 2016) and freeze-thaw episodes (e.g., Matsuoka & Sakai, 1999; D'Amato et al., 2016). Evidence for this process includes widespread fresh rockfall, disaggregation of column networks at the surface, toppling and breaking of large columns and collapse of monoclines into rubble piles (Rowland et al., 2007; Blakeslee & Kattenhorn, 2013). Peak ground acceleration is strongly correlated with rockfall volume, followed by relative height above the base of the slope (Massey et al., 2022). Ground shaking could be produced by seismic slip on the fault itself or another regional seismic source. Volcanic activity (e.g., tremors and eruptive activities) can also cause ground shaking that results in rockfall (Hibert et al., 2014). Climatic conditions that could affect the scarps include rainfall (e.g., Larose et al., 2015; Turowski et al., 2016; Melillo et al., 2020), wind (e.g., examples in Dietze et al., 2017; Lott et al., 2017), lightning strikes (e.g. Kappus & Vernon, 1991), freeze-thaw conditions (e.g., Matsuoka & Sakai, 1999; Mateos et al., 2012) and thermal stresses (e.g., Collins & Stock, 2016; Eppes et al., 2016). The probability of rockfall in an area increases with

previous rockfall events in adjacent areas, leading to clusters of rockfalls near areas that have failed previously (Massey et al., 2022). This suggests that the seismically-induced rockfall from the active tectonics and volcanism of our study areas might precondition areas along the scarp to be more susceptible to climatic factors later on and vice versa.

Each rockfall event delivers rock fragments to the base of the scarp, leading to the accumulation of a talus deposit. The shape and slope of the talus is governed by the characteristics of the processes that deliver material to the slope from the rock face and those that redistribute slope debris. Taluses often share similar characteristics, such as the marked longitudinal sorting where the finest grains appear at the top of the talus and the coarse particles in the lower part (e.g., De Blasio & Sæter, 2009). The redistribution of material downslope can happen gradually through progressive creep, caused by fluctuating temperatures (expansion-contraction creep), needle ice action (freeze-thaw creep) or precipitation (runoff creep) (Pérez, 1985). Creep and sliding more effectively redistribute the particles according to the principle of kinetic sieving (Sass & Krautblatter, 2007; De Blasio & Sæter, 2009), leading to inverse grading and the formation of layers of smaller particles in the debris body. This smoother, and thus weaker, layer can serve as a sliding plane for failures of large portions of the talus slope (van Steijn et al., 1995; De Blasio & Sæter, 2009). Larger amounts of material are transferred downslope through shallow slides along these planar surfaces, through dry debris flows caused by shear distortion of the granular materials or through debris avalanches of partially or fully saturated talus material (Hungr et al., 2014). Lateral variations in clast size along the talus deposit can reflect both changes in redistribution process (e.g., between creep, sliding and flow) and lateral variations in joint spacing in its source bedrock unit (Wilson, 1990).

Debris flows can also affect scarp hillslopes when scarp relief is sufficiently high, drainages are present to concentrate the flow and climatic conditions are favorable to induce high discharge rates. Debris flows often occur with floods and are initiated by destabilizing events (e.g., slides or rockfall) along a steep drainage channel or gully that lead to rapid loading of the channel bed and liquefaction of the debris (Hungr et al., 2014). The debris flow then surges down the drainage, eroding and entraining material along the channel banks, until it deposits its material in a debris fan, which is characterized the presence of large individual particles, levees and boulder fronts (Hungr et al., 2014). In most cases, gully incision and accumulation of debris fans lead to an increase in slope concavity (Curry & Morris, 2004).

Landslides can also fundamentally change fault scarp morphologies and erase (or obscure) earlier geomorphic and structural features. In basalt, competent flows interbedded with weaker materials (e.g., ash or clay-rich layers) are susceptible to landslides (e.g., Safran et al., 2011).

2.4.3.2.2 Observations

Given the jointed nature of the bedrock and the gravitational potential of the scarp height, rockfall is a process that was widely present at each field area. We identified cobbles and boulders as having been deposited on scarp slopes through rock fall specifically when they had a characteristic angular shape that could be spatially matched to a void in the free face (Figure 2.7. a.), but we assume that most of the scree deposits at the base of scarps were accumulated through rockfall. The profile form associated with rockfall consists of one free face or multiple free faces separated by short steep bare bedrock slopes (Figure 2.7.b.), varying between profiles within a wide range (between 80 and 10%) of the total scarp height, a mid-slope ranging between 15º and 30º and a short lower slope connecting the mid-slope to the toe of the scarp (Figure 2.7). Profiles where rockfall activity is high are characterized by the short scale heterogeneities of the fallen

blocks. Blocks in the lower scarp slopes can have smaller dimensions than those predicted by free face joint spacing, suggesting that the impact with the ground is capable of disintegrating material, but the slope profiles continue to display roughness elements even when the free face reaches heights of 10 m or more (Figure 2.7.c.). Vegetation is sparse in areas where rockfall activity appears to be high but can grow more abundantly in areas immediately adjacent (Figure 2.7.d.), suggesting that frequent rockfalls limit shrub expansion on slopes.

The Gold Digger Pass Scarp and the Hilina Pali are examples of scarp systems with well-developed talus slopes accumulated through rockfall at two different scales. We can describe a large portion of the variability in scarp talus slope profiles along five parameters: the height of the bedrock wall delivering the talus material, its complexity (single or multiple free faces), the mean slope of the talus, the curvature of the profile and the number of breaks in slope in the profile. Figure 2.8 presents examples of scarp-normal profiles taken of talus slopes along the Gold Digger Pass Scarp and the Hilina Pali. We see that both scarps present along-strike variability in profile form. The profiles of the Gold Digger Pass scarps all display clearly-defined free faces but vary in complexity and curvature. We can distinguish three main morphologic groups: 1) concave-upward profiles with simple free faces, mid-slopes reaching values of 30° or higher and distal slopes between 20-25°; 2) concave-upward profiles with complex free faces (multiple steps that lower the overall slope of the free face), mid-slopes of 25° or less and distal slopes between 20 and 15°; and 3) slightly convex-upward profiles with simple, short free faces and mid-slopes of approximately 30°. Average block size in the talus deposits varies laterally along the scarp (Figure 2.8.d.), with larger blocks on average corresponding to groups 2 and 3. Group 3 also occurs primarily in areas where the trace of the free face bends, suggesting that the convexity of the slope might be due to a more complex bedrock structure created over the course of two fault segments

becoming linked. The profiles of the Hilina Pali vary laterally as well. In our morphologic analysis, we discounted profiles taken from alluvial channels (discussed below) and focused on slopes where scree was present and did not appear to be linked with processes related to the bedrock channels. Vegetation tends to be sparse on the talus slopes in the central portions of the scarps, whereas bands of grass- and tree-rich areas alternate with bare talus on the outer edges of the scarps, suggesting a higher rate of rockfall and talus redistribution processes in the center of the scarp. The banded nature of the rock fragments close to the edges of the scarp suggest that the talus is also accumulating through rock and debris slides, rather than just through rock fall of small groups of blocks. We note two general morphologic classes: 1) profiles with a complex free face exposing many basaltic flows, a proximal slope varying between approximately 30 and 35° and a distal slope of 10° or less; and 2) profiles with no discernible free face and a relatively straight slope of approximately 35°. Looking at the attitude of the flows exposed in channels close to the topographic profiles, we see that the beds are either dipping approximately at the same angle of the slope or are sub-horizontal. When the beds are dipping, nearby profiles are more likely to be of the second morphologic class, suggesting that those types of profiles are associated with mantling flows. A certain amount of the rock fragments along these slopes are thus likely to be part of a brecciated flow, rather than products of talus accumulation through rockfall from a free face.

Portions of the Hilina Pali that have accrued more than 100 m of scarp relief show evidence of significant modification by processes other than episodic rockfall. We observe deeply carved alcoves with fans of debris at their bases. These alcoves can reach dimensions of 400 m x1000 m and expose over 150 m of flow stratigraphy. Dry, bedrock channels originating from the northern section of Kilauea intersect these alcoves. The boundaries of the fans vary between being sharp

and diffuse, and their texture varies from hummocky to channelized. Fans with very sharp boundaries (e.g., Figure 2.9, profile 4) have slopes of approximately 25°, whereas fans with very diffuse boundaries (e.g., Figure 2.9, profile 1) have slopes of less than 10°. The first type of fan appears to have been formed through mass wasting processes that did not involve much fluid flow (e.g., rock avalanching), either during the event(s) or afterwards, given the sharpness of the boundaries and the lack of evidence of redistribution through channelized flows. The second type of fan is either the product of continuous erosion through fluidized flows (e.g., debris or flood flows) or redistribution of material through fluidized flows after initial non-fluidized mass-wasting events. The fans with intermediary slopes might represent different stages of this erosive process, as fans build up and then are redistributed via flows during storm events.

We also observe landslides at different scales along the studied fault scarps. In the Koae Fault Zone, we observe areas where structural monoclines and draped flows have had transitional slides, generally failing along a planar interface separating cooling joints of different dimensions (Figure 2.10.A.). Along the Gold Digger Pass scarp, we note a landslide that has failed along the boundary between an ash-tuff and pāhoehoe flows. We also find evidence of more complex types of mass movement. Along the Crumes Lake Scarp, we find a series of landforms with a scalloped headwall, a series of small scarps and counter-scarps that run parallel to the headwall and a lobate toe (Figure 2.10.B.). These features most closely resemble earthflows but are mantled by blocky basalt.

2.4.3.3 Physical and chemical weathering

2.4.3.3.1 Background

Though cooling joints determine the initial geometry and size of material that might be released from the scarp face and slope, mechanical weathering is a key process in any further

breakdown of rock into smaller particles. The initial stages of physical weathering in surface materials such as lava flow surfaces or boulders is marked by cracking (McFadden et al., 2005). The concept of subcritical cracking relies on the action of modest but persistent stresses that are either steadily or frequently applied on the rock to ultimately produce rock breakdown under a wider range of conditions than those predicted from a traditional critical stress-strength analysis (Eppes & Keanini, 2017). Cracking is triggered by a wide variety of parameters, ranging from unloading (e.g., Ko & Kemeny, 2007), freezing and ice segregation (e.g., Draebing & Krautblatter, 2019), biologic processes or even simple diurnal variations in temperature (e.g., Eppes et al., 2016). As the rock breaks down through mechanical weathering, more surface area is available for chemical weathering to take effect, dissolving and precipitating minerals and leading to changes in rock chemistry, porosity, permeability and strength (e.g., Tuğrul, 2004; Fletcher et al., 2006; Navarre-Sitchler et al., 2009).

2.4.3.3.2 Observations

We observe blocks of varying scales that we interpret to be the products of climate-driven subcritical cracking, which we broadly group into three size categories: 50 – 200 cm; 10 – 50 cm; and less than 10 cms. Beyond the size of the fractured blocks themselves, the characteristics of the fractures tend to differ by category. At the scale of 50-200 cm, it can be very difficult to differentiate between cooling joints and larger fractures derived from sub-critical cracking, so we focused on identifying examples that were clearly linked to mechanical weathering. We documented boulders (1 – 3 m long axis length) that were out of place from the primary volcanic flow and that were fully bisected by fractures whose surfaces could be directly matched. The position and characteristics of the fracture in these blocks suggest it propagated after the block was detached from the volcanic unit. We found boulders fractured in this manner in the slopes of scarps

from Bishop, the Thingvellir region of Iceland and the Kau Desert of Hawai'i (Figure 2.11. A.). These fractures tended to be vertical to subvertical, often parallel to the long-axis of the boulder, with surfaces that were either planar or curved.

We made rough assessments of the degree of chemical weathering at each site by observing soil formation on the slopes and along the base of the scarps. Soils were present at each site, but not in quantities sufficient to mantle large portions of the bedrock scarp, with the exception of the Icelandic scarps. The Icelandic scarps are partially covered in moss and grasses anchored in thin soil lenses, and depth to intact bedrock at the base of the scarp reached 50 cm in areas. However, it was difficult to determine whether these soils were derived from the in situ breakdown of bedrock or whether they were transported to the scarp via aeolian processes. Attributing soil formation to in situ mechanical and chemical processes was easier in areas along the young scarps of the Koae Fault Zone. For example, material from translational slides along the limbs of over steepened monoclines created small levees trapping clasts, which seemed to break down into smaller and more intensely weathered material, finally leading to dark brown soils.

2.4.3.4 Vegetation

2.4.3.4.1 Background

Vegetation can serve both as a stabilizing force on rock faces and hillslopes, allowing them to maintain their form, and as an agent of mechanical or chemical weathering that can disrupt profile form at a variety of spatial and temporal scales. The effects of vegetation on scarp profile form vary with vegetation type, age and/or size, spatial distribution on the slope and the different vegetation components, including the above- and below-ground biomass. This complexity is increased by the variability, both along the scarp and through time, introduced by primary bedrock

structure, fault structure, hillslope processes and non-biogenic mechanical and chemical weathering processes.

Tree roots act both biomechanically and biochemically on fractured bedrock. Mechanically, tree roots can exert maximum radial growth pressures ranging from 0.51 to 0.9 MPa (Lambers et al., 2008), can detach rock fragments through subcritical cracking during expansion (Pawlik et al., 2016; Anderson, 2019) and can lead to cliff recession (Jackson & Sheldon, 1949; Pawlik et al., 2016). Once roots have penetrated the bedrock via a fracture, moisture fluxes along the root, root respiration and dissolution of minerals by solutions secreted by symbiotic microbiota contribute to enhanced biochemical weathering, often at a scale unavailable for biomechanical erosion (Berner & Cochran, 1998; Burford et al., 2003; Taylor et al., 2009; Pawlik et al., 2016). Trees on mid-slopes can affect profile form by: 1) stabilizing the slope by increasing soil cohesion and anchoring weaker soil lenses to bedrock through root systems (Gabet & Dunne, 2002; Roering et al., 2003; Kuriakose & van Beek, 2011); 2) extracting and transporting fractured bedrock downslope through tree throw (Gabet et al., 2003; Gabet & Mudd, 2010); and/or 3) damming gravitationally-transported material (Raška & Oršulák, 2009; Pawlik, 2013).

Once blocks are detached from the primary flow, they can be subject to continued biogenic weathering by vegetation types other than trees. Studies of lichen species on volcanic rock indicate that these organisms intensify chemical weathering by an order of magnitude or more compared to surfaces devoid of lichen, reaching a maximum weathering rate of approximately 0.04 mm/year (Jackson & Keller, 1970). Certain species of mosses can also increase weathering rates along rock faces (Jackson, 2015). If the basalt is covered by vascular plants, weathering rates increase again by at least an order of magnitude compared to lichen-covered rock, both at the flow surface and in joints and vesicles (Berner & Cochran, 1998).

2.4.3.4.2 Observations

The free faces and hanging wall fissures of scarps in the forested area of the Koae Fault Zone expose areas where roots of ‘ohi’a trees (Metrosideros polymorpha) have extended into joints and fractures in the primary flow structures of the basalt (Figure 2.12.1. and 6). As these root systems grow near the crests of steep free faces, they disintegrate rock fragments and widen the aperture of the joints and fractures, leading to collapse, topple and transportation of blocks and, eventually, of the trees themselves downslope. We also observe trees on the mid-slopes of scarps, particularly on larger (20m+) scarps, such as the Western-juniper-dotted scarps of Medicine Lake Volcano, CA (Figure 2.12.5.) These trees, averaging approximately 7 m in height along LVBD-A, are situated in patches of shallow soil along rocky slopes, consisting of either primary layered flows or secondary talus. In the case of LVBD-A, the trees are sparsely spread out and the soil cover is patchy, suggesting that tree cover might not be an important factor in slope stability as a whole for the scarp at its current stage. However, we do see evidence of tree damming along the forested sections of the scarp, with cobble- to large-boulder-sized material found upslope of the juniper trees (Figure 2.12.5.)

Other vegetation also influences the weathering and transport of sediment across these volcanic scarps. We observe root systems of smaller shrubs and bushes such as ‘ōhelo in Hawai’i, ferns in Iceland or sagebrush and bitterbrush in northern California developing in soil accumulated in fractures (Figure 2.12.2.a.). Moss cover was extensive at the Icelandic sites, subduing small-scale heterogeneities in profile form. We observed the presence of extensive lichen cover at several sites, particularly in Iceland and northern California. At those sites, we could identify isolated areas where centimeter-scale flaking of the bedrock surface had occurred, probably due to lichen-driven biogenic weathering.

2.5 CONCEPTUAL MODELS OF FAULT SCARP EVOLUTION IN FRACTURED VOLCANIC ROCK FOR A RANGE OF VOLCANO-TECTONIC SETTINGS

We have grouped the scarps in our study according to their age, which coincides with geographic location, and thus tectonic and volcanic setting. By leveraging our documentation of processes active in each setting, we can construct a conceptual model of how scarps initiate and evolve for the specific setting of each of the five scarp groups. The value of this approach is that we can identify which elements of scarp evolution are setting specific, versus those that apply to the evolution of fault scarps in jointed rock in all settings.

Two parameters that vary consistently between groups are the rates of scarp growth and of volcanic resurfacing. We suggest that the interplay between these rates is a useful metric in characterizing the setting of the fault scarp, since this relationship plays an important role in determining the geometry of the fault zone, the maximum height that the scarp can attain, the length of the timescale during which processes can be active, and thus the types of geomorphic processes that will modify scarp form throughout its lifetime. Other parameters that can vary between sites include rock mass characteristics (influenced by effusion rate), climate and vegetation.

2.5.1 Scenario 1: High rate of resurfacing volcanic flows and high scarp growth rate

In this scenario (Figure 2.13), repeated periods of volcanic activity have obscured the total offset, number and/or geometry of the original scarps. Individual flow volumes and effusion rates are relatively low. Structurally, initial scarp growth is characterized by the development and growth of en echelon dilatant fractures, ranging from 10s to 100s of meters, and the growth of monoclines linking the fractures. The ratio of the length of the longest fracture relative to the total fault zone length is small, given the structural influence of the buried faults. The presence and

geometry of monoclines can be variable along strike of the scarp. The profile form of the scarp is mainly controlled by the amplitude and limb dip of the monocline, if present, and the aperture of the fissure created by dilatant fractures, as well as any flow top features (e.g., tumuli) that might be present.

As fractures link, grow and start accumulating vertical offset, scarp free faces become recognizable in profile form and expose lateral heterogeneities caused by multi-lobed pāhoehoe architecture. These heterogeneities can create areas that are more susceptible to modification than others. If the fault is accumulating slip seismically, ground shaking can amplify this variability through rockfall and toppling. Monocline limbs steepen and can create a brecciated zone at their toe as the structure grows. Small translational slides initiate along planes of weakness in the basalt flows. These slides become a locus of physical and chemical weathering, as the vitreous and reactive flow tops are dammed by coarser slide material and disintegrate into smaller particles that fill in depressions. At relay zones, relay ramps are breached as larger segments join, creating a characteristic double-peaked scarp profile. Isolated trees and shrubs grow in patches of accumulated soil, accelerating rockfall through tree root action at the crest of the scarps.

In this scenario, the structural and geomorphic processes described above happen between periods of resurfacing. In the case of Koae Fault Zone, where temperatures are consistently warm, precipitation is sporadic but high and regional extension rates are approximately 10mm/year, that timescale is on the order of hundreds of years. Scarps reach heights on the order of 10s of meters before resurfacing occurs. Scarps are not necessarily completely resurfaced with every flow: evidence of flow draping and abutting is abundant in the area.

2.5.2 Scenario 2: Mid-range rate of resurfacing volcanic flows with high to mid-range scarp growth rate

In this scenario (Figure 2.14), volcanic flows interact with the scarp and can occasionally resurface it, but longer periods of time elapse between large-scale eruptions. Flow volumes are larger, often resulting in complete resurfacing, without the evidence for scarp-flow interactions at the surface found in the Koae Fault Zone. Effusion rates are also relatively high. Volcanic resurfacing is evident in the overall fault zone morphology: the ratio of the length of the longest fracture relative to the total fault zone length is comparable to that scenario 1 and the maximum scarp height within a flow of certain age increases with age. Monoclines, free faces and fissures are all features identifiable in scarp profile morphology, but monoclines tend to be discontinuous and are situated at the fault tips and sporadically along the scarp segments, potentially due to the location of antithetic faults (Bubeck et al., 2018). As scarp height increases, monoclines become steeper, reaching angles of up to 35°, before undergoing collapse, rendering it difficult to distinguish between monocline and talus.

The ratio of resurfacing to scarp growth for these scarps is similar to that of scenario 1, resulting in scarps of comparable heights (tens of meters). Differences in profile form are explained by differences in flow type and thickness and geomorphic processes related to climate (e.g., frost weathering, soil development through biogenic weathering by moss). The rock mass hosting the Icelandic scarps is characterized by high volume pāhoehoe sheet flows, allowing for fewer horizontal discontinuities and larger overall joint spacing than that of the Koae Fault Zone scarps. Blocks are released from free faces during ground shaking events and form small debris piles where the size of the blocks is relatively large compared to the overall size of the scarp. Frost wedging also serves as a mechanism to initiate rockfall and it further decreases the block size of debris. The widespread growth of moss, ferns, grasses and, to a lesser extent, lichen accelerates

chemical weathering rates (Jackson, 2015) and reduces the roughness of scarp profile forms when vegetation infills the cavities between blocks in the talus. Examples of these scarps include Sodulholagja (3 ka since the last major flow), Gildruholtsgja (approx. 7 ka) and Nydri-Mosadalagja and Stora-Aragja (more than 12 ka).

2.5.3 Scenario 3: Low rate of resurfacing volcanic flows and high scarp growth rate

In this scenario (Figure 2.15), fault slip rates are high, scarp growth rates are high, but rates of volcanic resurfacing are low. The Hilina Fault Zone is accommodating a minimum of 10 mm of extension per year and is primarily made up of flows older than 23 ka. As in scenario 1, flow volume and effusion rates are relatively low. More recent flows drape the scarp, and evidence of these flows can be apparent in profile form (e.g., the relatively high relief of the ʻaʻā flow at the base of the southwest edge of the Hilina Pali), but they do not significantly reduce the total height of the scarp. Pāhoehoe flows tend to mantle the scarp, whereas ʻaʻā flows tend to mass at the base of the scarp, creating a toe visible in profile morphology.

Rapid scarp growth and low rates of resurfacing allow for scarp relief to increase to the scale of hundreds of meters, leading to different modification processes affecting scarp profile form than in the first two scenarios. The increasing gravitational potential energy of material on the scarp is relieved first through rock fall, then through rockslides, triggered by frequent strong ground motions from earthquakes on the fault and nearby, gravitational stresses and heavy rainfall or wind action. Given the very large height of the scarp relative to the size of a joint bounded block, rock mass characteristics matter little to scarp form at the scale of joints or lobes, but can be an influence at the flow scale, when inter-flow units act as planes of mechanical weakness. Any draped flows contribute to an increase in material susceptible to mass wasting events. Bedrock channels are carved through episodic heavy rainfall in the Kau Desert. These channels become

over steepened and cut through the loose material accumulated on the talus slope, triggering larger mass wasting events such as rock avalanches and debris flows. As loose material accumulates and is reworked on talus slopes, climatic events can trigger debris flows, increasing the concavity of profile form.

2.5.4 Scenario 4: Low flow resurfacing, low scarp growth rate

In this scenario (Figure 2.16), fault slip and scarp growth rates are relatively low, but volcanic resurfacing rates are low as well, allowing the scarp to accumulate relief over a much longer time scale, as is the case for the Gold Digger Pass and Crumes Lake scarps. The structural maturity of the system is signaled by the long fault segments relative to the overall fault length, as smaller segments become hard-linked. Structural features (e.g., monoclines or breached relays) are obscured by rockfall accumulating at the base of the scarp. The accumulation of talus deposits takes more time, since there are fewer earthquakes, so strong ground motion is less of a trigger for rockfall than at the other sites. Thermal weathering is a candidate for rockfall triggering, given the diurnal variation in temperature and low winter temperatures in this section of the Modoc Plateau desert. Inter-flow units, such as the Antelope Well tuff, precondition certain parts of the scarps to translational slides. Relict relay ramps persist in the scarp profile morphology, even in areas of increase rockfall. As the scarp grows, it become susceptible to larger mass movement processes. A renewal in volcanic activity is evident in the southern portions of the scarp, where scarp offsets and fault segment lengths are smaller.

2.5.5 Scenario 5: No volcanic flow resurfacing, low to mid-range scarp growth rate

In this scenario (Figure 2.17), scarps are not resurfaced by younger volcanic flows, since faults propagate through one large volcanic flow complex (the Bishop Tuff). The scarps thus

record a continuous history of extension. This is reflected in the overall fault structure: the total length of the fault zones is smaller than that of the scarps of the other groups, but the individual fault segments within the fault zone are also larger. The record of scarp degradation is also continuous. Given the difference in lithology to the basaltic sites, joint-bounded blocks are larger and thus the importance of individual blocks in affecting profile form remains important even as scarps reach height of 50+ m. These blocks do disintegrate over time, mainly through mechanical weathering processes, but the form of the scarp tends to be dictated by the structural evolution and the action of larger blocks.

2.6 Synthesis – Discussion

In this study, we motivate the characterization of fault scarp evolution in jointed volcanic rock by the success in establishing models for scarp degradation in granular materials and in limestone. An important element to synthesize from our observations is thus determining an equivalent conceptual model for the degradation of fault scarps in jointed volcanic rock, using scarps of equivalent scale. The models used for scarps in granular materials and in limestone are 2-D models applied to a scarp profile where the slip plane of the fault is identifiable or known, that were formed by one or a few earthquakes, rarely reaching a height of more than ten meters. A first complicating factor in the case of jointed bedrock scarps is the absence of an identifiable fault slip surface that is coherent with overall fault dip. Our field studies yielded no observations of slickenlines, or other indications of a coherent fault slip plane. This is consistent with work indicating that faults in jointed volcanic rock propagate to surface through fractures that are often dilatant (e.g., Ferrill et al., 2011; Weismüller et al., 2019) and exploit the pre-existing weaknesses of the cooling joints (e.g. Holland et al., 2006), leading to scarp faces that reflect the geometry of the intersecting joints rather than the dip angle of the underlying fault. Furthermore, the orientation

and density of near-surface fractures and joints relative to the fault influences the width of the deformation zone and the topographic expression of the scarp (Hilley et al., 2001), resulting in multiple initial scarp forms for a single fault depending on the rock mass and regional tectonic stresses. This complicates evolution models, since the initial scarp form, even if one excludes structures such as monoclines or fissures, is not easily predicted.

To manage this complexity, we can make some simplifying assumptions and use commonalities between scarp groups to determine the likely form of a simple (single or just a few earthquakes) scarp and the processes that act upon it. We first assume in the conceptual model that no further scarp growth events or scarp-volcanic-flow interactions occur. The model is thus only reflecting a period of scarp degradation, with only geomorphic modification considered. We determine scarps that are appropriate comparisons to the smaller scarps of the other models, using a maximum scarp height cutoff of 15 meters, which yields two Icelandic scarps (Stora-Aragja and Nydri-Mosadalagja) and one scarp from the Koae Fault Zone (the Ohale Fault scarp). The simplest shared profile form between these three scarps, taken away from complicating structures and geomorphic or volcanic modification, is a steep free face. As documented in section 4.1.2., variation in profile form of these free faces is accounted for by rock mass characteristics. Figure 2.18 presents a conceptual model of how a simple free face in jointed rock evolves, based on the ratio of joint spacing to scarp height (as dictated by volcanic effusion rates), frequency of rockfall (high or low) and degree of mechanical and chemical weathering. We populate the conceptual model with profile forms adapted from our observations of the three selected faults, as well as

from the other scarps in our study where certain mechanical and chemical weathering processes were more active.

Rock mass characteristics coupled with the frequency of rockfall are the most important factors in determining final scarp form. Where vertical joint spacing is almost equal to scarp height, topple of single blocks can occur if the scarp is subjected to groundshaking from nearby earthquakes (Figure 2.18.i.). The toppled block is subject to mechanical weathering processes (iii) (e.g., subcritical cracking driven by diurnal changes in temperature) and minimally to chemical weathering processes, but the size of the block offers a limited reactive surface. If no groundshaking occurs in the area, mechanisms initiating rockfall using smaller amounts of force (e.g., root or frost wedging) are unlikely to topple scarp-height blocks (ii), so the scarp form will persist through time, modified minimally by sources of mechanical (iv) and chemical weathering (vi) (e.g., lichen, chemical breakdown of flowtops).

At the other end of the rock mass spectrum, we have free faces containing many lobes and thus densely spaced joints, with a low ratio of horizontal joint spacing to scarp height. Rockfall frequency remains the most important predictor of scarp form. With high rockfall frequency, the more readily available fallen blocks form a talus slope, while the free face recedes in a stepped fashion, retaining a short free face at the top of the scarp. Rockfall is hindered once the talus reaches the highest joint-bounded block in the free face capable of toppling. This height depends on the force of the rockfall mechanism, the geometry of the block and the density of the material. At this point, the effects of mechanical and chemical weathering processes can be seen on scarp form, first breaking down the subaerial portion of the talus and smoothing the profile.

This conceptual model is rooted in the idea that rockfall so thoroughly disrupts profile form that smaller-scale processes, such as mechanical and chemical weathering, can be ignored while

rockfall is active. The profile experiences rockfall through time until rockfall is no longer possible, due to either the regional settings (e.g., earthquakes activity ceases) or profile geometry (e.g., a wedge of fallen blocks impedes the topple of another). The transition to mechanical weathering as the dominant process affecting scarp form is thus a transition to a later stage of scarp degradation, where fallen blocks are broken down. This leads to the final degradation stage, where chemical weathering processes alter the products of mechanical weathering. Difficulty remains in assigning ages to these stages. We find similar free face profile forms in both Vogar and the Koae Fault Zone, even though the Icelandic scarps are thousands of years older than the Hawai'ian ones. However, each region experiences different amounts of groundshaking, annual and diurnal temperatures, amount, frequency and type of precipitation and types of vegetation, which could lead to different processes dominating for different amounts of time, resulting in similar profile forms for scarps of different ages. Similarly to scarp diffusion in granular materials and scarp relaxation in limestone, parameters quantifying the environmental conditions are required for in any future quantitative model of scarp degradation in jointed bedrock. Specifically, the frequency and volume of rockfall events and the rates of mechanical and chemical weathering need to be parametrized. Given the importance of rock mass characteristics in influencing patterns of rockfall, a quantitative model will also require refining a physical model of scarps in jointed volcanic rock over a range of joint spacings. Complex dynamic analyses are now possible with modern computer hardware and software, but detailed descriptions of the block shape and mechanical properties are needed to avoid large errors (Fityus et al., 2013). These detailed descriptions are possible with

techniques such as SfM photogrammetry (e.g., Sarro et al., 2018), but need to be incorporated into a larger framework of scarp rockfall models to avoid over-fitting to specific sites.

The conceptual model discussed above responds to the need for an explanation of the degradation of simple fault scarp profiles in jointed rock in small scarps with no renewed volcanic or tectonic activity. However, our study highlights the three-dimensional complexity of fault scarps in jointed volcanic rock: an initial profile form that varies along strike of the scarp, continued growth events which simultaneously trigger rockfall, interactions between scarps and volcanic flows and multiple processes that can be active concurrently over different temporal and spatial scales. Furthermore, scarps in jointed bedrock persist in landscape through time as unique landforms, the result of tens to hundreds of growth events and thousands to millions of years of geomorphic and volcanic modification (e.g., Hilina Pali or Crumes Lake Scarp), compounding these complicating factors. We aim to address this complexity by integrating profile observations across the entire scarp, rather than focusing on the evolution of a single profile. By observing the patterns in scarp profile form of a single scarp at a single time step, we can infer the processes that influence scarp form at this stage and how they might change as the scarp evolves. In all five of our scenarios, the initial variation in scarp profile form was governed primarily by fault structures (monoclines, fissures, relay ramps) and secondarily by rock mass characteristics (e.g., free faces being more or less heterogeneous based on flow lobe structure). Structure thus sets the initial variability, and this variability is semi predictable, based on the tectonic context (e.g., shorter scarp segments relative to fault zone length in resurfaced areas or continuous monoclines in the Koae Fault Zone). This initial variability sets the stage for the next step in scarp evolution, as rockfall and small-scale sliding concentrates in areas where structures have made the scarp more unstable (e.g., slides off of steepened monoclines, collapse of breached relay ramps, topple of overhanging

free faces). This geomorphic action first increases morphologic variability, then decreases it, as rockfall buries the initial structures. This interplay between structure and rockfall occurs repeatedly throughout the active lifetime of the scarp. Between growth events, rockfall is still possible, but talus processes and mechanical and chemical weathering can also act on scarp form, smoothing out profile form and decreasing the scarp's overall morphologic variability through time (e.g., northern section of Gold Digger Scarp). Heterogeneity can be introduced yet again as scarps become very high and mass wasting events introduce increased morphologic variability on a broader scale (e.g., Hilina Pali or Crumes Lake Scarp). Throughout the lifetime of the scarp, volcanic activity can decrease (e.g., draped flows that smooth rock slope or mask structures) or increase morphologic variability (e.g., draped flows can be brecciated or be the locus of mass wasting). Furthermore, the ratio of fault slip rate to volcanic resurfacing rate sets the maximum height that the scarp can attain, which has implications for the types of processes that can be active upon it and their effect on the scarp's morphologic variability and the structural maturity of the fault zone.

This cross-scarp conceptual model of the evolution of fault scarps in jointed volcanic rock also lays the groundwork for quantitative studies of scarp in jointed volcanic rock. The parameter space for a quantitative model would be defined by climate (which influences the types and rates of geomorphic processes acting on the scarp), lithology (which influences the joint patterns, and thus block size and weathering rates and products) and the ratio of fault slip to volcanic resurfacing rates (which would in turn set the fault zone structure, the scarp maximum height, the relationship of block size to scarp height and the modification processes likely to influence scarp form). The model output would have to summarize the morphologic patterns expected with the selected parameters. Given the wide variety of parameters and the complexity of their relationships, a

statistical approach using existing scarp data to train a model, rather than a numerical model, might be the most feasible avenue to produce a quantitative study of scarp evolution in jointed volcanic bedrock. A "morphologic variability metric" that quantifies profile form variability along a linear landform, could describe the morphometric patterns associated with different parameter settings (e.g., Brigham and Crider 2022). Future work would include calculating the morphologic variability for scarps across the parameter space to serve as the basis for classifying scarps with unknown parameters. Eventually, this model could be calibrated by cosmogenic exposure dating of both scarp growth and modification events (e.g., 3He exposure dating of scarp-forming events in Schwartz et al., 2022).

The applications of such a quantitative model based on the conceptual framework described here would be far-reaching, allowing for semi-automated analyses of fault scarps in complex settings using remotely-sensed data. Settings that could benefit from such analyses include subaerial regions on Earth where neotectonic activity remains not well constrained (e.g., central Oregon: Bacon & Robinson, 2019; Vadman & Bemis, 2019), submarine fault scarps (e.g., Hughes et al., 2021; Vega-Ramírez et al., 2021) and other planetary bodies such as Mars (e.g., Watters et al., 2016; Senthil Kumar et al., 2019; Watters et al., 2019), the Moon (e.g., Kumar et al., 2019; Watters et al., 2019) or Mercury (e.g., Banks et al., 2015; Watters et al., 2016).

2.7 CONCLUSIONS

By synthesizing field observations of fault scarps in five different settings, analysis of remotely-sensed data and previous research on fault scarps and related processes, we have constructed a framework to understand the evolution of fault scarps in jointed volcanic bedrock. The processes that most affect scarp form change throughout the lifetime of the scarp, introducing

more or less morphologic variability along the scarp, and the stage of evolution can be assessed by observing the lateral variation in profile form across the entire scarp. The relationship of tectonic activity to volcanic resurfacing sets the length and height scale of the overall scarp, determining the scale of the geomorphic processes, which vary by climatic setting, that will be influential on scarp profile form.

If scarp growth rates are similar to resurfacing rates (scenarios 1 and 2), maximum scarp height will be capped at a certain value and scarps will be subject to similar processes throughout the lifetime of the fault zone. The Koae Fault Zone and the Icelandic scarps both had maximum scarp heights of approximately 20 m, resulting in fault zone structure, rock mass characteristics and small scale rockfall being the most important processes affecting scarp form. To a lesser extent, both groups underwent mechanical and chemical weathering in the periods between scarp growth and resurfacing but differed in the amount of time upon which these processes had to act and their climatic setting. The Koae Fault Zone scarps are in a climate conducive to more rapid chemical weathering rates than the Icelandic ones, but a shorter window between growth and resurfacing events leads to a lower degree of soil production. Differences in vegetation cover also account for morphologic differences between these two groups (e.g., the presence of ‘ohi’a trees in Hawai’i accelerating rockfall vs. extensive moss cover in Iceland changing profile form and accelerating chemical weathering).

If scarp growth rates are high and volcanic resurfacing rates are low to moderate, scarps increase in height quickly and reach larger maximum heights than in the previous scenarios. The scale of the processes that influence scarp form will thus increase at the pace of scarp growth. The Hilina Pali has a maximum height of approximately 500 m, and thus the processes that impact its profile form tend to be large mass-wasting events (e.g., debris flows and rock avalanches).

Volcanic activity still affects scarp form through draping flows that can either armor hillslopes against further geomorphic modification or be the locus of initiation of slides. Fault structures such as relay ramps and monoclines are quickly breached, buried and obscured by volcanic flows and geomorphic modification.

If there is little to no volcanic resurfacing or even lava flow interaction with the scarps and scarp growth rates are low to moderate, the scale of the processes affecting scarp form will again follow the scale of scarp growth, but the scarp will record a continuous history of growth and fault structures, such as relict relay ramps, are more likely to be preserved in scarp profile form. This is the case for the scarps in Bishop and a large portion of the Modoc scarps. Differences in profile form between scarps of the same height/growth stage are accounted for by differences in rock mass characteristics (e.g., the large joint bounded blocks of the Bishop Tuff explain how individual rock fall events impact scarp form even as scarp heights reach 50 m) and vegetation.

Our conceptual models of fault scarp growth in jointed bedrock highlight the variety of factors that determine scarp form and the complexity of their relationship to each other. However, a path forward is possible with an understanding that dominant modification processes tend to change with time in scarps in jointed volcanic bedrock and that profile form changes with it. By first establishing the relationship of fault slip to volcanic resurfacing, then the scale of the processes likely to influence scarp form, then the types of processes available given the climatic setting, we can properly contextualize which processes are likely to influence scarp form. By observing variations in profile form across the scarp, we can attribute process to these patterns and gain an understanding of the evolutionary stage of the scarp.

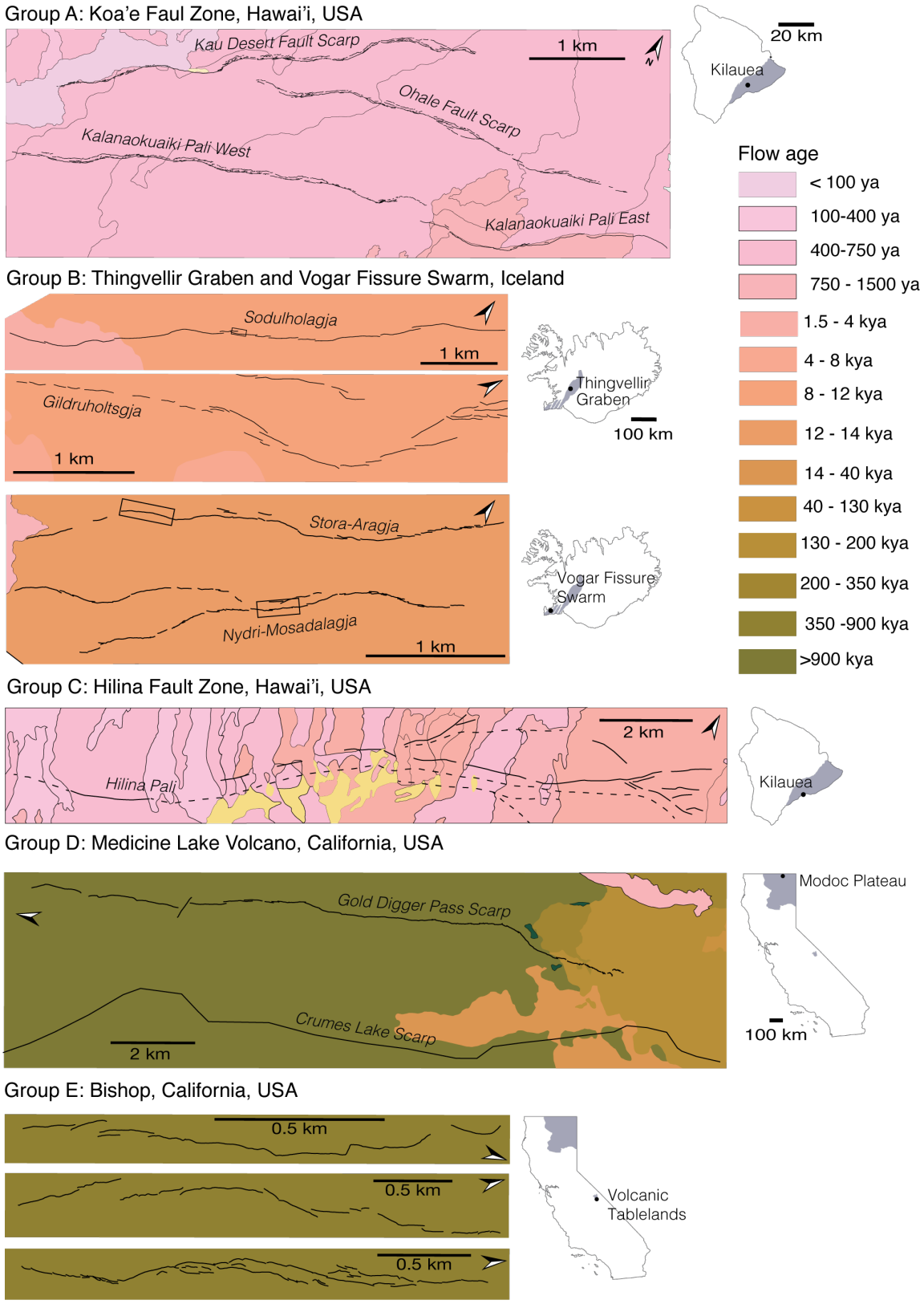

Figure 2.1: Site fault maps with color indicating the age of volcanic flow

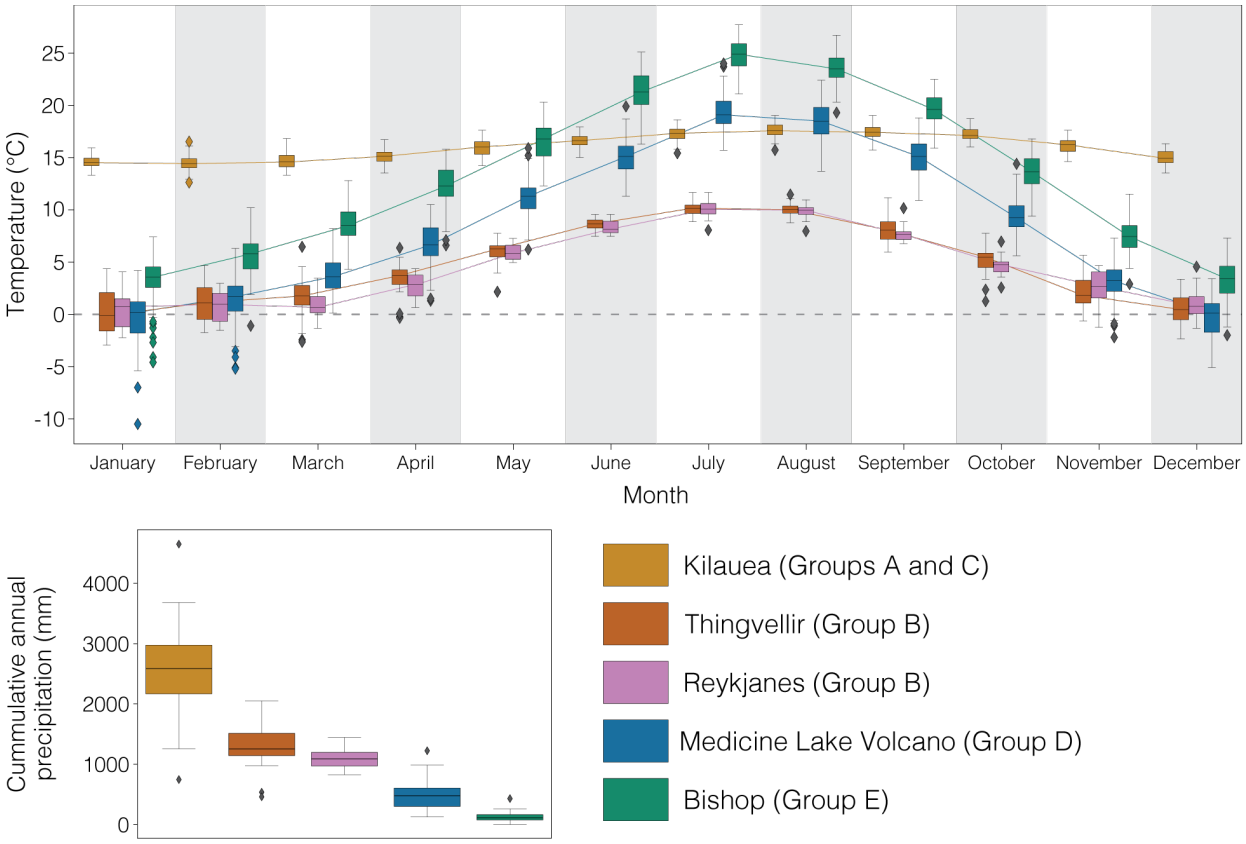

Figure 2.2. Climate data from the five field sites collected between 1960 and 2022 by the National Centers for Environmental Information (Kilauea, Medicine Lake Volcano and Bishop) and the Icelandic Meteorological Office (Thingvellir and Reykjanes). A) Boxplot of average monthly temperature values between 1960 and 2022 from each site (sites identified by color legend below). B) Boxplot of average annual precipitation values between 1960 and 2022 for each site (sites identified by color legend to the right).

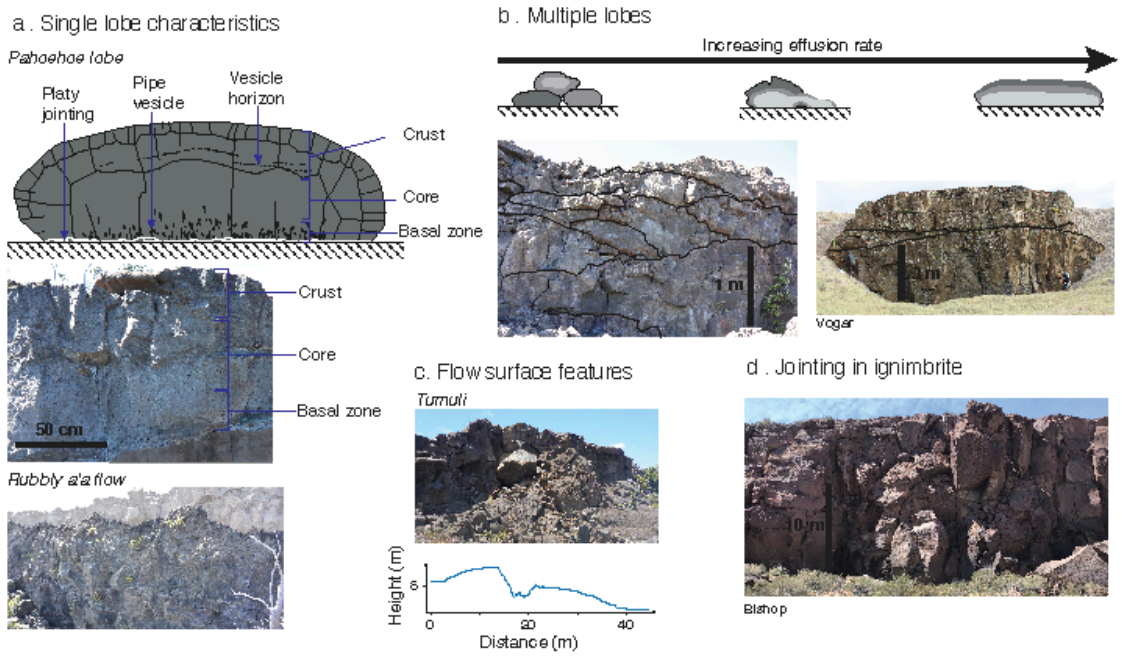

Figure 2.3. Rock mass characteristics of volcanic flows. a. Components of a pahoehoe lobe (above: schematic diagram; below: annotated image from the Ohale Fault scarp) and a rubbly a'a flow (annotated image from the Ohale Fault scarp). b. Above: Schematic diagram illustrating the effect of increasing volcanic effusion rates on lobe morphology (adapted from Self et al., 1998); below: images illustrating multiple-lobe structures from the Kau Desert Fault scarp (left) and Stora-Aragja (right), with black solid lines indicating lobe boundaries. c. Image (above) and scarp-normal profile (below) of a tumulus breached by the Ohale Fault. d. Image taken along RHPS illustrating jointing patterns present in the upper portions of the Bishop Tuff.

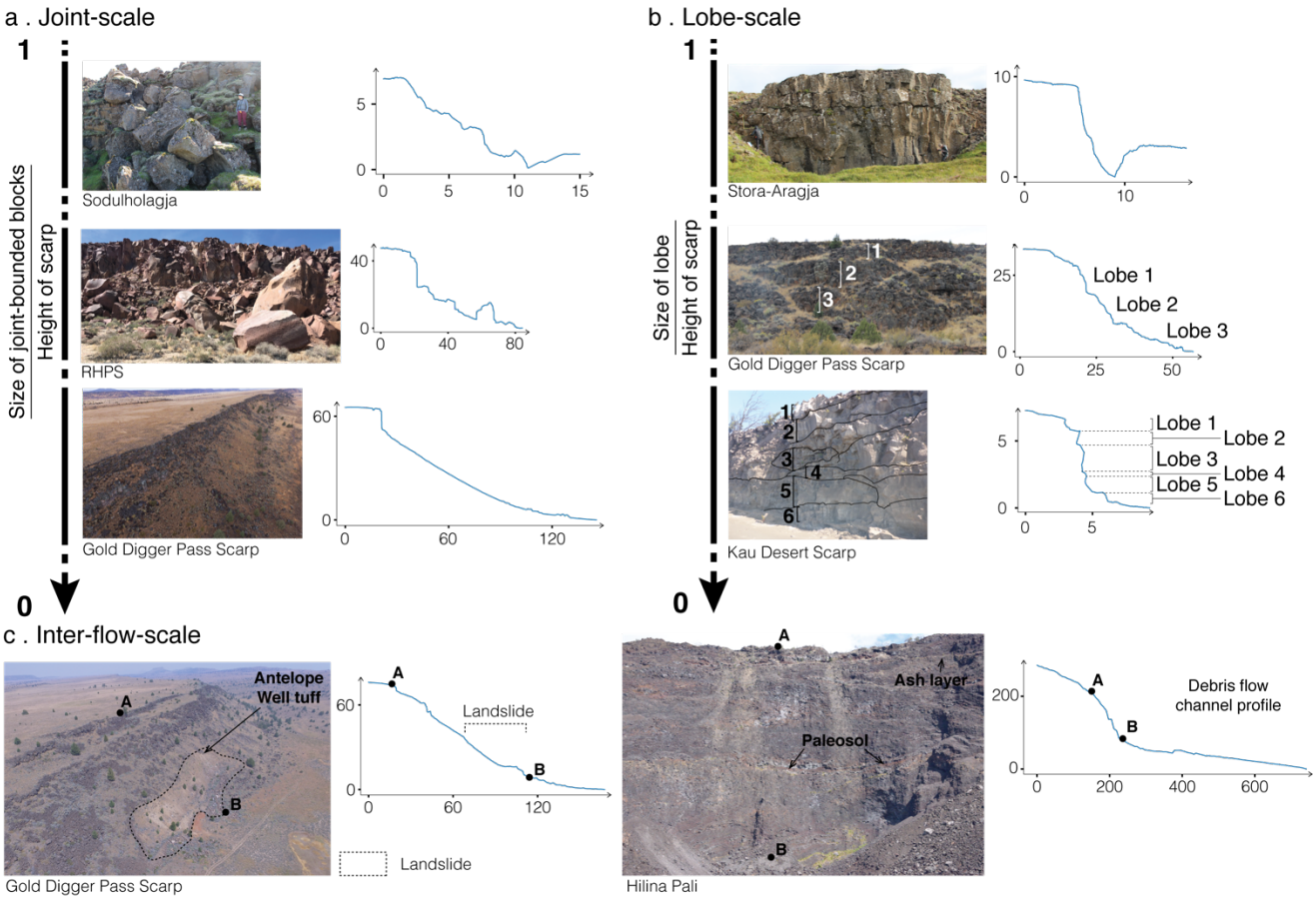

Figure 2.4. Effects of rock mass architecture on scarp-normal topographic profiles a) when decreasing the size of joint-bounded blocks relative to the height of the scarp; b) when decreasing the size of individual lobes relative to the height of the scarp; c) when inter-flow units serve as planes of weakness to facilitate landslides and debris flow channel formations.

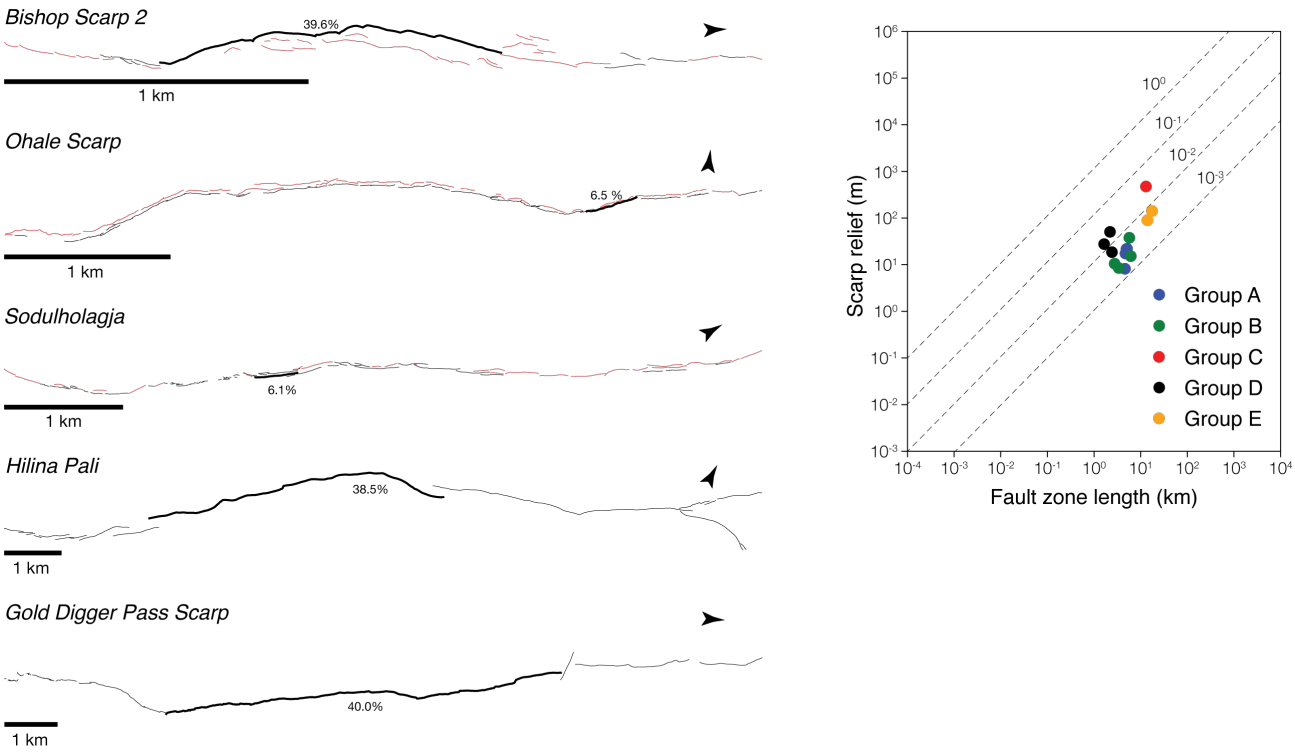

Figure 2.5. Effects of rock mass architecture on scarp-normal topographic profiles a) when decreasing the size of joint-bounded blocks relative to the height of the scarp; b) when decreasing the size of individual lobes relative to the height of the scarp; c) when inter-flow units serve as planes of weakness to facilitate landslides and debris flow channel formations.

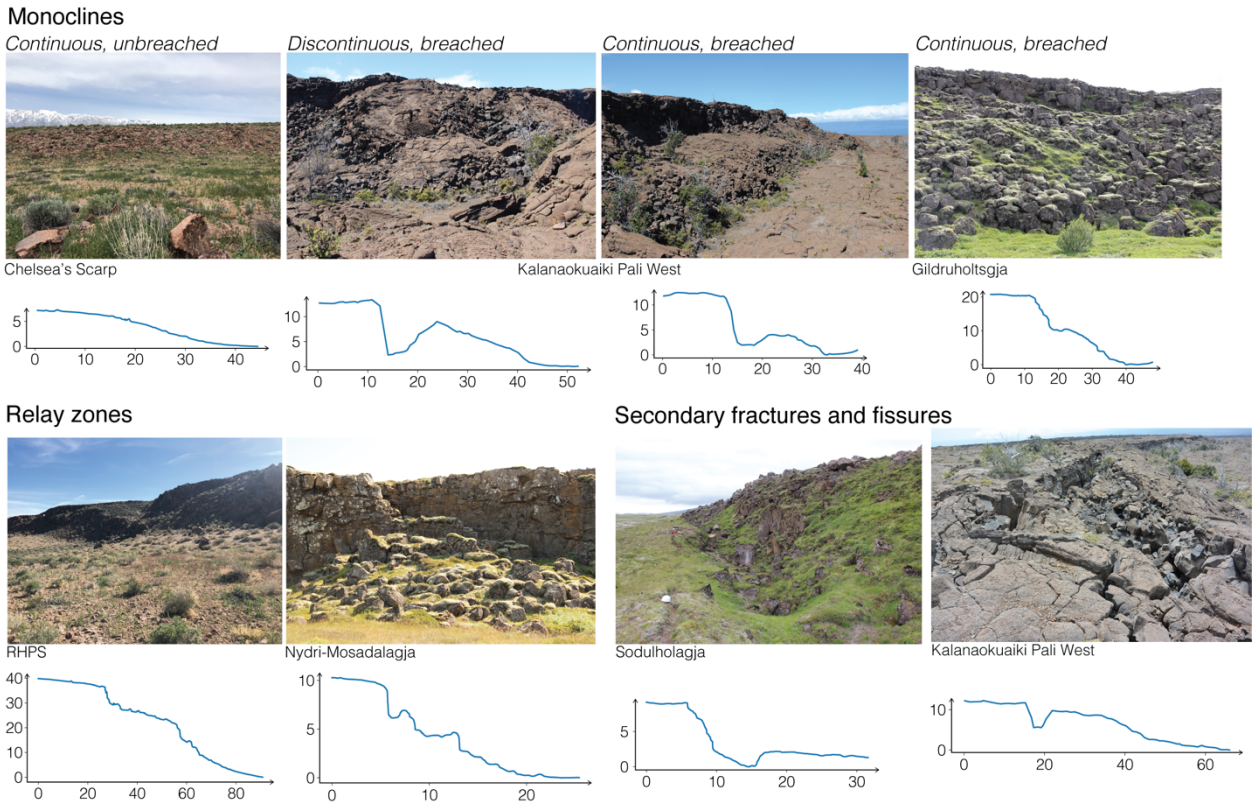

Figure 2.6. Images showing examples of individual fault zone structures (monoclines, relay zones and secondary fractures/fissures) and their associated scarp-normal topographic profiles; scarp names are indicated below each image; the x-axis of each plot indicates height (m) and the y-axis indicates distance along profile (m).

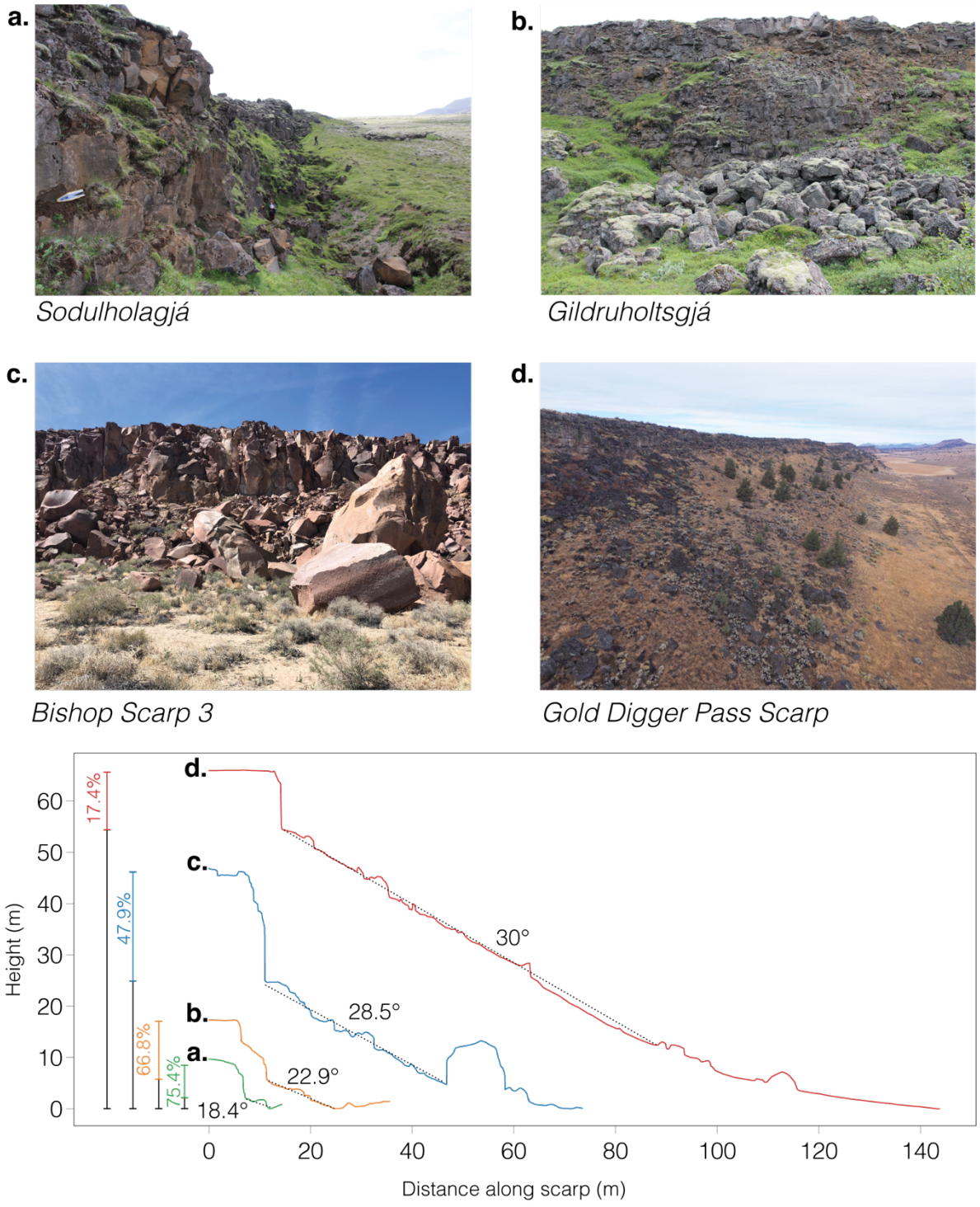

Figure 2.7. Images and associated scarp-normal topographic profiles of rockfall along (a) Sodulholagjá, (b) Gildruholtsgjá, (c) Bishop Scarp 3 and (d) Gold Digger Pass Scarp.

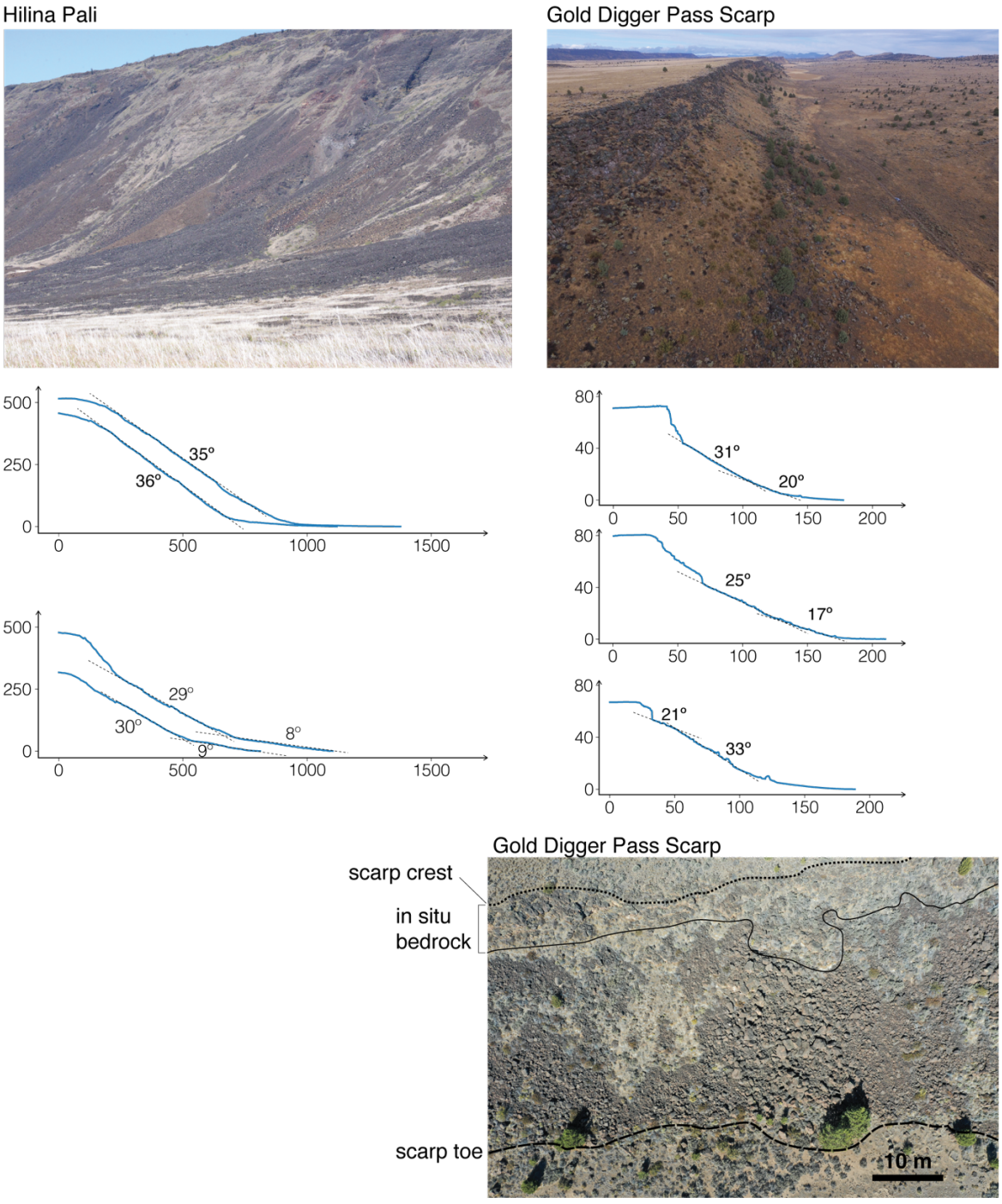

Figure 2.8. Images above show talus slopes from Hilina Pali and Gold Digger Pass Scarp, along with scarp-normal profiles illustrating typical talus slope forms for each area. Below is a UAV-acquired image showing the lateral variability in talus size along a section of the Gold Digger Pass Scarp.

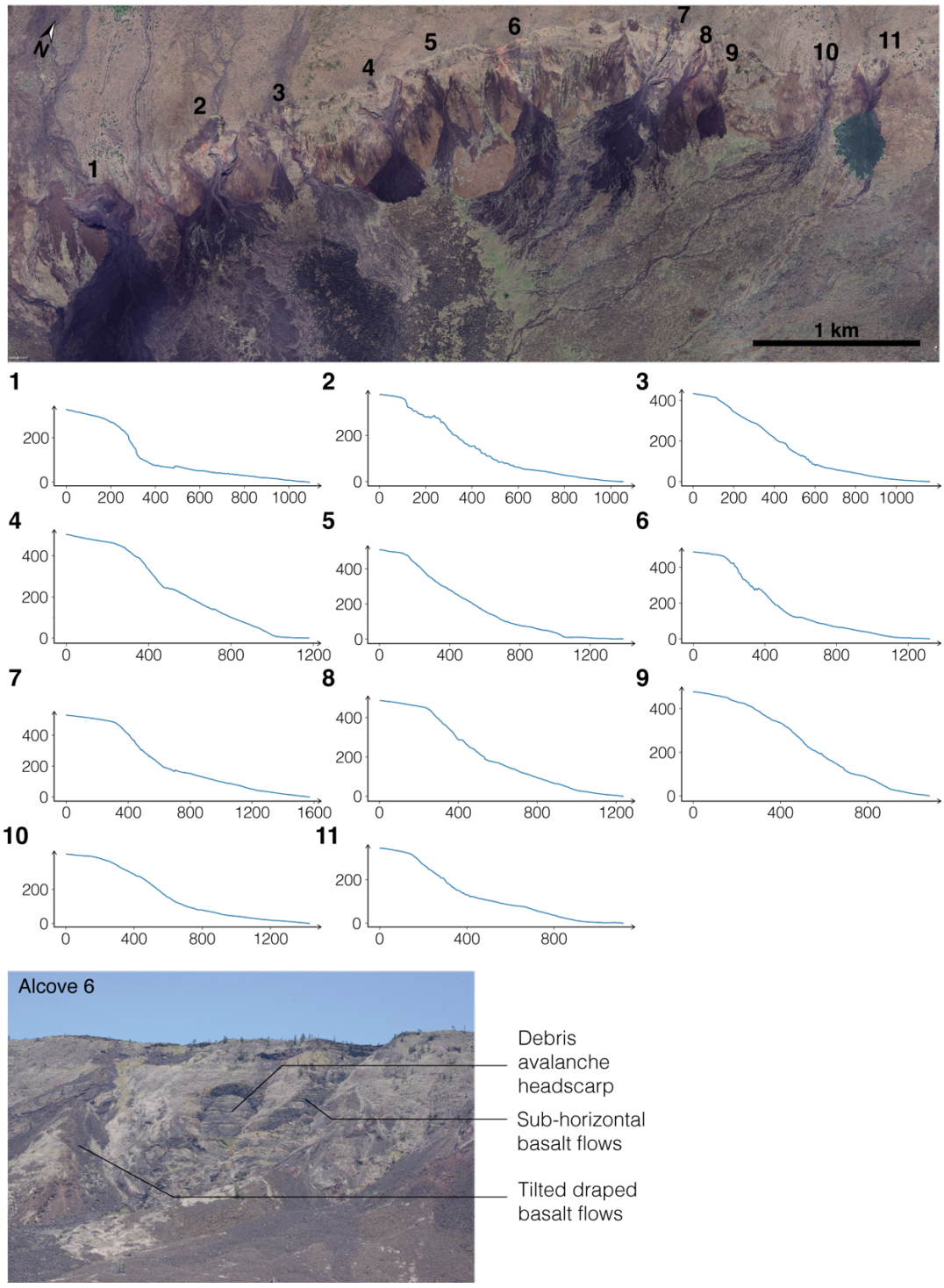

Figure 2.9. Aerial imagery of the Hilina Pali (GoogleEarth) with mass-wasting-created alcoves numbered sequentially West to East. The corresponding profiles are taken perpendicular to the scarp at the location of each alcove (x-axis: distance along profile in meters; y-axis: height in meters). Image below shows mass-wasting features in alcove 6, along with the varied attitude of basaltic flows.

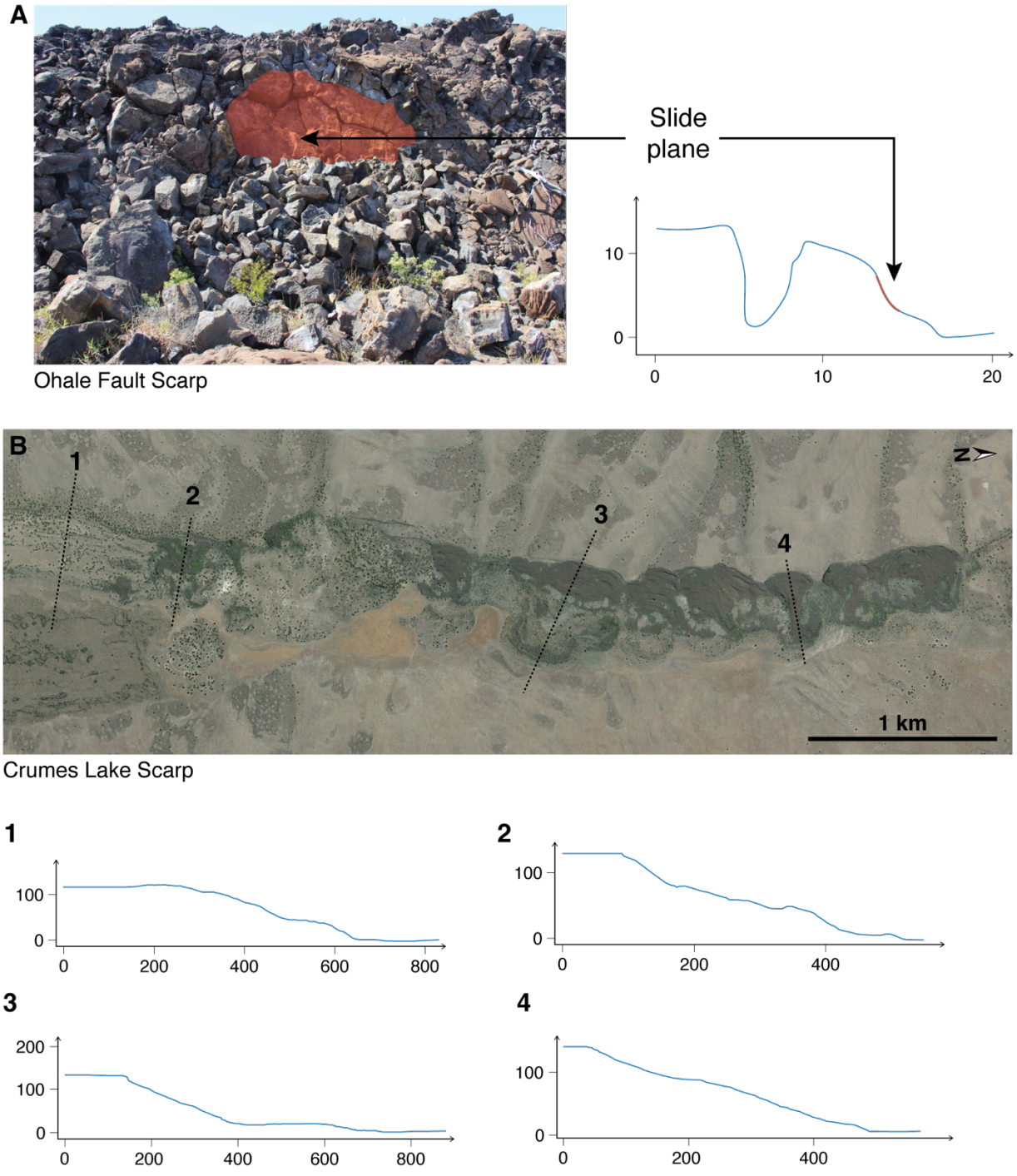

Figure 2.10. A) Shallow translational slide along a monocline of the Ohale Fault Scarp (image and scarp-normal profile). B) Mass-wasting features along the Crumes Lake Scarp (aerial imagery from Google Earth and four profiles taken along the area of interest). All profiles record height on the y-axis (in meters) and distance along the profile on the x-axis (in meters).

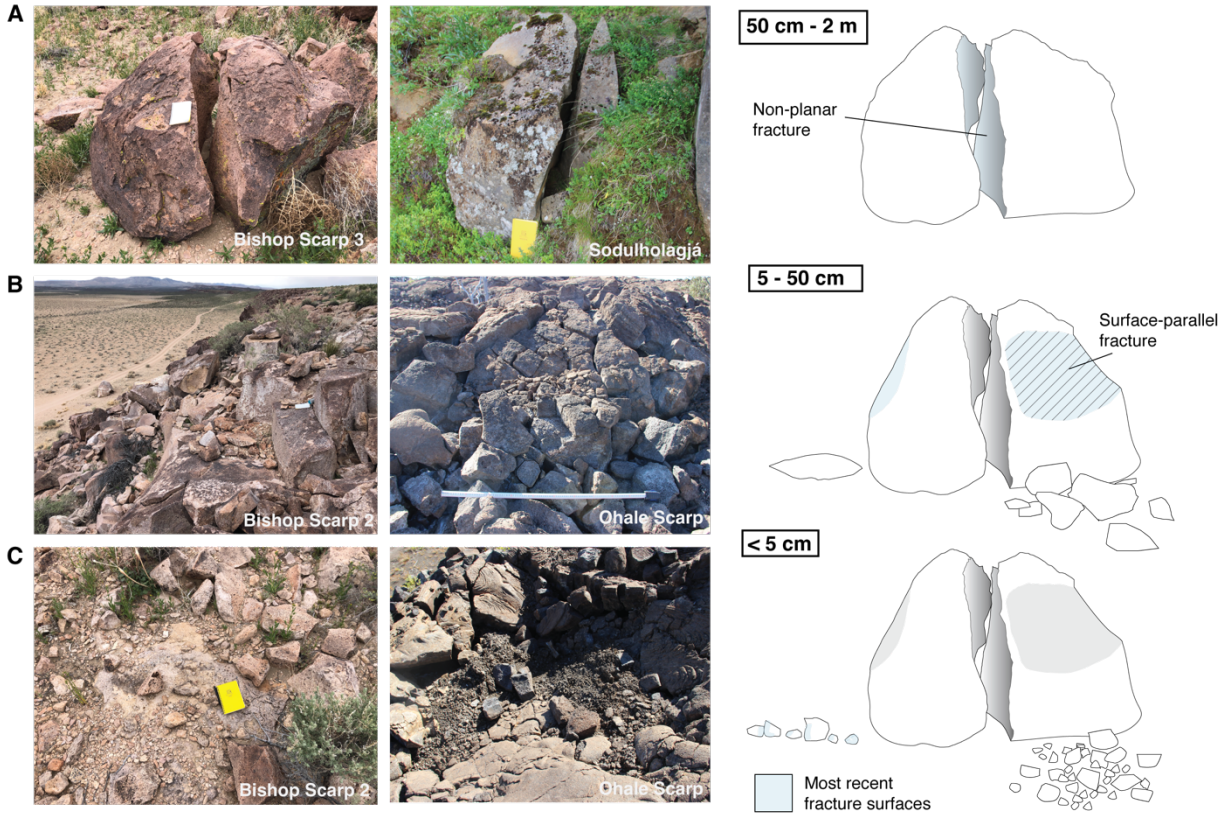

Figure 2.11. Images and schematic illustrations of physical weathering processes present at study sites.

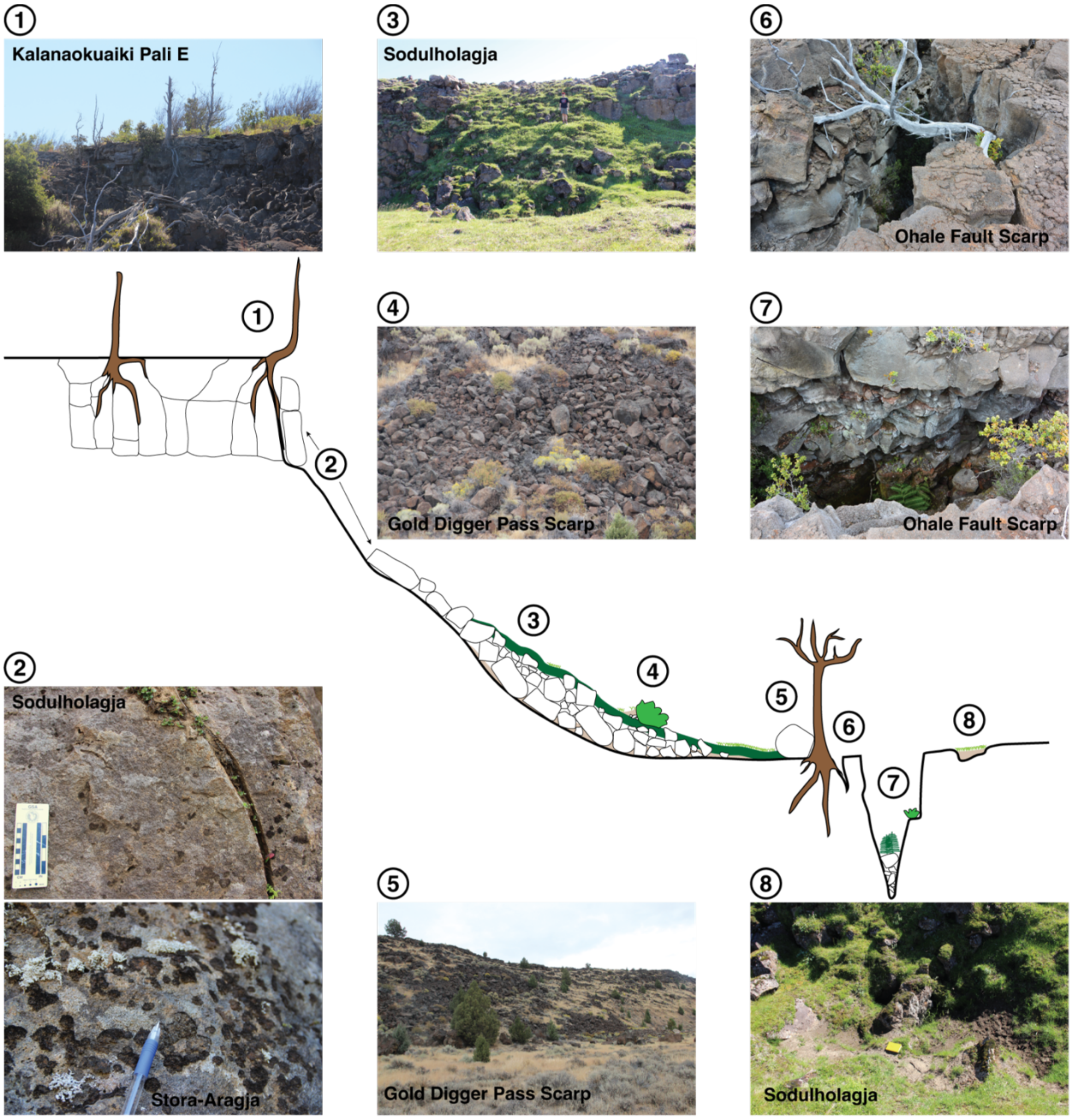

Figure 2.12. Photographs taken at the studied sties (scarp name indicated on image) illustrating vegetation acting on scarp morphology at a variety of scales. Numbers images refer to those on the central schematic drawing, showing the location along the scarp profile where these processes are found.

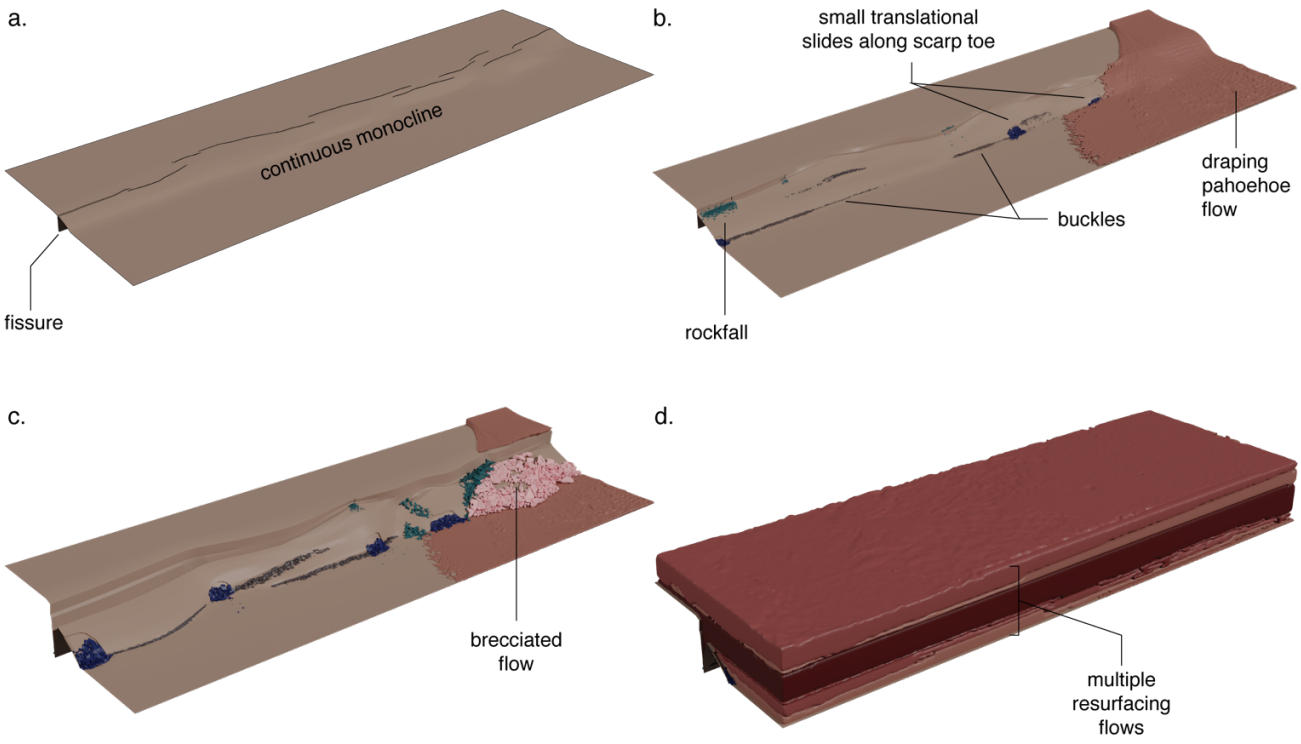

Figure 2.13. Scenario 1: conceptual model of the evolution of fault scarps with high rates of volcanic resurfacing and scarp growth. Model is based on observations of scarps from group A, so it reflects a warm climate with limited vegetation cover and mid-range lava effusion rates that lead to compound, hummocky pahoehoe flows.

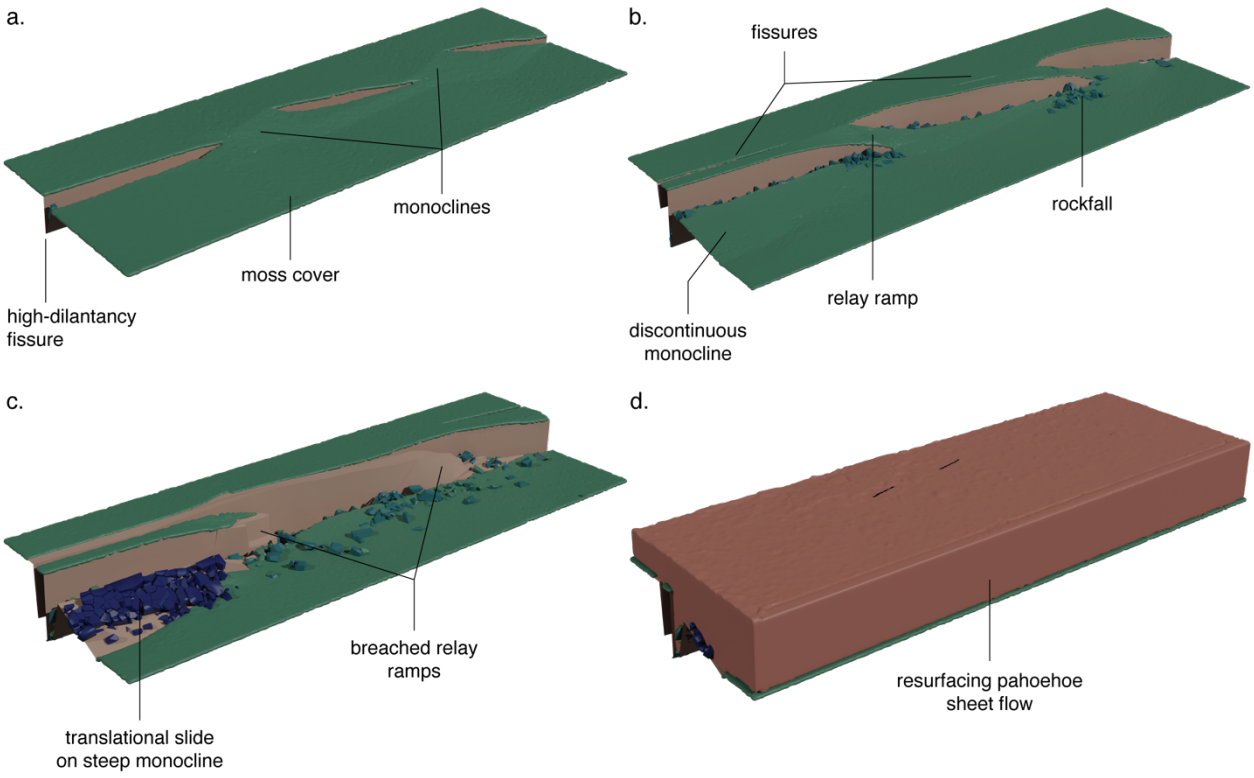

Figure 2.14. Scenario 2: conceptual model of the evolution of fault scarps with mid-range rates of volcanic resurfacing and scarp growth. Model is based on observations of scarps from group B, so it reflects a cold, wet climate with extensive moss cover and high lava effusion rates that lead to pahoehoe sheet flows.

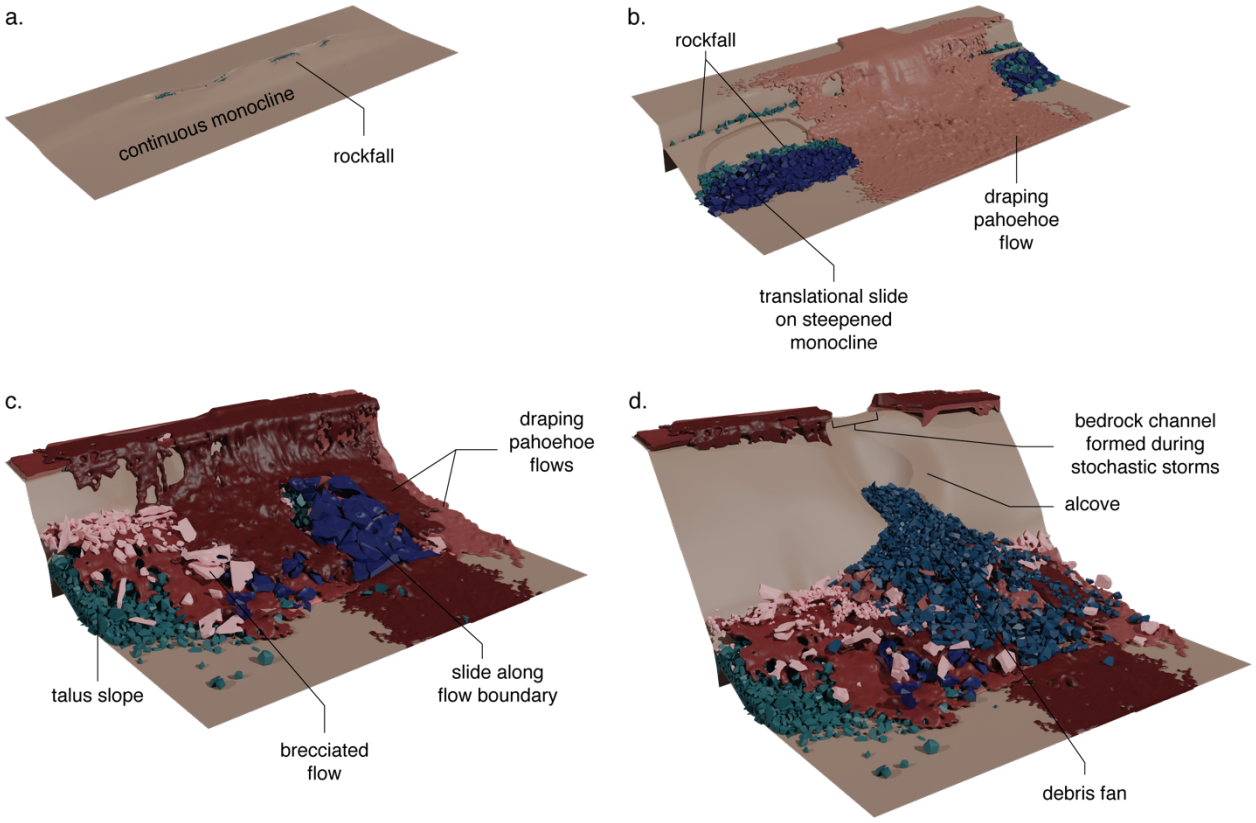

Figure 2.15. Scenario 3: conceptual model of the evolution of fault scarps with low rates of volcanic resurfacing and high rates of scarp growth. Model is based on observations of Hilina Pali (group C), so it reflects a warm, dry climate with stochastic high rainfall events, with limited vegetation cover and mid-range lava effusion rates that lead to compound, hummocky pahoehoe flows.

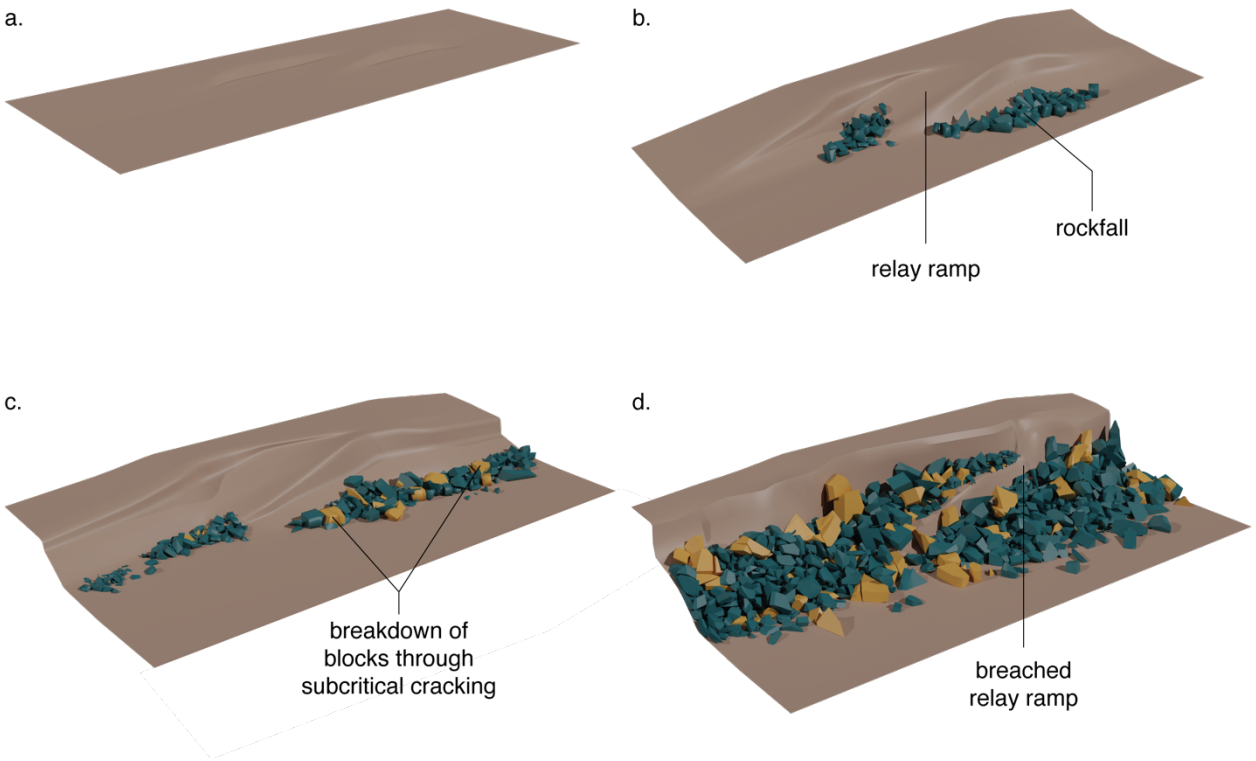

Figure 2.16. Scenario 4: conceptual model of the evolution of fault scarps with no volcanic resurfacing and mid-range rates of scarp growth. Model is based on observations of scarps from group D, so it reflects the consistently larger joint spacing of welded ignimbrite compared to basalt. The diurnal variation in temperature allows for higher rates of subcrititcal cracking.

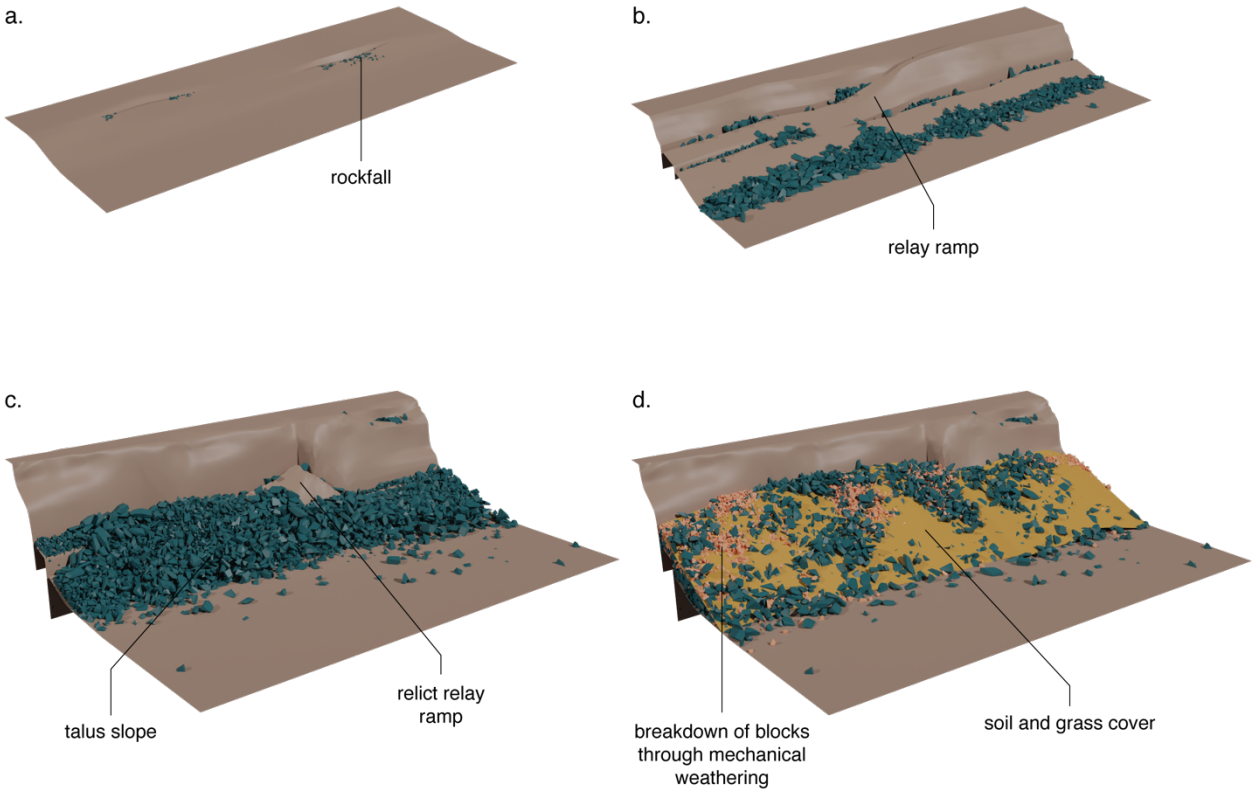

Figure 2.17. Scenario 5: conceptual model of the evolution of fault scarps with low volcanic resurfacing and mid-range rates of scarp growth. Model is based on observations of scarps from group E, so it reflects a dry climate with large diurnal variations in temperature.

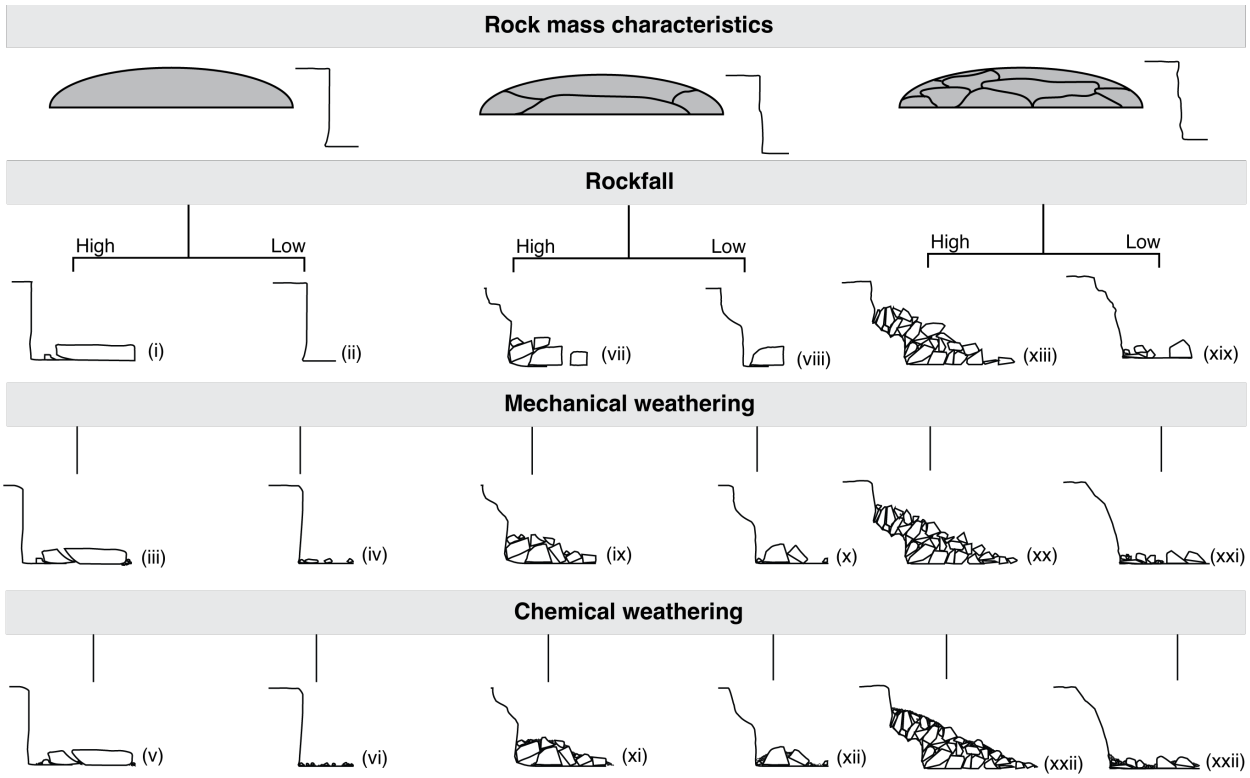

Figure 2.18. Conceptual model of the evolution of the free face of a fault scarp in jointed volcanic rock, with no additional scarp growth events or volcanic modification. Illustration shows scenarios based on rock mass characteristics (decreasing ratio of block height to scarp height from left to right), rockfall (high and low frequency), mechanical weathering and chemical weathering.

Table 2.1. Three measures of scarp age (date of initiation, date of last growth episode and growth rate) for each scarp age group.

	Initiation	**Last growth episode**	**Growth rate**
Group A Kau Desert Fault Kalanaokuaiki Pali East Kalanaokuaiki Pali West Ohale Fault	< 1.5 ka	< 10 yrs	> 5 mm/yr
Group B Sodulholagja Gildruholtsgja Stora-Aragja Nydri-Mosadalagja	< 13 ka	< 1 ka	1-5mm/yr
Group C Hilina Pali	Approx. 30 ka	< 100 yrs	> 10mm/yr
Group D Bishop Scarp 1 Bishop Scarp 2 Bishop Scarp 3	< 0.76 Ma	< 15 ka	0.2-1 mm/yr
Group E Gold Digger Pass Scarp Crumes Lake Scarp	2 Ma	10 ka	< 0.1 mm/yr

Table 2.2. Structural measurements of studied scarps.

	Max length (km)	**Average length per group (km)**	**Max height (m)**	**Average height per group (m)**	**Mean D/L**
Kau Desert Fault	5.3	5.2	21.8	17.3	$3.3*10^{-3}$
Kalanaokuaiki Pali East	5.4		22.0		
Kalanaokuaiki Pali West	5.0		17.4		
Ohale Fault	4.9		8.2		
Sodulholagja	6.5	4.8	15.3	18.0	$3.6*10^{-3}$
Gildruholtsgja	6.1		37.9		
Stora-Aragja	3.6		8.5		
Nydri-Mosadalagja	2.9		10.5		
Hilina Pali	13.8	13.8	475.3	475.3	$3.4*10^{-2}$
Bishop Scarp 1	1.8	2.2	27.7	32.3	$1.5*10^{-2}$
Bishop Scarp 2	2.6		18.6		
Bishop Scarp 3	2.3		50.6		
Gold Digger Pass Scarp	14.9	16.8	89.9	115.9	$6.8*10^{-3}$
Crumes Lake Scarp	18.6		141.9		

CHAPTER 3: A NEW METRIC FOR MORPHOLOGIC VARIABILITY USING LANDFORM SHAPE CLASSIFICATION VIA SUPERVISED MACHINE LEARNING[1]

3.1 INTRODUCTION

The core work of geomorphology is to identify, describe, classify, and interpret landforms. Advances in remote sensing and computational techniques have fueled efforts to develop workflows to characterize landforms quantitatively and automatically, with a view towards increasing the time-efficiency, reproducibility, and level of detail in geomorphic studies. These methodologies require translating qualitative, and often landform-type-specific, conceptual models into quantitative parameters that can adequately identify salient landform features.

Early workers built on manual quantitative procedures of describing landforms (Hammond, 1964, 1954), using slope and relief characteristics to automatically segment Digital Elevation Models (DEMs) into landform units (e.g., Dikau et al., 1991). Further efforts focused on refining and expanding these DEM-based automated mapping methods, using differential geometry (e.g., Giano et al., 2020; Irvin et al., 1997; MacMillan et al., 2004, 2000; Olaya, 2009), pixel pattern recognition, or geomorphons, (Gioia et al., 2020; Jasiewicz and Stepinski, 2013), and object-based image analysis (e.g., Drăguţ and Blaschke, 2006; Drăguţ and Eisank, 2011). Workflows are constructed around either manually defined classes based on empirical knowledge (e.g., Pennock et al., 1987; Skidmore, 1990), or a classification derived by machine learning algorithms (e.g., Brown et al., 1998; Hengl and Rossiter, 2003; Iwahashi and Pike, 2007). These methods focus on

[1] Chapter 3 is a published article: Brigham, C. A. P., & Crider, J. G. (2022). A new metric for morphologic variability using landform shape classification via supervised machine learning. *Geomorphology*, *399*, 108065. https://doi.org/10.1016/j.geomorph.2021.108065

a variety of scales, from delimiting physiographic provinces (e.g., Drăguţ and Eisank, 2012) to identifying individual landforms (e.g., Castillo et al., 2014; Korzeniowska et al., 2018; Walker et al., 2020). Automated methods of landform description and classification have significantly advanced our quantitative understanding of many features, but the variety of methodologies demonstrates that many of these approaches are setting- or landform-dependent. Indeed, they require a conceptual model defining rules and value thresholds, susceptible to over-fitting and not necessarily transferrable across landscapes (Castillo et al., 2014).

Furthermore, having identified, described, and classified a landform, the geomorphologist is faced with the additional challenge of interpretation: identifying and quantifying the type and rate of the structural and geomorphic processes that control the shape of the landform. A rich body of literature exists on the links between form, measurable site parameters, and process (e.g., reviews by de Boer, 1992; Stoddart, 2013). However, isolating the effects and rates of specific processes is a daunting task, given the complexity of natural systems, where many processes can be active concurrently at variable spatial and temporal scales and where different permutations of types and rates of processes could converge towards a similar landform morphology. Historically, two general strategies have been used: “natural laboratories” where landforms with similar initial morphologies are observed in settings where one or a few parameters are changed (e.g., climate, age of the landform, rock strength) (e.g., Clarke and Burbank, 2010; DiBiase et al., 2018; Duvall et al., 2004; Murphy et al., 2016); and “space-for-time substitution” where landforms of a single type are observed in similar conditions but at different stages of evolution (e.g., Hilley and Arrowsmith, 2008; Kirkbride and Matthews, 1997; Obanawa et al., 2009). Important insights have been gained by both approaches, but challenges and limitations remain in applying these methods,

given the careful site selection necessary to isolate the variable of interest and minimize unwanted complexities.

We propose a workflow that builds on the advances in the fields of morphometric landform characterization and process geomorphology, while addressing some of the limitations present in current methodologies. By associating a large number of shape measurements universal to all types of landforms (e.g., positional data along landform profiles) to measurements of parameters related to active processes (e.g., type and density of vegetation to account for biogenic weathering), it is possible to detect and describe how form and process vary together. If the variation in a given structural or geomorphic parameter accounts for a large percentage of the variation in landform shape, this parameter is likely to be an important control of morphologic change. Our goal is to determine which processes are the most active along the landform by ranking parameters by their degree of covariance with landform shape. This approach remedies some of the limitations of natural laboratories and space-for-time substitution: we can consider the contribution of many different parameters at a single site and we can account for differences in active processes to compare sites at different stages of evolution in different settings.

Successfully identifying active processes through covariance patterns hinges on our ability to use automated landform analysis techniques to quantitatively record variations in landform profile shape. A previous approach identified areas of morphologic change in longitudinal and transverse watershed profiles by profile classification along specific parameters related to watershed characteristics (Lin and Oguchi, 2006). Our method generalizes this approach, by forgoing the derivation of landform-specific metrics and instead using data-reduction techniques on the positional data of the profile itself as the basis for profile classification. This allows for a widespread application of this approach to many different types of landforms, as it eliminates the

need to find a sufficient number of landform-specific parameters to quantitatively characterize the shape of the profile. Geomorphologists can thus easily establish morphologic classes based on field observations and expert knowledge. In our approach, we first establish expert-defined morphologic classes, and automatically parameterize and classify landform profiles into these classes using a supervised machine learning algorithm. We then use the profile classification results to calculate a new metric: the morphologic variability of a landform, which measures the frequency and degree of change in landform profile shape. In this paper, we show how to determine this metric using a landform-specific case study (fault scarps in jointed bedrock) and suggest how it may be successfully applied to compare many types of complex landforms at fine and broad scales, considering both evolutionary stage and setting.

3.2 THEORETICAL BACKGROUND

Our workflow automatically quantifies the morphologic variability of a given landform using machine learning techniques. We start by manually assigning profiles taken at even intervals along the landform to morphologic classes. Our approach assumes that an expert has made careful observations of the landform in question and has developed a hypothesis about how the shape of the landform might relate to parameters such as process or age. With this framework in mind, the expert defines morphologic classes, labels a representative training dataset of landform profiles according to this classification (Figure 3.1a) and uses a supervised machine learning approach to objectively and automatically characterize the morphologies present in unclassified landforms. In order to do so, we need two main quantitative tools: the first, to isolate the features in the qualitatively classified or “training” dataset that will separate the labeled members of each class along meaningful class boundaries; and the second, to accurately predict the class of unlabeled profiles, based on their similarity to members of a certain class defined in the training dataset. We

posit that the first goal can be accomplished by Principal Component Analysis using Singular Value Decomposition (PCA/SVD) of the profile (two dimensional) positional data; and that the second goal can be met with a Support Vector Machines (SVM) learning algorithm.

Examining landform-shape variation requires identifying the most important morphologic patterns present in a given topographic dataset. To do so quantitatively and accurately, we need to determine the specific patterns or features along the profile that vary the most among the qualitatively defined classes. However, high-resolution topographic datasets are commonly composed of thousands to millions of points, so manually detecting these patterns in point-cloud-derived metrics is virtually impossible. Linear algebra offers a means to efficiently identify features that maximize variation from any data matrix: the singular value decomposition (SVD). SVD is the factorization of a matrix into its constitutive components, by diagonalizing the matrix into a tailored set of orthonormal bases (Golub and Reinsch, 1970; Golub and Van Loan, 1996). Principal component analysis (PCA) is the application of SVD to mean-subtracted data in order to find the "directions" with the greatest variance, called principal components. Our approach to feature extraction using PCA/SVD is modeled on the "eigenfaces" example, a notable application of these methods to the field of automated facial recognition. Eigenfaces are images that represent the principal components of a distribution of human faces (Sirovich and Kirby, 1987; Turk and Pentland, 1991), which can be used to extract the relevant facial information that contributes to the overall variation among face images, which may or may not be related to human intuition of face features. The eigenfaces define a new coordinate system, the eigenspace projection (Trucco and Verri, 1998), in which different images of the same people tend to cluster together (e.g., Asiedu et al., 2014; Hsu and Chen, 2007; Muller et al., 2004). In the case of landform analysis, the principal aim of SVD/PCA is to find landform features present in a dataset of 2D profile

coordinates that will define a space where landform profiles of similar morphologies will cluster together.

Let $\boldsymbol{A}$ be the data matrix of size $\boldsymbol{m} \times \boldsymbol{n}$, with $\boldsymbol{m}$ the number of observations taken along the profile and $\boldsymbol{n}$ the number of landform profiles. To condition the matrix for PCA, we center each row by calculating the mean landform profile coordinates and subtracting them from $\boldsymbol{A}$, yielding the mean-centered matrix $\boldsymbol{A'}$. The SVD of $\boldsymbol{A'}$ will be:

$$\boldsymbol{A' = U\Sigma V^T}$$

where $\boldsymbol{U}$ and $\boldsymbol{V^T}$ are $\boldsymbol{m} \times \boldsymbol{m}$ and $\boldsymbol{n} \times \boldsymbol{n}$ orthonormal matrices and $\boldsymbol{\Sigma}$ is an $\boldsymbol{m} \times \boldsymbol{n}$ diagonal matrix with singular values arranged along the diagonal in decreasing order (Figure 3.1b). The columns of $\boldsymbol{U}$ are called the left singular vectors of $\boldsymbol{A'}$ and form an orthonormal basis for the space spanned by the $\boldsymbol{n}$ columns of matrix $\boldsymbol{A'}$ The columns of $\boldsymbol{V}$ are called the right singular vectors of $\boldsymbol{A'}$ and form an orthonormal space spanned by the $\boldsymbol{m}$ rows of matrix $\boldsymbol{A'}$. Relating back to the original data matrix, the columns of $\boldsymbol{U}$ represent the principal components of $\boldsymbol{A}$. The singular values, $\boldsymbol{\Sigma}$, are proportional to the variance captured in each principal component. The matrix $\boldsymbol{\Sigma V^T}$ contains the principal component scores, which are the coordinates of the landform profiles in a $\boldsymbol{r}$-dimensional principal component space. We can reduce the dimensionality of the analysis (thus reducing the noise) by selecting a subset of $\boldsymbol{l}$ of modes that represent most of the variability in the dataset, as indicated by higher $\boldsymbol{\Sigma}$ values.

The utility of SVD in landform classification is that we can treat a set of profiles of known morphology as vectors in a subspace defined by $\boldsymbol{l}$ principal components: the projections of $\boldsymbol{\Sigma V^T}$ into the subspace should create clusters, or characteristic domains, for each morphologic type (Figure 3.1c). The classification of unknown profiles is then performed by projecting a new profile into the subspace, and classifying the profile by comparing its coordinates in the subspace to the coordinates of known profiles.

In order to perform this classification automatically, we employ the support vector machine (SVM) method (Boser et al., 1992) The SVM is a machine learning algorithm that uses data vectors with expert-assigned class labels (support vectors) to define the optimal hyperplane in the subspace that maximizes the separation between vectors of different classes (Figure 3.2). The group of labeled data vectors is known as the training set; it contains the feature patterns upon which the classification is based. SVM is thus a supervised learning algorithm, as opposed to an unsupervised learning algorithm, where no *a priori* knowledge is used to aid the classification. Once the hyperplane is defined, unlabeled data can be classified based on their features by the trained SVM. Though SVM is fundamentally a binary classifier, we can use it to solve multi-class problems. A popular approach to classifying some number of classes, K, is to train K(K-1)/2 two-class SVMs on datapoints from all possible pairs of classes, and then to classify test points according to which class has the highest number of 'votes'. We used this approach, also called one-against-one (Bishop, 2006; Hastie and Tibshirani, 1998; Knerr et al., 1990) in our study.

3.3 CASE STUDY: JOINTED BEDROCK FAULT SCARPS

To demonstrate how to apply this statistical approach to a specific type of landform, we use the example of fault scarps in jointed bedrock. Fault scarps are tectonic landforms resulting from the dislocation of the ground surface by movement along a fault plane (e.g., Stewart and Hancock, 1990, and references therein). Study of their characteristics can yield information about the style and timing of near-surface deformation, particularly in the case of scarps in unconsolidated materials, where changes in scarp profiles can be modeled by hillslope diffusion (e.g., Andrews and Hanks, 1985; Bucknam and Anderson, 1979; Hanks et al., 1984; Hanks and Andrews, 1989; Nash, 1980; Roering et al., 1999). However, we cannot apply diffusion models of scarp degradation in to scarps in jointed bedrock: the presence of joints complicates both the original

scarp form, making it difficult to definitively recognize modification by erosion, and the manner in which scarps erode, with more stochastic processes that are not accounted for in continuum models. Given the frequent coupling of tectonic activity and magmatism, scarps within jointed bedrock are very common throughout the world, particularly in areas of active extension, such as Iceland (e.g., Villemin et al., 1994), the East African Rift (e.g., Strecker et al., 1990), and the northwestern Basin and Range (e.g., Pezzopane and Weldon, 1993). Degradation and weathering in jointed bedrock has been explored in the specific contexts of waterfalls (e.g., Lamb and Dietrich, 2009) and glacial headwalls (e.g., MacGregor et al., 2009), but are still poorly constrained for fault scarps.

Our statistical approach to determining morphologic variability is well suited to reducing the complexity of this system: by comparing the morphologic variability of the fault scarp to those of measured tectonic and geomorphic parameters, we can untangle original structure from subsequent modification and make interpretations about the different types of processes active along the scarp. First, we make detailed field observations from four scarp localities, define morphologic classes, and collect high-resolution topographic data. Then, we extract fault-scarp-line-normal profiles, normalize the profile positional data, and apply PCA/SVM to the dataset.

3.3.1 Field study of fault scarps in jointed rock to establish morphologic classes

We conducted fieldwork in three regions with normal fault scarps in jointed bedrock: two areas of the subaerial rift zone of southwestern Iceland, the Volcanic Tablelands of central California, and the flank of Medicine Lake Volcano in northern California (Figure 3.3). At each field site, we made detailed observations of the form of the scarps and parameters related to the processes that might control it (e.g., type of tectonic structures present, type and amount of vegetation, fracture spacing along the free face, size, and distribution of the talus). Our field

observations indicated that the shape of each fault scarp was variable, with certain recurring forms. Using our field observations of forms and structures and our expert knowledge, we defined morphologic classes based on two principles that emerged from field observations: 1) the proportion of exposed free face (the exposed surface resulting from faulting or gravity spalling) varies significantly along strike of a scarp; 2) initial scarp conditions resulting from faulting and volcanic processes can yield profile forms that are gravitationally unstable through time, such as an overhang or a steep convex-up monocline, and these unstable forms have more stable counterparts, where the instability is reduced by erosional processes. By combining these two principles, we obtain the following six morphologic classes (Figure 3.4): 1) all free face with overhang, 2) all free face with no overhang, 3) partial free face with convex-up lower slope, 4) partial free face with concave-up lower slope, 5) no free face with convex-up lower slope, 6) no free face with concave-up lower slope.

3.3.2 Data acquisition and processing

We used structure-from-motion (SfM) photogrammetry along selected fault segments to create surface models. Depending on the complexity of the scarp features, between 400 and 900 images were captured using a drone equipped with a 12-megapixel camera with a f/2.8 lens and a 94° field of view. Photographs were taken at varying lateral positions, elevations and facing directions of the area surrounding the portion of the fault scarp of interest, allowing for >80% overlap between photographs. To increase the geometric accuracy of the model, we established five temporary ground control points (GCPs) at each site of interest using neon-orange cloth squares, positioned on both the hanging wall and the footwall of the fault. The GCPs were surveyed with a Trimble Geo7x GPS (1-100 cm GNSS accuracy).

For each scarp, we first manually defined the fault scarp line along the crest of the scarp. From the point cloud, we extract 2D topographic profiles perpendicular to the manually defined fault scarp-line at a set interval of 2 m along the strike of the scarp. We use 125 profiles from five scarps to use as a training dataset, and manually assigned each profile to one of the six morphologic classes.

To ensure that features of the same type are correctly compared, we consider only the scarp face. We crop each profile between two anchor features: the crest and toe of the scarp, the highest and lowest points on the fault scarp, between which are the free face and the talus slope accumulated below the free face. To compare the shape of fault scarps of different scales, we normalize vertical and horizontal values of scarp position by scarp height, defined to be the difference in elevation between the toe and crest (Figure 3.5a). We developed an algorithm to automatically determine the position of the crest and toe of the scarp and calculate scarp height for each profile. For the algorithm to automatically select the toe and the crest, we established the following selection principles (Figure 3.6):

1. At the crest and toe of the scarp, the curvature values of the scarp profile will be local extrema (minima for the scarp crest and maxima for the scarp toe). In the blocky terrain produced by degradation of jointed-bedrock scarps, this is not an exclusive condition and further filtering is required to correctly select the crest and toe.
2. The crest will be a point that minimizes the angle created by itself and the m nearest points on either side of it, while maximizing elevation. In our algorithm, we use $m = 5$ (angle a on Figure 3.6).
3. Given that all profiles are cropped so that the first point in the profile (start point) and the last point (end point) are, respectively, on the foot wall and hanging wall of the fault, the

toe will be a point that minimizes the angle between the crest, itself and the start point (angle *b* on Figure 3.6), while minimizing elevation.

To implement the curvature rule, each topographic profile is fitted with a spline function composed of a sum of B-splines, using the Python package NURBS-Python (Bingol and Krishnamurthy, 2019). The first and second partial derivatives (of x and y with respect to the parameter u) are evaluated at even intervals along the curve. We calculate the curvature

κ of the spline functions, using the formula of signed curvature for a parametrized curve:

$$\kappa = \frac{x'y'' - y'x''}{(x'^2 + y'^2)^{\frac{3}{2}}}$$

For all points corresponding to local minima in curvature values, we calculate the angle between the selected points and the fifth point before and after it. The crest of the scarp is selected as the point with the lowest value for the sum of this angle and the complement of the elevation, thus minimizing the angle while maximizing the elevation.

For each of the points corresponding to the local maxima, we calculate the angle defined by the start point, the previously determined crest of the scarp, and the minima point. The toe is selected as the point with the lowest value for the sum of this angle and the elevation. We then difference the elevation of the toe from the elevation of the crest to obtain the scarp height. To obtain the normalized profiles, we divide the elevation and the distance along the profile by the scarp height (Figure 3.5a) and crop the profile to the points situated between the crest and the toe (Figure 3.5b).

Once we have normalized the profiles and cropped them to the scarp face, we take evenly-spaced position coordinates in the vertical (y) and horizontal (x) directions, along the spline function defined in 3*c*. We store these measurements in a data matrix A, from which we subtract the mean profile values to obtain A'. We perform SVD analysis on matrix A', yielding U and V

and the diagonal matrix Σ. Since Σ represents the singular values of A', we use it to determine the singular value spectrum of the data and the rank, or the number of modes of importance, of the data.

3.3.3 Calculating the morphologic variability metric using the classification results

Based on our field observations, we expect many of the scarps to contain forms from several of the morphologic classes, if not all six. The classes are unevenly distributed along the scarp and are present in differing proportions between different scarps. We introduce a novel *morphologic variability metric* to summarize these along-strike changes, allowing us to both correlate patterns in variability to other available datasets along the scarp and to make comparisons between scarps in different locations.

We define a successful variability metric as: 1) imparting information as to the number of classes present in the scarp or section of scarp; 2) accounting for the proportions of the present classes; 3) reporting changes in morphology at a high enough resolution to capture the effects of most geomorphic processes. In this framework, the highest variability value represents a landform section that presented all classes in equal proportions; the lowest variability value would be assigned to a scarp section with a single morphologic class.

To quantify variability, we first calculated the proportion of each class (ranging from 0 to 1) within a given window along the scarp. In order to account for the distribution of proportions in a given section, we calculated the standard deviation (σ_{prop}) from the mean (μ_{prop}) of these proportions. Given that the values of σ_{prop} are non-unique for each class, we add a constant, equal to the ratio of the number of classes present in the section to the total number of classes. We obtain the following equation for our variability metric, v_s, with p_{class} the proportion of each

class, $N_{total\ classes}$ the total number of classes, and $N_{classes}$ the number of classes present in a given section:

$$v_s = \sqrt{\frac{\sum\left(p_{class} - \mu_{prop}\right)^2}{N_{total\ classes}}} + \frac{N_{classes}}{N_{total\ classes}}$$

For our case study, we determine the range of values that v_s could take, with a minimum value v_{min} occurring when $N_{classes} = 1$ and $\sigma_{prop} = \sigma_{max}$, and a maximum value v_{max} occurring when $N_{classes} = 6$ and $\sigma_{prop} = 0$. To obtain a variability scale between the values of 0 and 1 that increases with increasing variability, we normalize v_s using v_{max} and v_{min}, obtaining $v_{s\ norm}$:

$$v_{s\ norm} = \frac{\left(\sigma_{max} - \sigma_{prop} + \frac{N_{classes}}{N_{totalclasses}}\right) - v_{min}}{v_{max} - v_{min}}$$

We calculated $v_{s\ norm}$ in a moving window centered on the location of each section profile (spaced every 2 meters for our case study) (Figure 3.7). In order to choose an appropriate window length L_{window}, we determined that the number of profiles represented in the window must be proportional to the total number of classes, so that the maximum value of $v_{s\ norm} = 1$ could theoretically be obtained with all classes equally represented. We determined that a window size of $2N_{TotalClasses} = 12$ profiles ($L_{window} = 24$ meters) captures representative morphologic variation at the scale of many scarp-altering geomorphic processes.

Given six classes and a window size of 12 profiles, we determined all 37 possible unique combinations of proportions with a sum equal to 1 and calculated $v_{s\ norm}$ for each scenario. The possible values are separated into distinct ranges characterized by the number of classes present in

the window and increase within those ranges as the difference between the highest and lowest proportions decrease. The morphologic variability $v_{s\ norm}$ is thus a useful summary metric that provides information on both the number of classes present and the distribution of the class proportions in a section.

3.4 RESULTS

3.4.1 Optimizing the dimensionality of the principal component space

The singular value spectrum of the training dataset indicates that 4 modes (representing principal components) account for significant shares of the variation in scarp profile form. Figure 3.1c shows the projection of the dataset into a space defined by the first three principal components and colorized according to class label. The first mode represents 46.8% of the total variance, the second 8.0%, the third 7.0% and fourth 4.3%.

Since the first four modes explain only 66.1% of the variance in data, we evaluate whether additional modes are required to build our classifier. The choice of the number of modes $\boldsymbol{l}$ to represent the dataset affects the classification model accuracy. If too few modes are chosen, the model might omit significant features that change the coordinates of our data points in principal component space, thus affecting the orientation of the SVM hyperplane and changing class assignation. If too many modes are selected, the model might consider feature anomalies that are unique to the training data, resulting in overfitting. We optimized the value of $\boldsymbol{l}$ by running the classification model for values of $\boldsymbol{l}$ ranging from 1 to 125. For each value, we performed 10-fold cross validation (see section below) and determined the mean model accuracy. The highest model accuracy was 84.5%, obtained with the value $\boldsymbol{l} = 5$, which we used for the subsequent analysis.

To visualize the five principal components used for classification, we added the values in the first five columns of the $\boldsymbol{U}$ matrix to the mean scarp profile and plotted the resulting principal

component profile (or PC profile) along with the mean scarp profile (Figure 3.8b). By observing the deviations of the PC profile from the mean profile (Figure 3.8a and c), we can determine the geomorphic characteristics each principal component uses to separate profiles into groups. For example, the principal component that explains close to 50% of the total variance in the dataset (PC1) distinguishes between scarps that exhibit a decrease in slope in the lower two-thirds of the profiles and those that do not, whereas PC2 and PC3 focus on the concavity and convexity, respectively, of the scarp profiles (Figure 3.8d).

3.4.2 Evaluating model performance

To assess the performance of the classification algorithm, we use 5-fold cross-validation (Stone, 1974). By withholding a random 20% (one fifth) of the data as the test dataset and using the remaining 80% as the training dataset, we predict the class of the scarps in the test dataset. We repeat this approach with a different random 20%, and so on until each profile has been assigned to the test dataset and its class predicted.

We used five metrics to evaluate each fold: accuracy, precision, recall, f1-score, and Matthews Correlation Coefficient (Raschka, 2018). The accuracy of the classifier represents the proportion of correctly classified profiles to the total number of profiles. With L being a given class label, precision is the proportion of correctly predicted L members to all predicted L members. Recall is the proportion of correctly predicted L members to the actual number of L members. The F1-score for L is the harmonic mean of these precision and recall scores. The Matthews Correlation Coefficient (MCC) is a summary statistic of the quality of a classifier by considering true and false positives and negatives (Matthews, 1975). Its values range from -1 to +1, with +1 representing a perfect prediction; 0, no-better-than-random prediction; and -1, total

disagreement between prediction and observation. The results of the model evaluation are summarized in Table 1.

Averaging the model evaluation results from the 5-fold cross-validation, we obtained an overall classifier accuracy of 81.4%, with a high MCC of +0.78. The accuracy results of our classification model are consistent with previous studies using SVMs: Beechie and Imaki (2014) classified channel patterns with a prediction accuracy of 82% with the training dataset; Othman and Gloaguen (2014) used SVM to conduct automated lithologic mapping with an accuracy of 79.3%; Marjanović et al. (2011) obtained an accuracy of 71% when mapping landslide susceptibility.

To investigate how the classifier performed for each class, we used the F1-scores to assess model performance (Table 1). Classes 1, 2 and 6 yielded the highest F1-scores (0.79, 0.98, and 0.96, respectively), whereas classes 3, 4 and 5 had lower scores (0.63, 0.77 and 0.65, respectively). By looking at the precision and recall values of these three classes, we can determine whether the classifier is missing elements of a given class (higher number of false negatives and lower recall score) or classifying too many elements as a given class (higher number of false positives and lower precision score). For example, in the case of class 3, the classifier has a precision score of 0.74 and a recall score of 0.63, suggesting that the model consistently misclassifies a proportion of class 3 profiles as those of another class.

3.4.3 Applying scarp form classifier to unlabeled scarps and comparing morphologic variability between 6 different scarps

Using all 125 classified scarps as training data, we applied the classification algorithm to Gildruholtsgja, a fault scarp in the Thingvellir region of Iceland. Profiles were extracted at a 2m interval along a 720m section of the scarp, then pre-processed according to the methodology

described in section 3.2. Once we obtained the Gildruholtsgja height-normalized and cropped profiles, we added their positional data to a matrix including the labeled training and performed PCA/SVD on this data matrix. Having obtained the projection values of the data into principal component space, we used SVM classification to assign class labels for the Gildruholtsgja scarp using the model parameters determined in section 4.2. A 3-dimensional visualization of the classification results (Figure 3.9a) shows how scarp form varies along its length. Although most of the scarp shows class 4 profiles, all six classes are represented. The figure shows that the scarp's variability in form is highest at the tips and center of the scarp, which is concordant with the calculated morphologic variability (Figure 3.10). Before obtaining these automatic results, we manually classified the 360 profiles of Gildruholtsgja (Figure 3.9b) to compare these expert-knowledge-derived results to that of our classification algorithm. We obtained a classification accuracy of 80% in this independent test of classification accuracy.

We calculated the along-strike $v_{s\ norm}$ for six sample scarps: Gildruholtsgjà, Nydri-Mosadalagjà, Stora-Aragja,VTBL-A, LVBD-A1 and LVBD-A4 (Figure 3.11). By calculating the mean $v_{s\ norm}$ for each scarp, we represent the average variability score $v_{ScarpMean}$ of each scarp on the variability reference graph, to simplify comparisons between sites. We observe that Nydri-Mosadalagjà has the highest variability score, averaging 5 classes per section length of 12 m and with an average difference in proportions of 30%. LVBD-A4 has the lowest variability score, averaging 3 classes per section and an average difference in proportions of 20%. The length of the scarps appears to be somewhat correlated with morphologic variability: shorter scarps exhibit higher morphologic variability.

3.5 DISCUSSION

The results of the study demonstrate that the along-strike morphologic variability of jointed bedrock fault scarps can be quantified in a semi-automatic procedure. The implications for future work are two-fold: 1) for a single scarp, regularly spaced variability measurements can be quantitatively compared to a wide variety of physical attributes that also vary along strike of the scarp (e.g. fracture spacing, vegetation, aspect, fault zone structure); 2) the average variability scores of scarps in different locations can be compared to metrics that vary from site to site (e.g. climate, tectonic setting, lithology). The first scenario offers the opportunity to explore the specific drivers of along-strike changes in scarp morphology, at a high enough resolution to correlate variability patterns to specific geomorphic processes. The second approach broadens the scope to extract larger-scale patterns from average variability scores for a large number of scarps in a variety of settings.

3.5.1 Advantages of pairing expert knowledge with machine learning to quantify landoform morphology

Beyond the specific case study of bedrock fault scarps, we show how to quantify the internal morphologic variability along any landform in an objective and time-efficient manner, using knowledge provided by fieldwork. Our approach involves: 1) an initial qualitative classification of landform profile shapes defined using expert knowledge and driven by a specific research question; 2) a statistical analysis of this manually-classified dataset to quantitatively characterize the distinction between the classes; 3) a supervised learning algorithm to assign labels to unclassified profiles; and 4) a morphologic variability metric that summarizes the results of the classification and enables comparisons between different landforms. This methodology has the

advantage of leveraging both the expertise of the researcher and the objectivity and reproducibility of a machine learning algorithm.

This approach outlined for the first two steps is consistent with previous studies that sought to make qualitative classifications of landform shape and quantify the morphologic variability in some manner. For example, O'Grady et al. (2000) qualitatively classified the slope profiles of passive continental margins from various locations and confirmed this classification quantitatively using factor analysis. Following a similar logic, we visually inspected the scarp profiles and qualitatively divvied them into six classes based on the amount of free face present and the convexity of the slope, a classification that does not encompass every single type of scarp profile morphology, but that we believed adequately described the continuum of scarp profile shapes. Our quantitative check on these qualitative classes derives from the SVD of the profile data and its projection into principal component space (Figure 3.1c). When we project our training data into a space defined by the first three principal components, we observe that the six classes are more or less distinct, with members of classes 1, 2 and 6 forming the most distinct clusters, but those of classes 3 and 4 displaying significant overlap. This level of distinctness of the classes directly translates to the accuracy of the classification model for each class: the mean F1-score of classes 1, 2 and 6 is 0.91, compared to 0.68 for that of classes 3, 4 and 5. This discrepancy suggests any loss of accuracy is not due to significant error inherent in the classification model, but rather a need to either modify the initial qualitative classification or to find a different training dataset that will maximize the separation of the classes in principal component space. This methodology thus offers an opportunity to assess the qualitative classification using quantitative means and iterate on the initial classification. For our case study, we discovered through this approach that the variability in profile shape shown by scarps with a partial free face (classes 3 and 4) obscured the

separation between profiles with concave lower slopes and those with convex ones. Given this information, we can either decide that the two classes are similar enough to be merged, or that the initial classification of these types of profiles is in fact overly broad and needs to be broken down into more than two classes. Although the first option increases the overall accuracy of the classifier to 93.0%, it does not serve our research question well, since we have posited that the degree of curvature of the slope is related to the process that formed it. We will thus need to refine the initial classification using our knowledge of fault scarp morphology. By cycling between the qualitative analysis tailored to a specific research question and the quantitative analysis offered by the SVD, this approach is conducive to better understanding and refining a classification.

Beyond quantitatively validating a qualitative classification, decomposing the profile positional data with SVD offers an opportunity to interpret the reconstructed principal components and identify the features that are most important to distinguish between profiles of different morphologic classes, which the expert might not have considered in their initial classification. In our case study, we use a framework of known hillslope morphologies to interpret the features present in the reconstructed principal components that form the basis of the scarp profile classification. This step provides an opportunity to check that these features are in fact consistent with the initial qualitative classification.

3.5.2 Quantifying the relationships between morphologic variability and measurable geomorphic features

By making pairwise comparisons, we can test the correlation between morphologic variability and another dataset taken along the scarp. The range of possible data types that could be compared are numerous. Here, we present a first-order example of a geomorphic feature easily obtainable from the SfM-derived topographic data: scarp height. Scarp height is used as a proxy

for throw along a fault (e.g., Crider and Pollard, 1998; Dawers and Anders, 1995); a strong correlation with morphologic variability would thus suggest that initial fault structure plays an important role in later scarp morphology. Scarp height was calculated using the method described in section 3.*4*.

Using the Pearson product-moment correlation coefficient, a measure of the strength of a linear association between variables, we test the strength of the relationship between the quantitative classification results along Gildruholtsgjà and scarp height (Figure 3.12). The comparison shows that scarp height has a moderate negative correlation with morphologic variability ($r = -0.31$), predicting approximately 10% of the variance in morphologic variability ($r^2 = 0.096$). With 90% of the variance left unexplained by the relationship between scarp height and morphologic variability, it is necessary to incorporate more data types into the analyses in order untangle the main drivers of scarp form variability; this is a topic of ongoing work. Our example demonstrates our approach in using the variability metric to test hypotheses about the geomorphic drivers of internal landform shape change.

Once the drivers of internal landform variability are explored and understood, we can use the mean morphologic variability of a landform to compare it to landforms from other settings, to determine the morphologic effect of broader site-dependent parameters, such as climate or lithology. As an example, we compare the average morphologic variability of our six study scarps to the maximum throw along each of these scarps (Figure 3.13). By making this comparison, we are seeking to determine the relationship between the total amount of slip accumulated along a fault and the morphology of its scarp. The comparison reveals that maximum scarp height has a strong negative correlation ($r = -0.79$) with the mean morphologic variability values of the six scarps, predicting approximately 62% of the latter's variance. This finding provides a quantitative

confirmation of the observation that the morphologic variability of a fault scarp appears to diminish for scarps that have accumulated more slip.

We suggest that the approach of using morphologic variability as a benchmark for comparison with other parameters to determine geomorphic drivers is applicable to landforms beyond that of fault scarps, such as understanding variability in coastal erosion rates (e.g., Pender and Karunarathna, 2013; Rodriguez et al., 2004) by using cross-shore profiles as a basis for comparison; or characterizing the spatial variability of channel morphology (e.g., Moody and Troutman, 2002; Yingkui et al., 2001) by classifying and quantifying the variability of cross-channel profiles.

3.6 CONCLUSION

We present a method to automatically classify point-cloud-derived topographic profiles of a landform into morphologic groups using a supervised learning algorithm. The results of this classification are then used to calculate the morphologic variability of the landform, a metric that quantifies the proportion and distribution of classes in sections along the landform. Having quantified the internal morphological variations along the landform, we can compare other datasets to the morphologic variability and determine the degree to which they co-vary. Parameters correlating strongly with morphologic variability can be understood as important actors on the morphology of the landform. We illustrate how geomorphic parameters can determine the proportion of variation explained by the drivers of landform morphology using this methodology. The average morphologic variability is used as a snapshot of the overall morphologic variation in the landform. We demonstrate how average variability can be compared to that of landforms in different settings to determine the contribution of factors that vary between sites. We suggest that the morphologic variability approach can meaningfully address outstanding questions in

geomorphology, generally, and in the realm of fault scarps, specifically. This approach is well suited to the complexities of process and form inherent in the problem of scarp evolution in jointed bedrock.

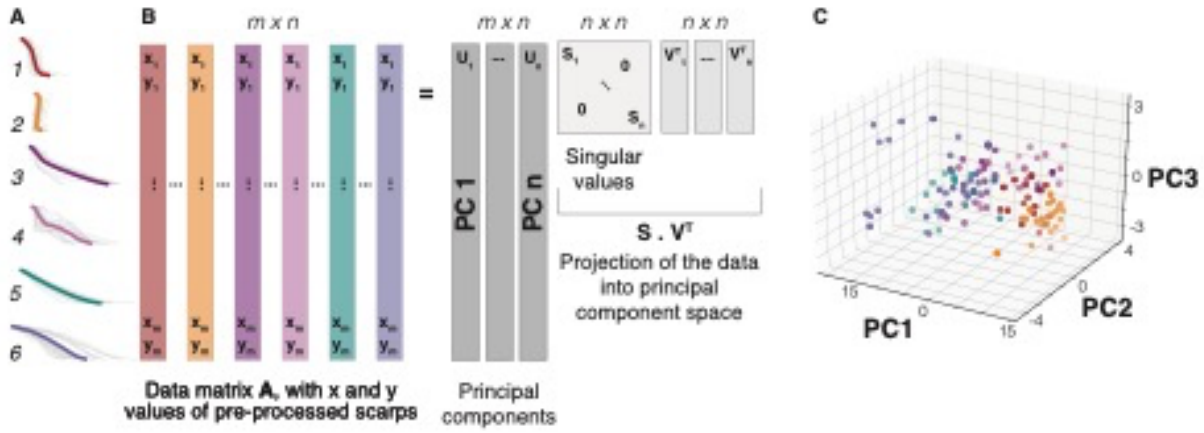

Figure 3.1. A) Manually classified training data profiles for each class, with average class profile color-coded by class. B) Schematic illustrating the Singular Value Decomposition (SVD) of the training data matrix (color-coded by class). C) Projection of training data (color-coded by class) into a subspace defined by the first three principal components.

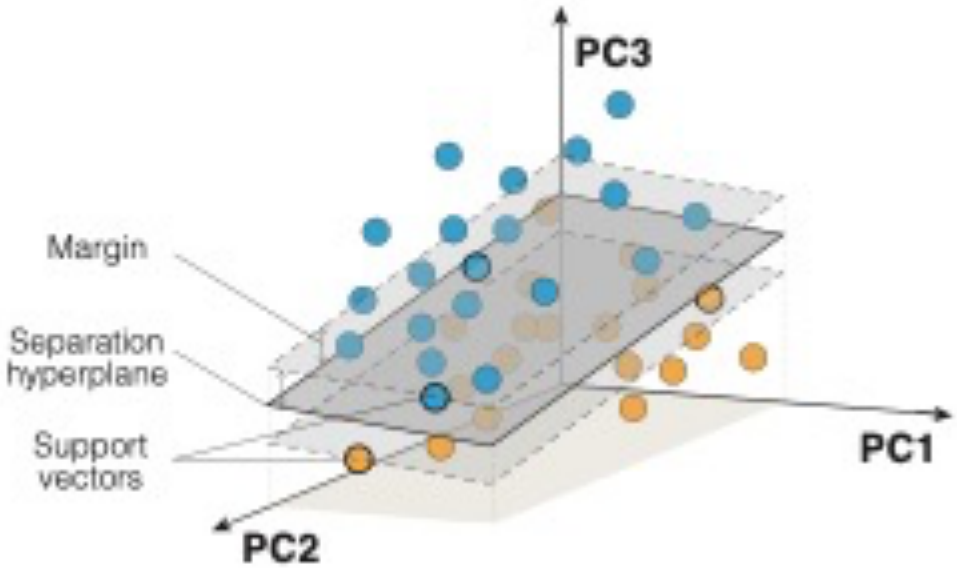

Figure 3.2. Schematic of the method by which a Support Vector Machine (SVM) determines the boundary between two classes.

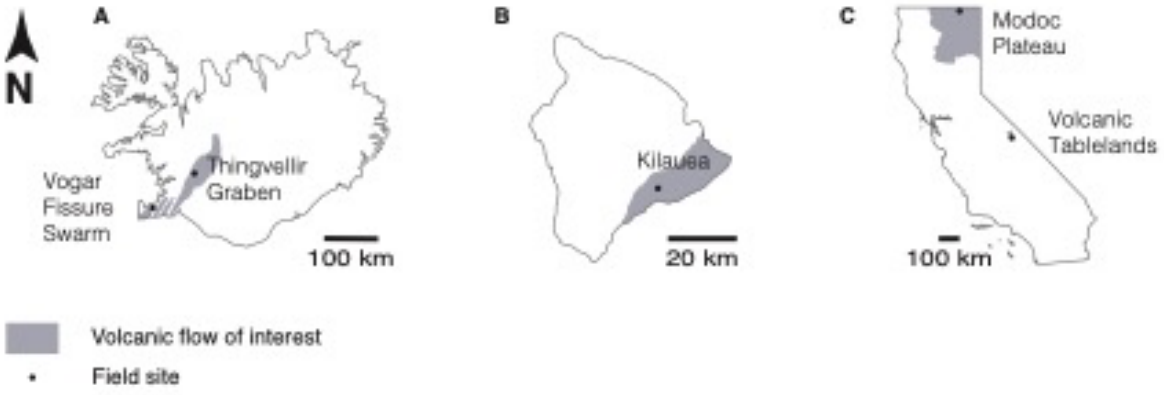

Figure 3.3. Field site locations in: A. Iceland; B. Hawai'i, USA; C. California, USA. For detailed field maps, refer to supplementary information.

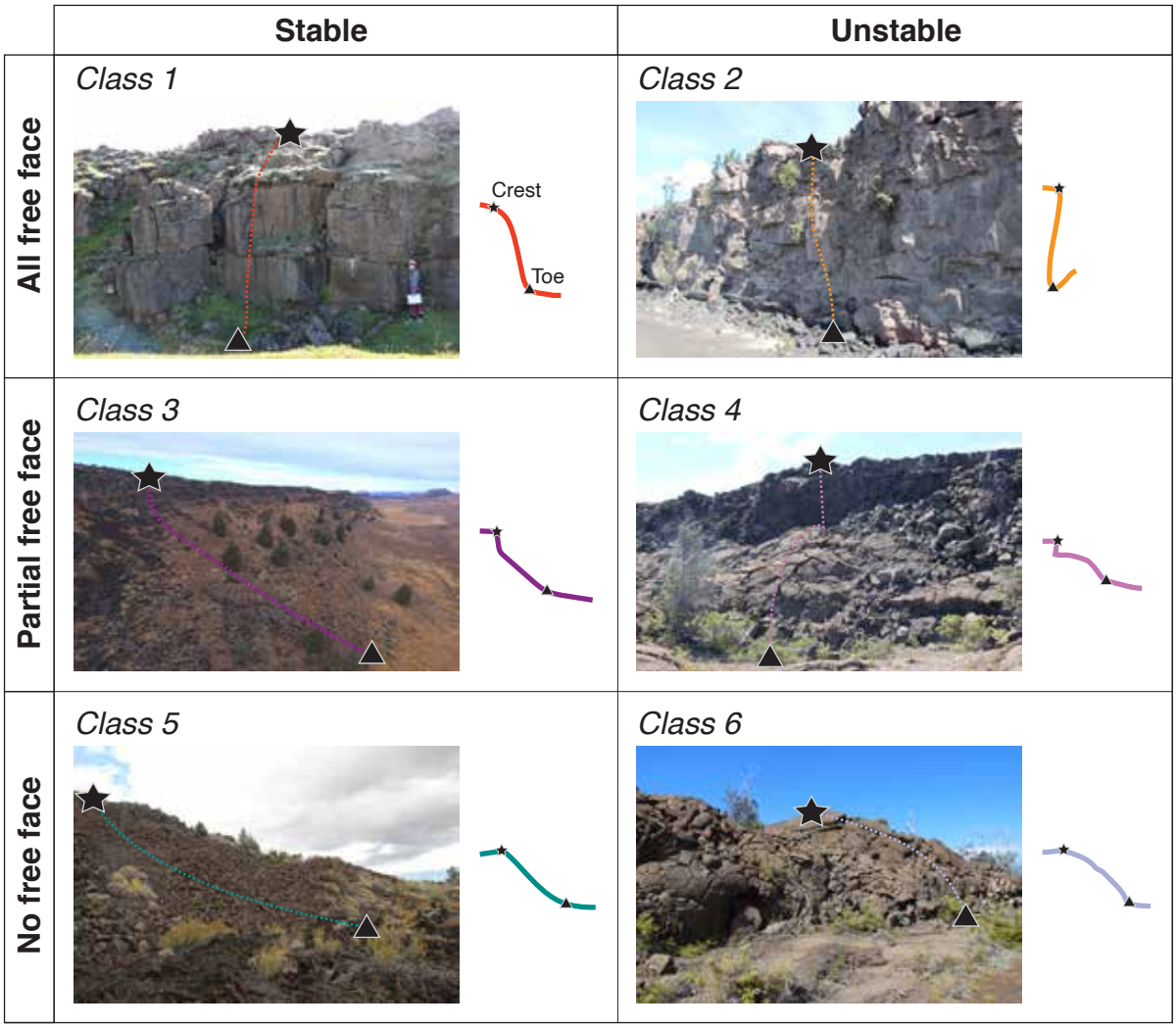

Figure 3.4. Morphologic classification of the studied fault scarps, with photograph example on the left and conceptual profile form on the right.

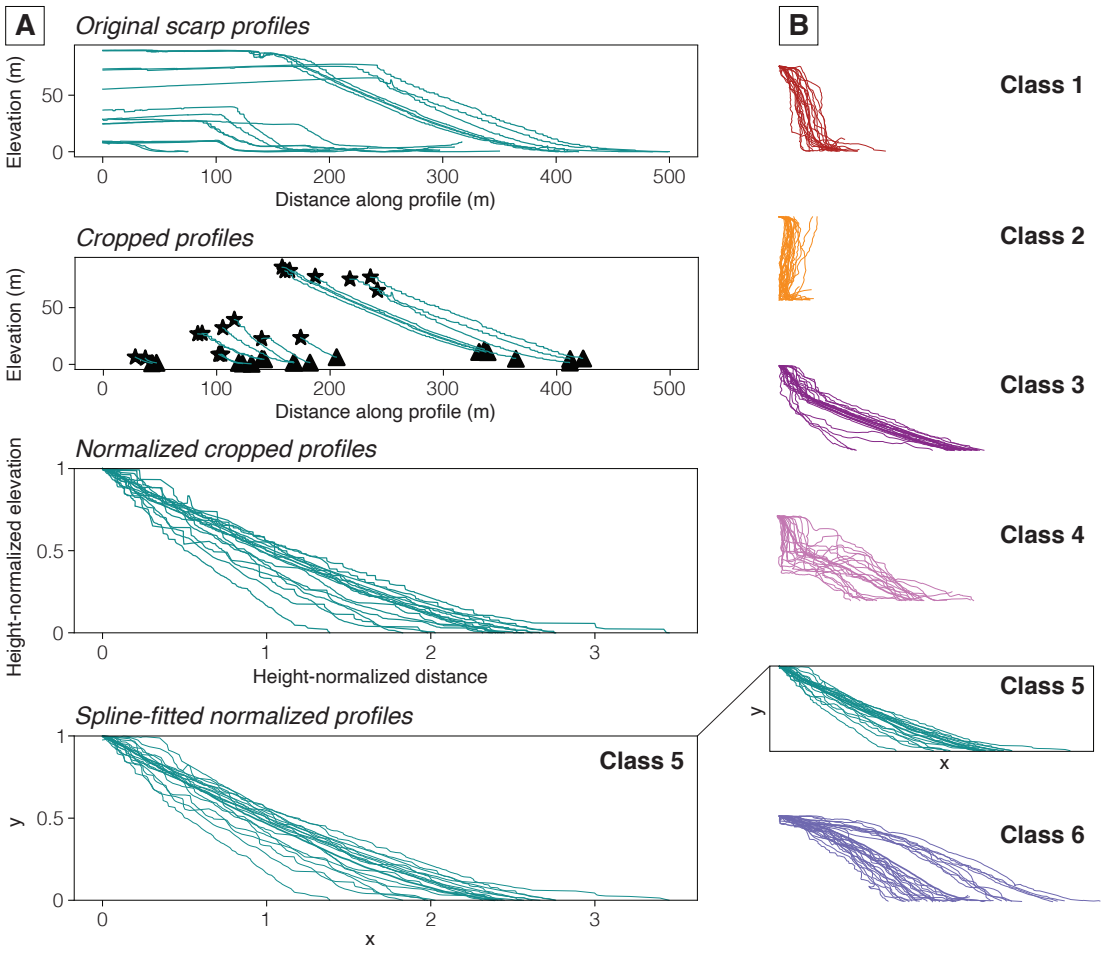

Figure 3.5. A) Pre-processing steps taken on the class 5 fault scarp profiles before classification: cropping the profile between the crest (star) and the toe (triangle) of the scarp, normalizing the cropped profiles by their maximum height and fitting B-splines to each of the profiles, with average class profile in bold. B) Final cropped, normalized and spline-fitted scarp profiles for each of the expert-determined classes, with average class profile in bold

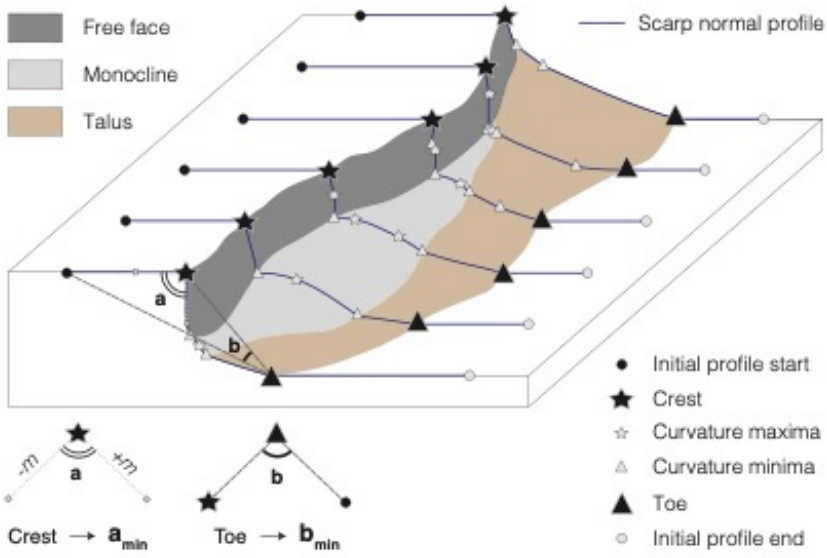

Figure 3.6. Schematic illustrating method to automatically determine the position of the crest and toe in scarp normal topographic profiles. For example, of the curvature maxima, the crest is the point that forms the smallest angle amin between the m points preceding and proceeding the maximum.

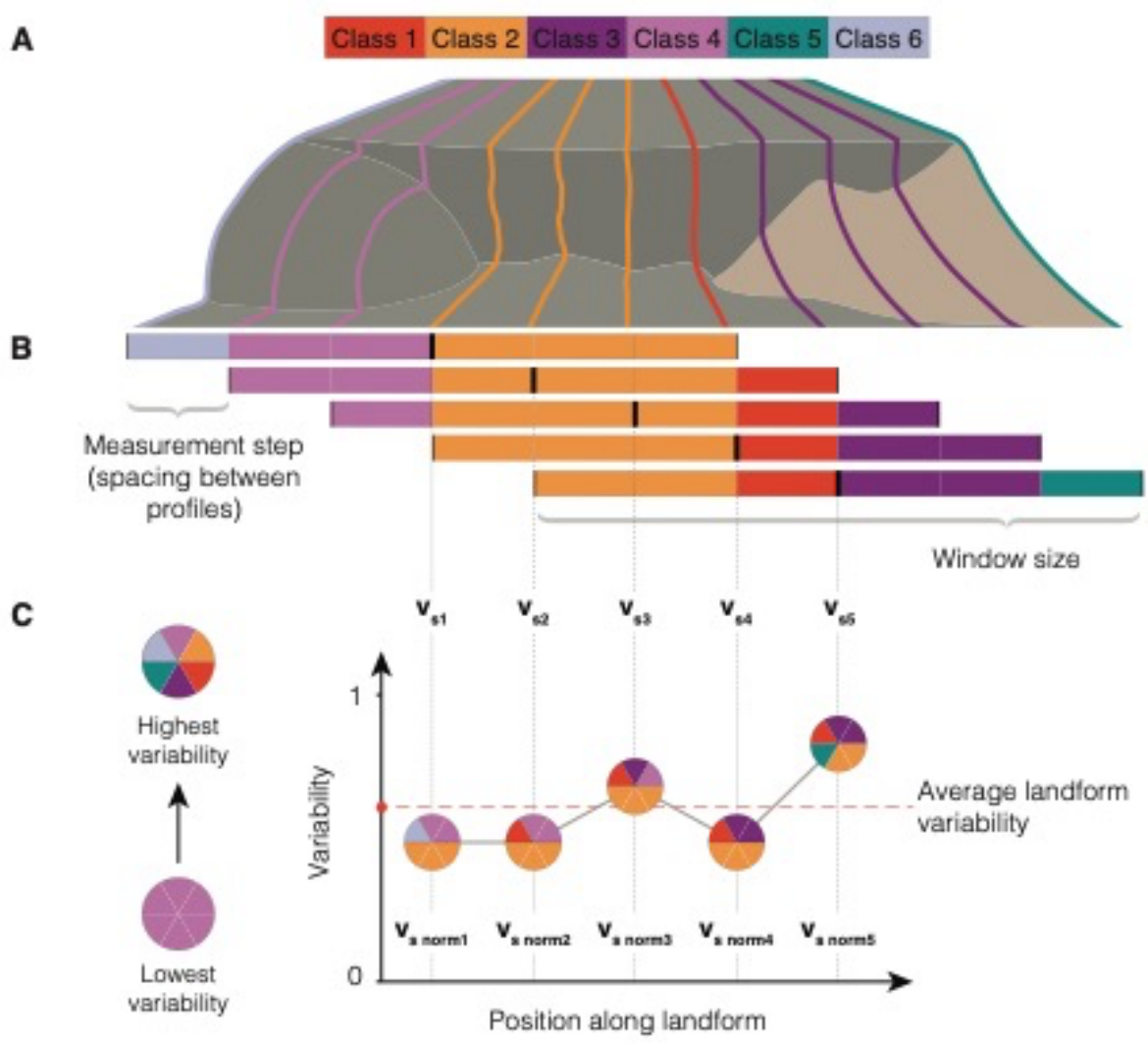

Figure 3.7. Conceptual model illustrating landform morphologic variability calculations. A) Cartoon of scarp and SVM-classified landform profiles. B) The number of classes and the proportions in which they are present are recorded in windows centered on a profile and moving at an increment equal to the spacing of the profiles and used to calculate the morphologic variabilities vs1, vs2, vs3, vs4, vs5 at five positions along the scarp. C) These values are normalized so that the highest variability is equal to one (six classes represented in equal proportions in the given window) and the lowest is equal to 0 (all one class in the window).

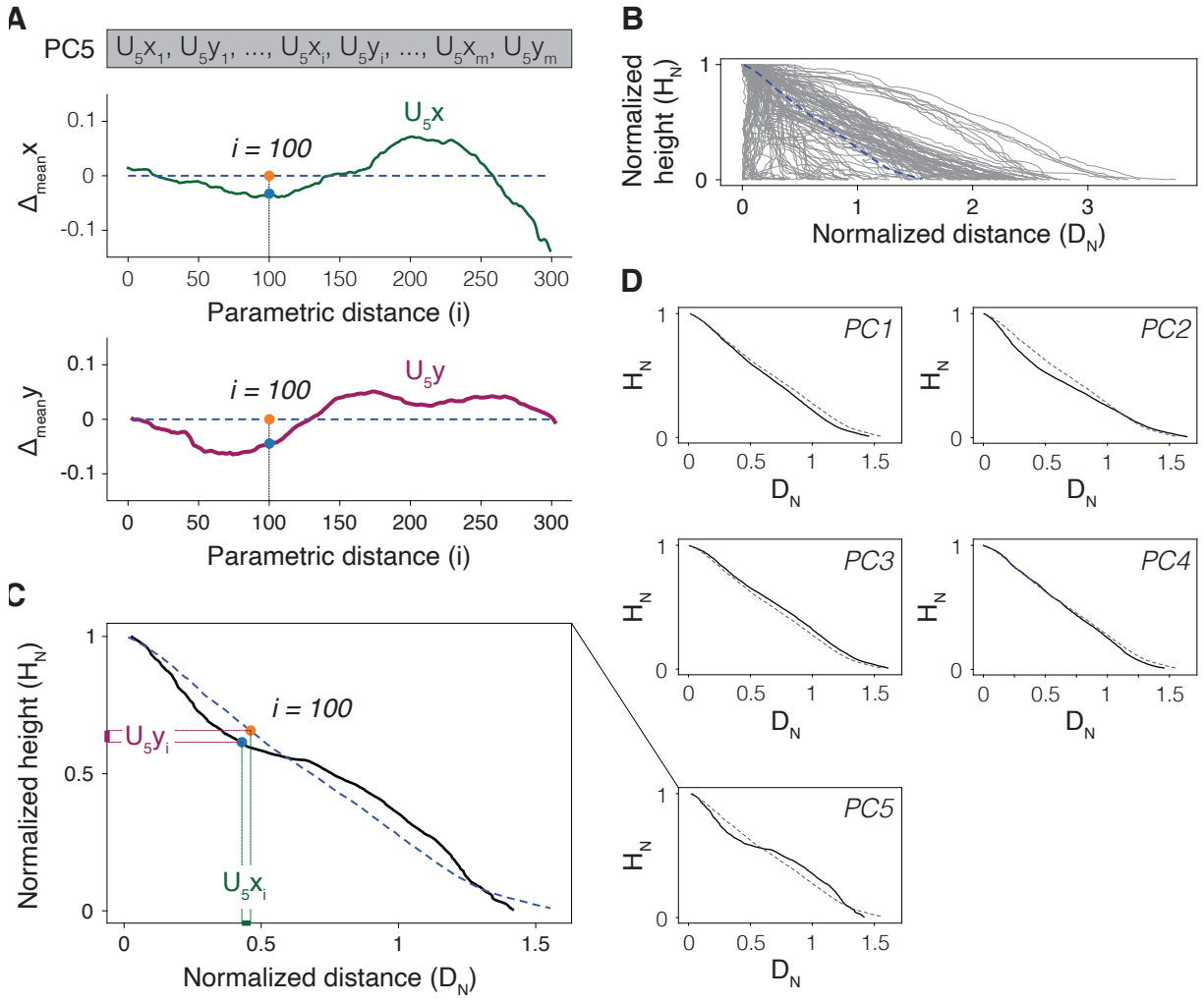

Figure 3.8. Visualization of principal components (the vectors of the U matrix from SVD decomposition). A) Example of principal component 5, with graphs representing the values of the principal component in the x- and y-directions, plotted against the parametric distance along the profile. These values are centered on the mean profile (represented by the blue dotted line). The orange and blue points represent the values of the mean and principal component, respectively, at a parametric distance of i=100. B) Graph plotting all cropped and normal-ized profiles from the training dataset (gray lines) and the average profile of the set (dotted blue line). C) PC5 values added to the mean scarp profile (black profile), along with the mean profile itself (blue dotted line), to visualize the manner in which the variance contained in PC5 is distributed along a profile. D) Profile visualizations of the first five principal components (black lines), along with mean scarp profile (blue dotted line).

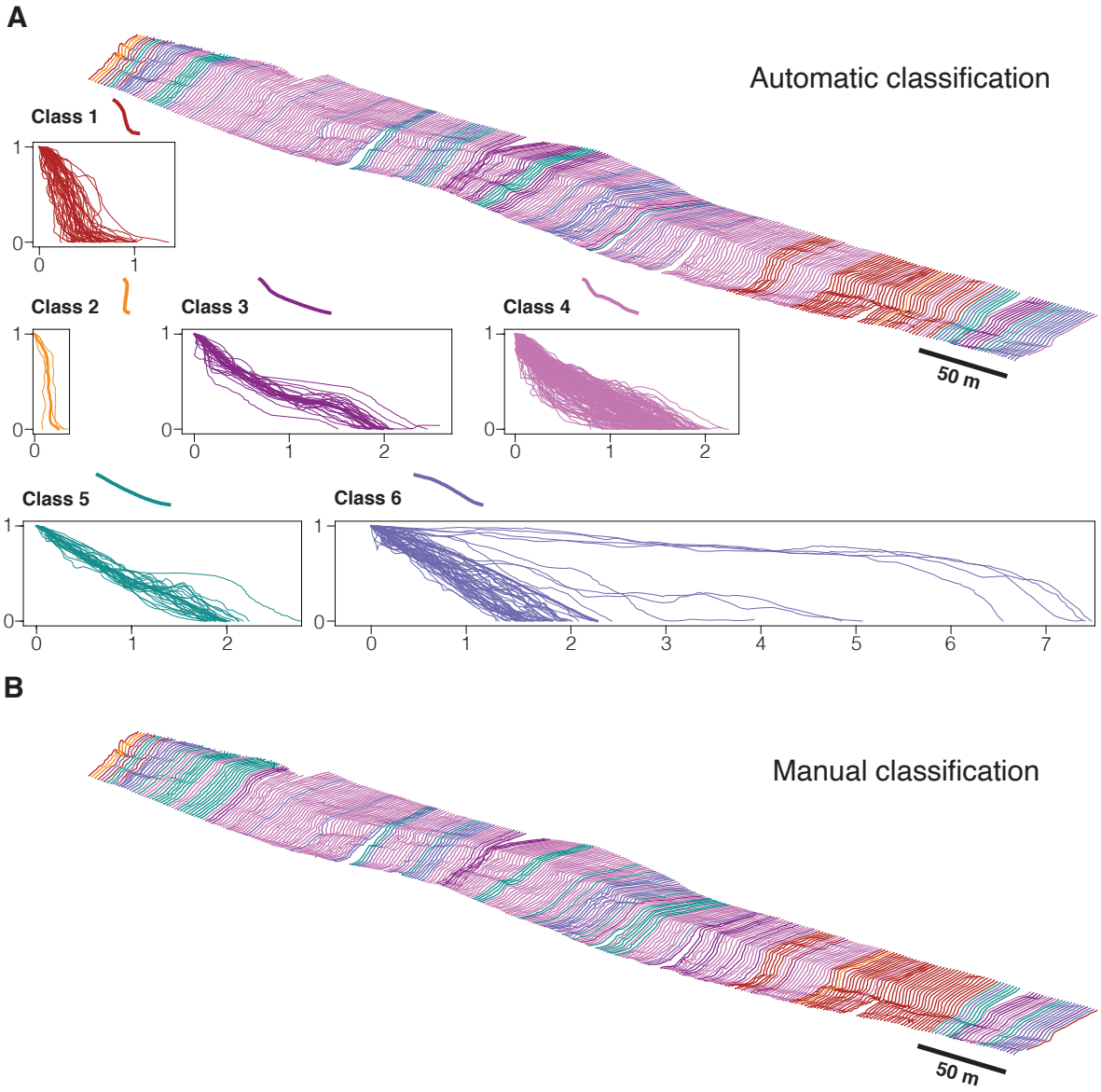

Figure 3.9. A) Classification results by the SVM for Gildruholtsgja, showing both the original uncropped 3-D profiles in situ along the scarp, as well as graphs of the 2-D cropped and normalized profiles sorted by class, with the profiles in bold representing the average form of each class. The profiles next to the class name repre-sent the form of the average profile from each class of the training dataset. B) Manual classification results.

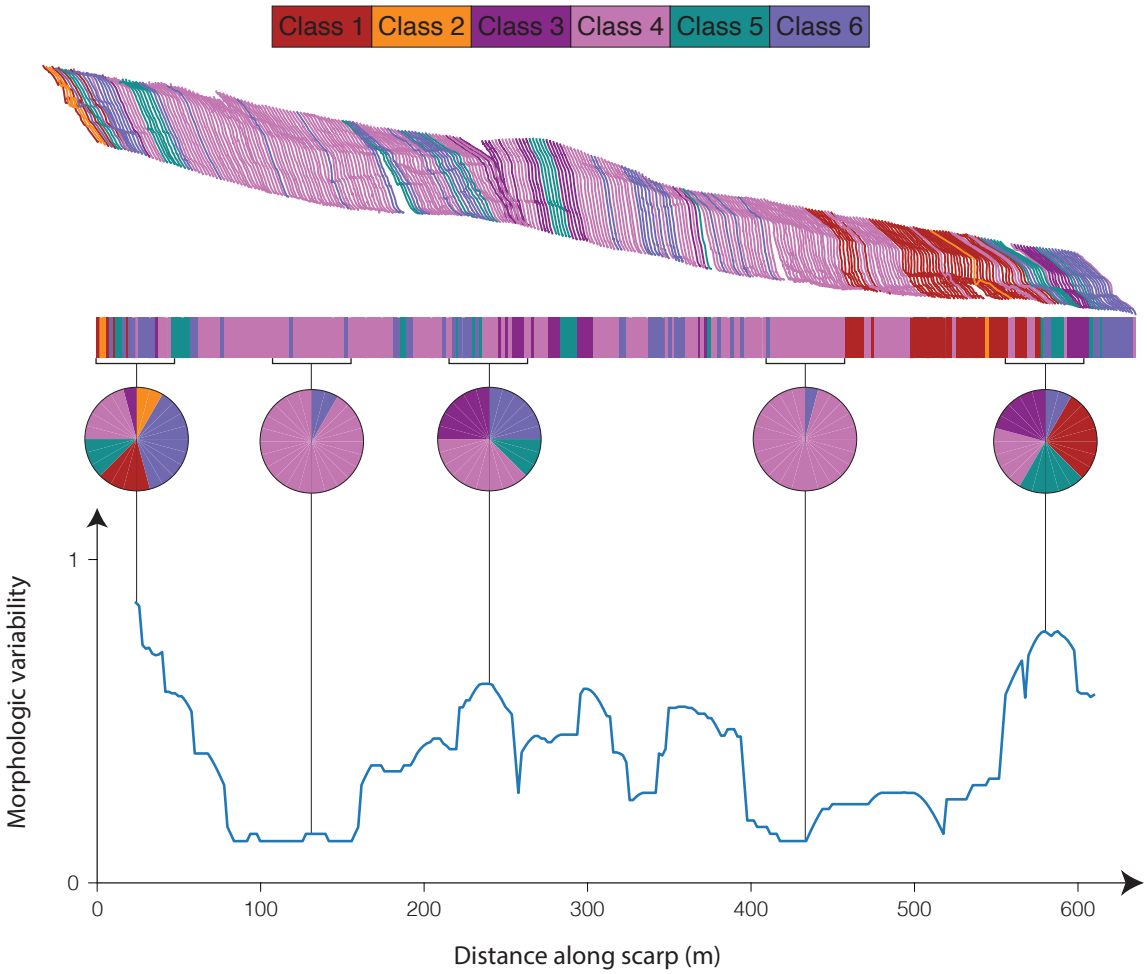

Figure 3.10. Morphologic variability calculated along strike of the Gildruholtsgja fault scarp.

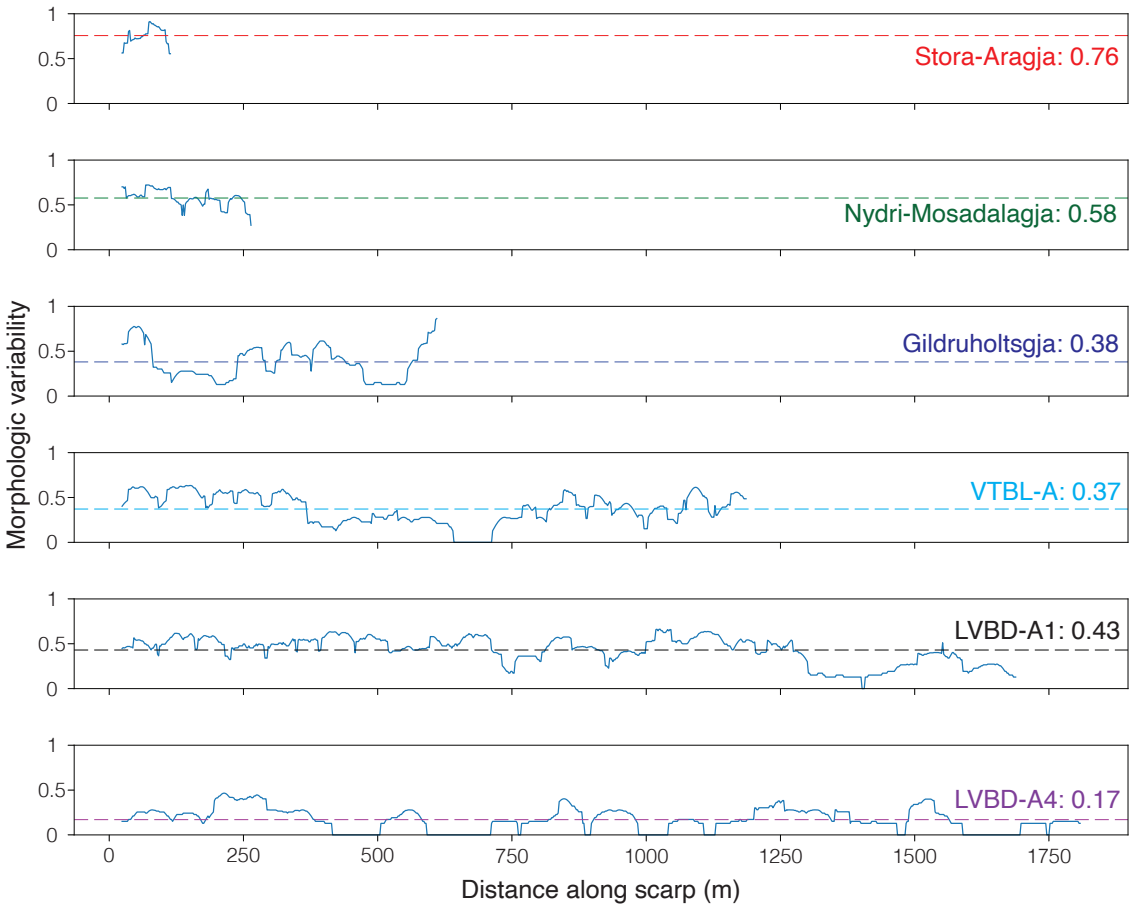

Figure 3.11. Morphologic variability results for six scarps: Stora-Aragja, Nydri-Mosadalagja, Sodulholagja (Iceland), VTBL-A (Volcanic Tablelands, CA), LVBD-A1, LVBD-A4 (Medicine Lake Volcano, CA). The dotted lines correspond to the average variability values for each scarp, with the value recorded after the scarp name.

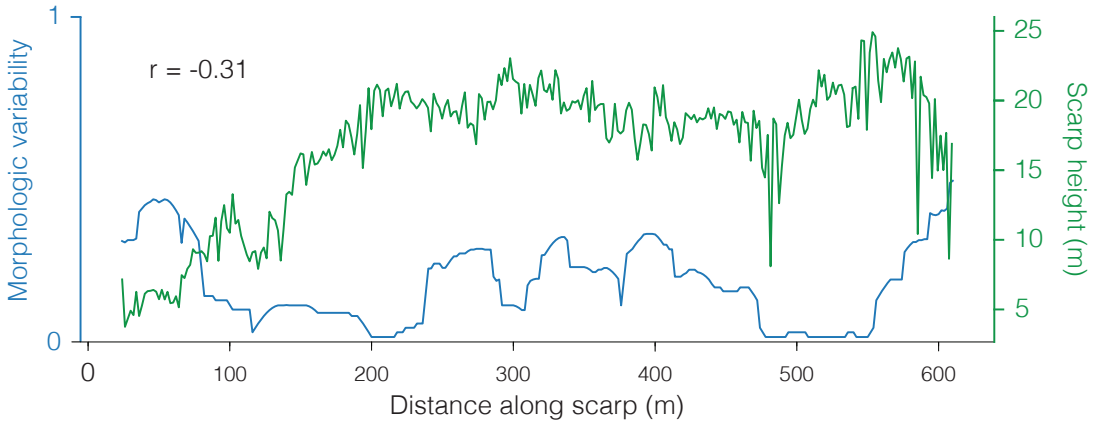

Figure 3.12. Morphologic variability (blue) and scarp height (green) of Gildruholtsgja plotted against the distance along the scarp. r is the Pearson coefficient of the correlation between morphologic variability and scarp height.

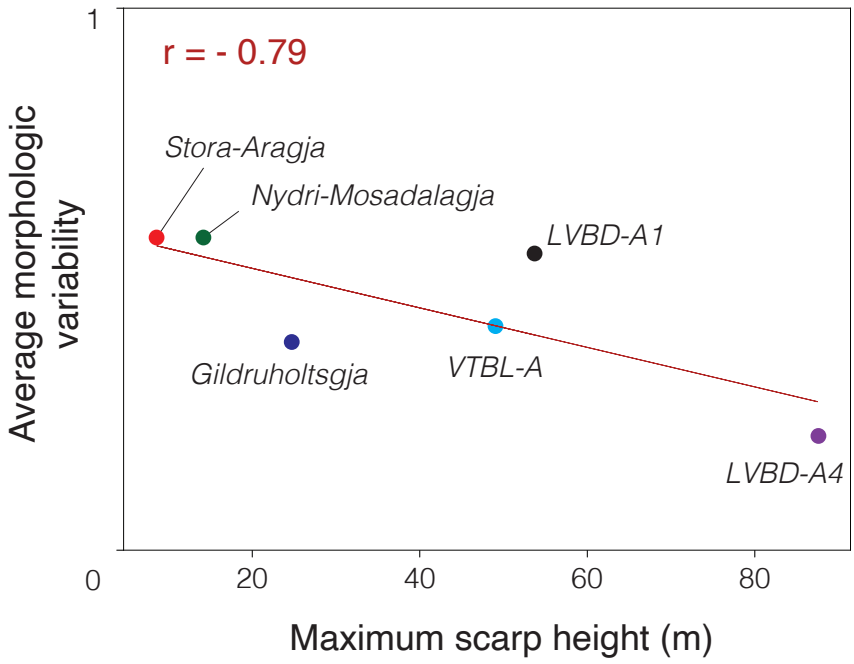

Figure 3.13. Plot of the average morphologic variability against the maximum scarp height of each of the six scarps. r indicates the Pearson correlation coefficient between average morphologic variability and maximum scarp height.

Table 3.1. Results of model evaluation

	F1- score	Precision	Recall	Support	Accuracy	Cohen's Kappa	MCC
Class 1	0.79	0.98	0.87	5.4			
Class 2	0.98	0.94	0.96	8.2			
Class 3	0.63	0.74	0.66	6.7			
Class 4	0.77	0.60	0.66	7.4			
Class 5	0.65	0.66	0.63	4.1			
Class 6	0.96	0.89	0.92	10.2			
Average	0.80	0.80	0.78	42	0.81	0.77	0.78
Weighted average	0.84	0.81	0.82	42			

CHAPTER 4: HOT SPRING SINTER, ACID SULFATE ALTERATION, AND THE MORPHOLOGIC VARIABILITY OF FAULT SCARP PROFILES FROM THE STILLWATER SEISMIC GAP, DIXIE VALLEY, NV

4.1 INTRODUCTION

Fault scarps are steps in the landscape created by surface-rupturing faults. Study of their morphology can supply paleoseismic information, such as the timing and size of past earthquake events, but the form of a single fault scarp can show great variability along the length of the scarp, complicating its interpretation. One control on fault-scarp form is the lithology cut by the scarp. Fault zones in geothermal fields provide a chance to run a controlled experiment, where hydrothermal alteration and mineral precipitation modify the properties of the host materials over short distances.

We present a case study from Dixie Valley, Nevada, where three adjacent units (alluvial and colluvial gravels, quartz-rich hot spring sinter and silicified gravels and clay-rich, acid sulfate alteration in a zone of ongoing fumarole activity) are offset by a single Holocene fault rupture. The fault scarp is in the Stillwater Seismic Gap segment of the Dixie Valley fault, named thus due to its location between coseismic surface ruptures of the 1915 Pleasant Valley earthquake to the north and 1954 Dixie Valley earthquake to the south.

Here, we document the morphologies present along the fault scarp in these three units to quantify the scarp profile form and how it varies with lithology. We use the morphologic variability metric developed by Brigham & Crider (2022). The study site provides the opportunity to apply the morphologic variability metric to a scarp where age and climate are kept constant but where lithologic characteristics vary between units. If all units have similar morphologic variability

values, the variation in profile form can be attributed to fault zone-scale attributes (e.g., primary fault structure). If each unit has distinct morphologic variability values, the variation in profile form can be attributed to lithological changes. This provides a test of the morphologic variability metric as a tool for discriminating among faults scarps with different styles of evolution. Additionally, we demonstrate that scarp form in this area can be used to identify the location and style of hydrothermal alteration.

4.2 BACKGROUND

The Dixie Valley fault is a range-front normal fault that bounds the east side of the Stillwater Range in western Nevada, United States (Figure 4.1). The Stillwater seismic gap is situated in the northern section of the Dixie Valley fault and separates fault scarps formed during the 1915 Pleasant Valley earthquake and the 1954 Dixie Valley earthquake (Wallace & Whitney, 1984). Though no historical surface ruptures can be found in the Stillwater seismic gap, a series discontinuous fault scarps are present along this section. Trench studies, radiocarbon ages and morphometric analyses of scarp profiles obtained in the gap indicate that these scarps were likely formed during a single Holocene event that occurred between 2 and 2.5 ka (Lutz et al., 2002; Bell et al., 2004). Vertical throw across the fault scarps in this section average 2-3 m, reaching maximums of 5-6 m. Based on rupture length and average slip estimates, the moment magnitude of the late Holocene earthquake is estimated to be about M_w 7.3 (Wesnousky et al., 2003).

The scarps cut alluvial-fan and colluvial deposits that bury gravels deposited during the high stand of pluvial Lake Dixie, dating to approximately 12 ka (Thompson & Burke, 1973) and predate the approximately 1.5 ka Mono Crater ash (Bell, 1981; Bell & Katzer, 1990). The alluvial-fan and colluvial deposits are composed of sandy pebble-to-cobble gravel and gravelly sand and represent

many discrete water-flood and debris-flow events, as well as rockfall and shallow slides from the steep rangefront (Bell & Katzer, 1990).

The Stillwater seismic gap is located within the Dixie Valley geothermal field, and evidence of hydrothermal activity is abundant at and near the study site (Figure 4.2). Extinct Holocene sinter deposits, including geyserite, emanating from fault splays along the rangefront escarpment indicate the former presence of high-temperature hot spring vents (Lutz et al., 2002). At the base of the geyserite, interbedded sinter and stream cobbles and silica-cemented gravels create terraces of resistant material, dating to approximately 3.4 ka (Lutz et al., 2002). The Frying Pan Fumaroles are associated with intense argillic alteration of the rangefront bedrock, creating sections of bleached pink and yellow rock. Weak fumarolic activity is ongoing, but initial alteration of this area began approximately at 5 ka (Lutz et al., 2002). The 2-2.5 ka scarp displaces the sinter, the silica-cemented gravels and the altered areas.

4.3 METHODS

4.3.1 Structure-from-Motion photogrammetry and field mapping

We collected drone-acquired aerial imagery for use in Structure-from-Motion photogrammetry (Westoby et al., 2012). The survey included five ground control points, surveyed with Trimble R2 GNSS receivers. We used Agisoft Metashape to match features between 2429 images to create a three-dimensional model of the field site and derived products such as a 1.5 cm^2/pixel resolution orthorectified image and a 6 cm^2/pixel resolution digital elevation model (DEM) of the study area (Figure 4.2; see details in Callahan et al., 2023). We made detailed observations in the field of scarp form and evidence of hydrothermal alteration and mapped the fault scarp trace and the hydrothermal features onto our SfM-derived DEM (Figure 4.3).

4.3.2 Quantitative analysis of morphologic variability

We examined fault scarp profiles in three areas: where the scarp is in uncemented alluvial gravels away from hot-spring activity; where the scarp is in sinter and silica-cemented gravels; and where the scarp cuts hydrothermally altered bedrock related to ongoing fumarole activity. To quantitatively compare the profile forms from each section of scarp, we extract scarp normal profiles from the SfM-derived DEM. For each unit, we sample profiles from a section where the scarp location is known and where profile morphology is not affected by the rangefront alluvial channels or by anthropogenic modification (Figure 4.3, boxes A-C). We review the forms of the extracted profiles and determine morphologic classes that represent the variation in profile forms in all three units.

To quantitatively determine the degree to which profile form varies in each section, we use a morphologic variability metric (Brigham and Crider, 2022). The metric 1) imparts information as to the number of classes present in the scarp or section of scarp; 2) accounts for the proportions of the present classes; and 3) reports changes in morphology at a high enough resolution to capture the effects of most geomorphic processes.

To calculate the metric, we pre-process and classify the profiles from each section into our chosen morphologic classes using the support vector machine method (Brigham and Crider, 2022). We then calculate the proportion p_{class} of each class (ranging from 0 to 1) within a given window along the scarp and the standard deviation (σ_{prop}) from the mean (μ_{prop}) of these proportions. We also determine the number of classes represented in that window. We thus obtain the variability metric v_s:

$$v_s = \sqrt{\frac{\sum\left(p_{class} - \mu_{prop}\right)^2}{N_{total\ classes}}} + \frac{N_{classes}}{N_{total\ classes}}$$

The metric is normalized, so that 1 represents a landform section that presented all classes in equal proportions. The value 0 is assigned to a scarp section with a single morphologic class (Figure 4.4). To compare the scarp sections to one another, we use the mean morphologic variability of each section as a representative metric.

4.4 RESULTS

4.4.1 Description of scarp form in each lithologic unit

4.4.1.1 Alluvium and colluvium

The Holocene fault scarp is the most easily discernible in the westernmost portion of the study area (section A) in the range-derived alluvial and colluvial material. Scarp profiles in the alluvial and colluvial section have a mean height of 6.2 m (± 0.94 m), with an average slope 27.4° (± 8.7°). In many areas, the slope takes on a familiar shape for scarps in unconsolidated material: rounded crest and toe, with a flat mid slope (Figure 4.5Ai.). However, the high degree of fluvial dissection along the range front is apparent in the scarp profile morphology, where the traditional fault scarp shape is sometimes replaced with concave upwards slopes formed by gullying (Figure 4.5Aii.) and profiles cross-cut by channels (Figure 4.5Aiii.)

4.4.1.2 Sinter and silica cemented gravels

Large sinter deposits characterize the central portion of the study area in the form of geyserite, a form of silica found in high-temperature hot spring systems. Near the base of the geyserite, we find aprons of silica-cemented gravel that are cut by the Holocene surface rupture. Scarp profiles in the silicified section have a mean height of 5.8 m (± 0.8 m), with an average slope of 23.2° (± 10.2°). Depending on the level of cementation, the scarp can take on a range of forms, including: an armored convex-upwards upper slope with a free face in the lower slope (Figure 4.5.

B. i.); a convex-upward slope (Figure 4.5. B. ii.); or a slope with short-scale heterogeneities introduced by rubble from collapse of the cemented apron (Figure 4.5. B. iii.)

4.4.1.3 Fumarole-altered materials

The eastern portion of the study area is characterized by altered, bleached white, yellow and pink rock, a consequence of current and past fumarolic activity and subsequent acid sulfate alteration. We distinguish between recent and inactive fumaroles through measurements of ground temperature (Figure. 4. 3). The fumarolic activity along the fault complicates its surface expression in the alteration zone. The easily erodible materials do not preserve the original scarp shape. Instead, the scarp slope relaxes until it reaches a change in lithology, creating a fault line scarp (Figure 4.5. C. i.), or is assimilated into the larger hillslope (Figure 4.5. C. ii.).

4.4.2 Morphologic variability analysis

We extract scarp-normal profiles from our digital elevation models of sample areas A, B and C in the alluvial fan, the sinter and the fumarole-altered areas. After examining the data, we identified six morphologic classes of scarp profiles (Figure 4.4A.): 1) convex-upward profiles; 2) concave-upward profiles; 3) profiles with V-shaped discontinuities; 4) profiles with free face in lower portion of profile; 5) straight profiles with visible rubble; 6) profiles with free faces in upper portion of profile. Once the classes were defined, each profile was assigned to morphologic class using the classification algorithm described in Brigham and Crider (2022). The analyzed scarp sections are represented with each profile colored by class (Figure 4.6).

Each scarp segment contains profiles of two or more classes. All three sample sections contain concave up profiles (class 2), which is also the most common profile form that we surveyed. Scarps in alluvium and colluvium also present numerous convex-up profiles (class 1).

Scarps in silica-cemented gravels present five morphologic classes, but class 3 (profiles with V-shaped discontinuities) is not represented. Scarps in fumarole-altered materials only contain profiles belonging to class 2 or class 6 (free face in upper portion of profile).

Using the classification results, we calculate the morphologic variability of each sample section in a 12-meter-moving window (Figure 4.6, blue curve), as well as the mean morphologic variability for the section (orange dashed line and number). The fault scarp in the fumarole-altered section exhibits the lowest morphologic variability (2 classes represented of the six, average morphologic variability value of 0.18). The fault scarp in alluvium and colluvium (3 classes, 0.31) showed intermediate morphologic variability. The scarp in sinter and cemented gravel showed the most variability in form (5 classes, with an average morphologic variability of 0.57).

4.5 Discussion

Through field observations and morphometric analyses, we have catalogued the variations in profile shape of a single-age Holocene fault scarp hosted in three areas with different amounts and styles of hydrothermal alteration. Our case study emphasizes the need to consider composition during paleoseismic interpretation of fault scarps, particularly in hydrothermally active areas, and illustrates the utility of along-strike morphologic variability in determining lithologic boundaries. We find that each lithologic unit has a distinct mean morphologic variability value, suggesting that patterns in profile form change depending on the type and amount of hydrothermal alteration. Fumarolic activity significantly complicates both locating and interpreting the single-event scarp, by altering the host rock to rapidly erodible material and leading to either the erasure of the scarp or the creation of a fault line scarp along the boundary with less altered and more competent bedrock. Due to the difficulty in identifying the scarp and the erodibility of the materials, we caution that over-estimating slip during a single event in areas with fumarolic activity is possible,

as a smaller single event scarp rapidly recedes to the larger bedrock fault scarp line. Large-scale alteration of the host rock to easily erodible clays along the fault in this area leads to the establishment of more uniform hillslopes, excepting any lithologic boundary or fumarole feature itself. Fault scarps associated with fumarolic activity thus have low morphologic variability values.

Scarp morphologies associated with high temperature hot spring systems have different characteristics than those in areas with fumarolic activity. Deposits of geyserite and associated aprons of silica-cemented gravel are the complicating factors. In the upper slopes of the scarp, the mantle of geyserite can shield the slope from erosion, preserving convex-upwards forms, or it can fracture and topple, creating forms with a lot of decimeter- to meter-scale heterogeneity. The degree of silica-cement can lead to steps and free faces (highly cemented) or to profiles with rounded crests and toes (poorly cemented). Scarps in sinter deposits seem to more or less accurately record offset along the fault, though the variability in form could lead to confusion in identifying the toe and the crest of the scarp. The interplay between the scarp, the sinter deposits, and their lateral variability in strength leads to higher morphologic variability values in fault scarps associated with high-temperature hot springs.

Scarps in unaltered and unconsolidated material, such as alluvium or colluvium, offer the best chance to correctly assess offset. However, heavy gullying and fluvial dissection does lead to scarp-parallel morphologic variability, so proper selection of the assessment site is key.

4.6 CONCLUSION

We examined fault scarp profiles within different lithologies along the Dixie Valley fault in western Nevada and find that alteration has influenced the mean morphologic variability value. The fault scarp in the fumarole-altered section exhibits the lowest morphologic variability, the fault scarp in alluvium and colluvium shows intermediate morphologic variability, and the scarp

in sinter and cemented gravel, the most similar to that of jointed bedrock, shows the most variability in form. This controlled experiment shows that the morphologic variability metric changes with lithology and is thus sensitive to parameters such as rock strength and mode of degradation. By expanding and refining our study of fault scarps associated with hydrothermal alteration and quantitatively assessing their morphologic variability, we have the potential to create an automatic landform analysis tool that can inform on the type of hydrothermal alteration present along a fault. This type of tool has many applications both in geothermally active areas on Earth and on other planets.

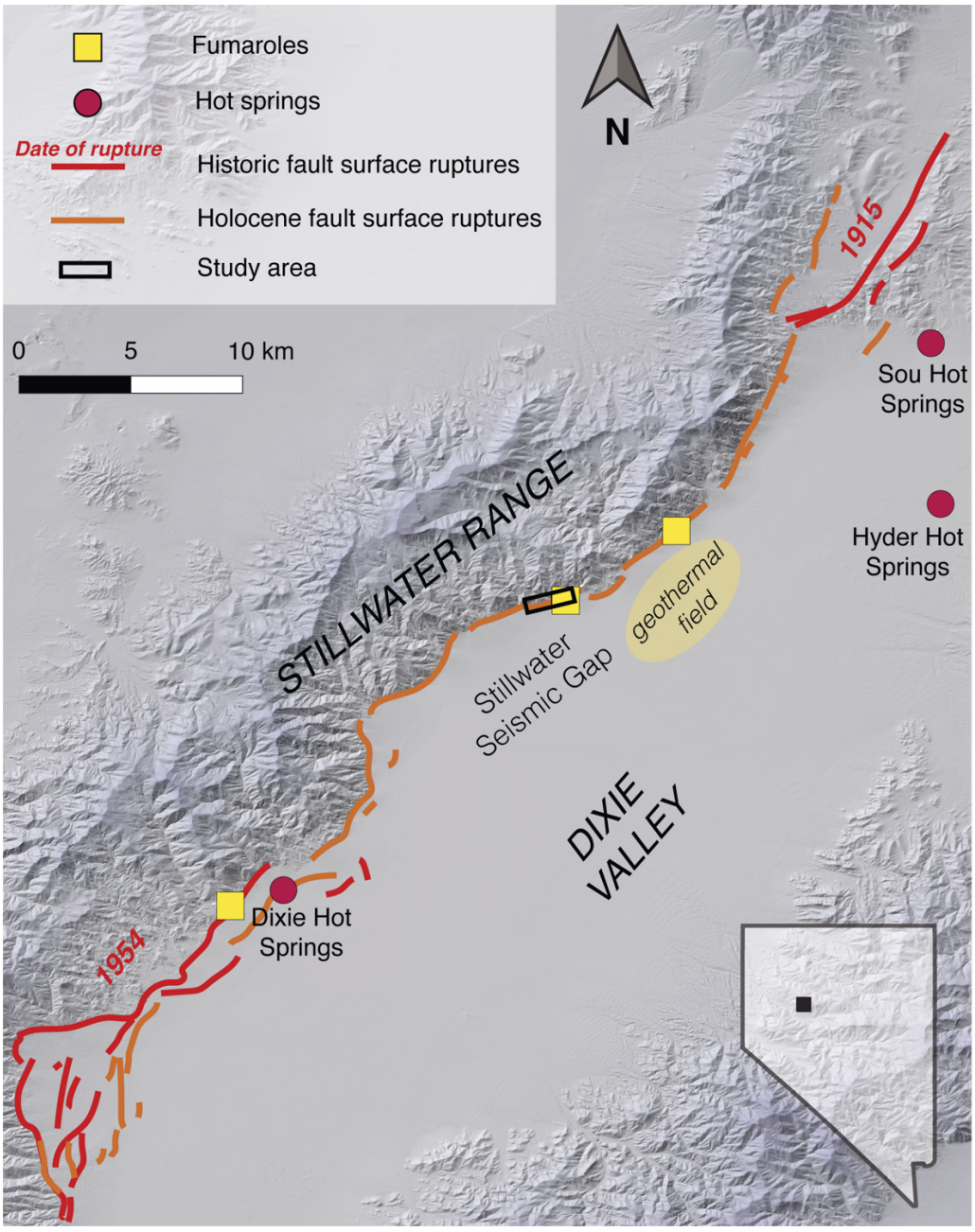

Figure 4.1. Map of study site at the base of the Stillwater Range (inset at bottom right shows location in Nevada). Red lines indicate the traces of surface ruptures from the 1915 and 1954 earthquakes, orange traces indicate traces of older Holocene ruptures. Black box indicates location of SfM survey. Hydrothermal features also indicated on map. Modified from Lutz (2002) and Callahan et al. (2019).

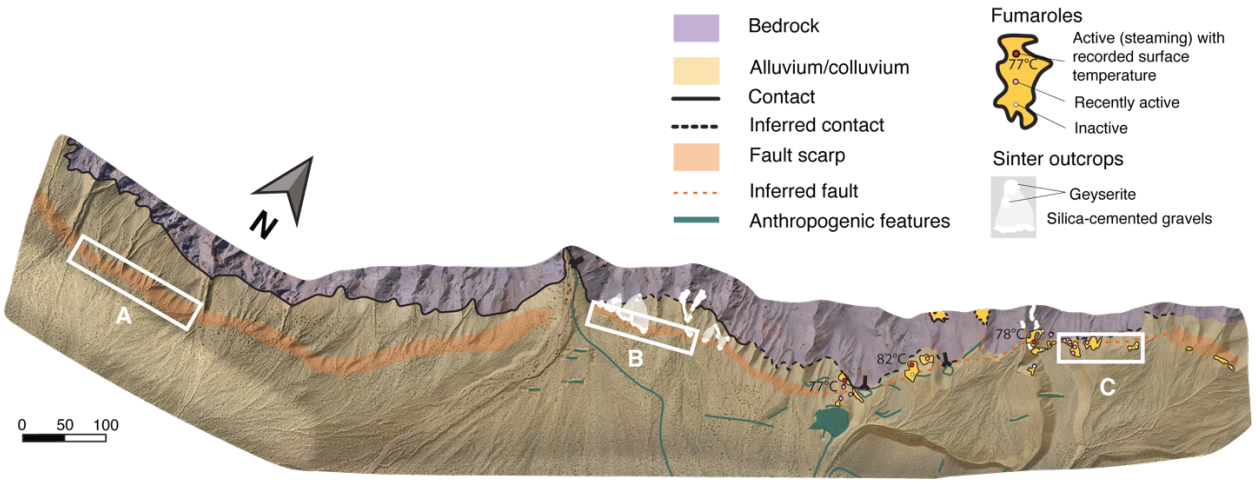

Figure 4.2. Map of fault scarp and hydrothermal features in study area. White rectangular boxes indicate where scarp profiles were extracted A) in the alluvial fan/colluvial deposits; B) in the sinter and silica-cemented deposits; C) in the fumarolic altered material.

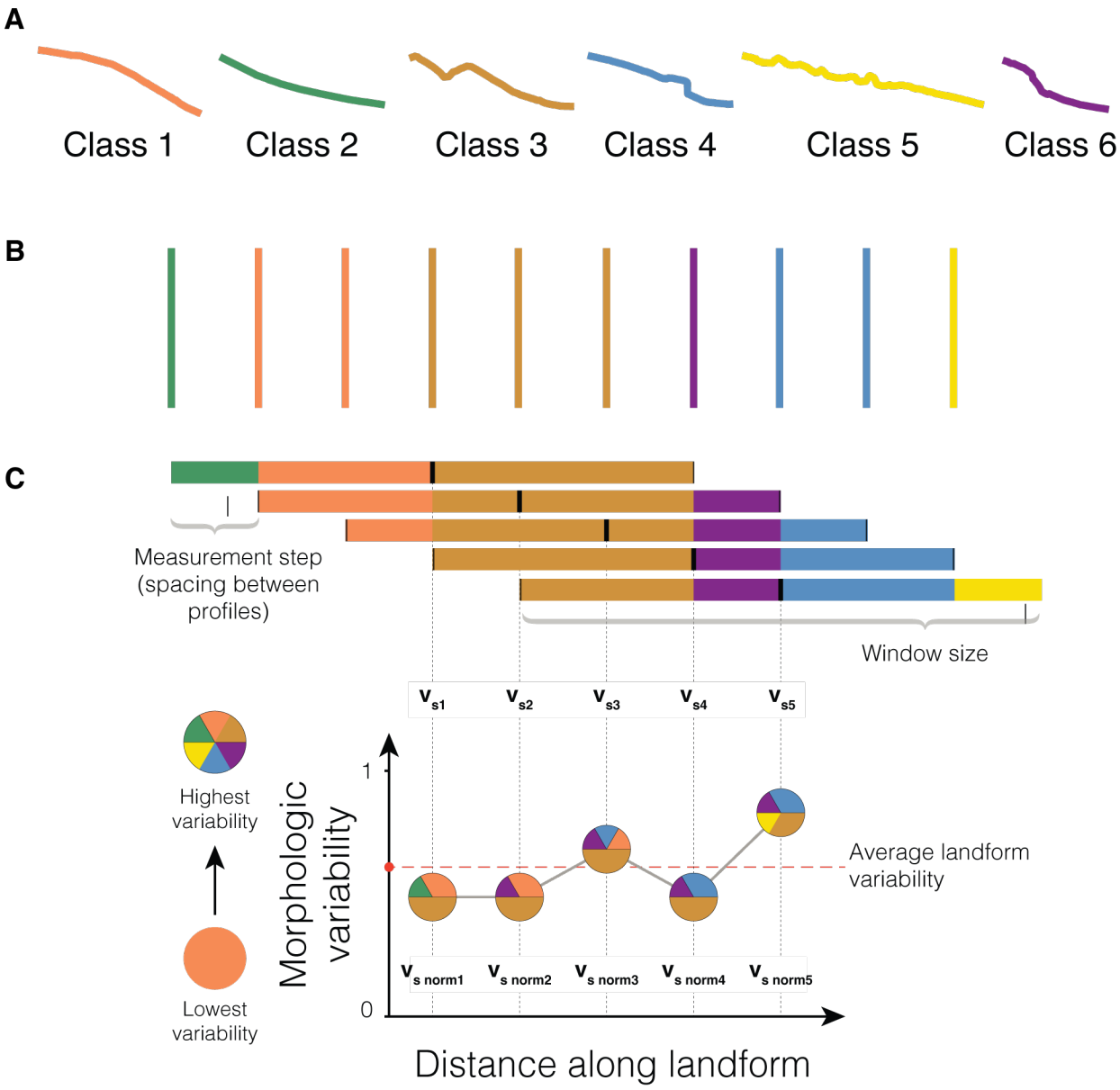

Figure 4.3. A) Morphologic classes determined by inspection of scarp-normal profiles taken from each unit. B) Example of possible arrangement of profiles of different morphologic classes along a section of scarp (map view). C) Schematic illustration of how morphologic variability is measured in a moving window along the scarp section (modified from Brigham and Crider, 2022).

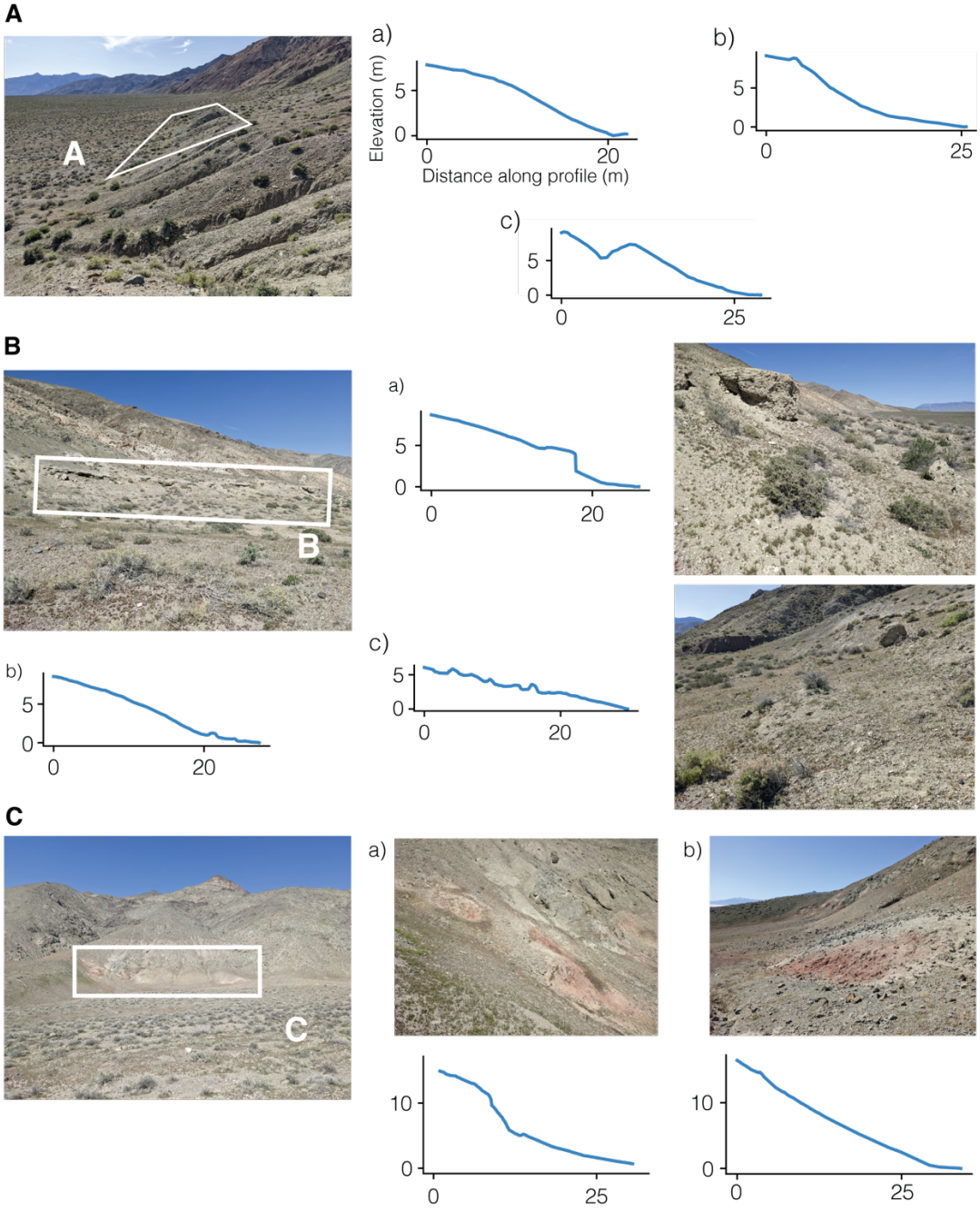

Figure 4.4. Scarp-normal topographic profiles and images illustrating the types of morphologies found in A) alluvial fan and colluvial material; B) sinter and silica-cemented gravels; C) fumarole altered material. All profiles indicate distance along the scarp in meters on the x-axis and height in meters on the y-axis.

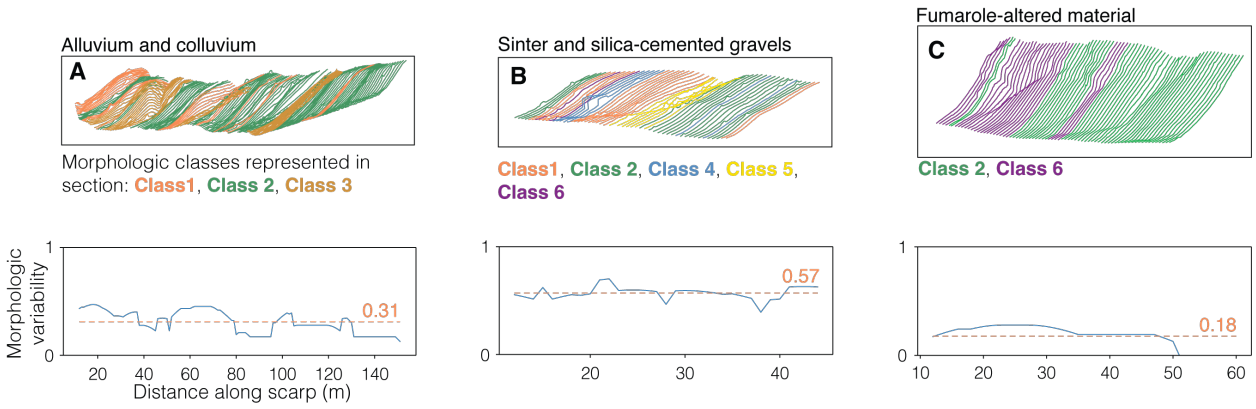

Figure 4.5. Profiles colored by morphologic class (above) and morphologic variability calculated along scarp section with mean morphologic variability value (below) for: A) alluvial fan and colluvial material; B) sinter and silica-cemented gravels and C) fumarole-altered material.

CHAPTER 5: QUANTITATIVELY RELATING PROCESS TO FORM IN FAULT SCARPS IN JOINTED BEDROCK USING MORPHOLOGIC VARIABILITY

5.1 INTRODUCTION

Fault scarps are the product of lithologic, tectonic and geomorphic characteristics that vary widely both within a single scarp and between sites. Understanding the temporal and spatial effects of these processes on scarp morphology is important, since they affect interpretations of paleoseismicity (e.g., Zou et al., 2021), fault zone structure and age (e.g., Sare et al., 2019) and geomorphic process rates (e.g., Tucker et al., 2011). Isolating these processes currently requires carefully selecting and studying "natural laboratories", where a large proportion of the parameters are already constrained or can be reasonably assumed. Comparing scarps at similar stages of evolution but in different settings (e.g., Scarciglia et al., 2022) can yield the morphologic signatures of specific processes, but complications remain in determining rates of processes and characterizing the overall evolution of the landform. Conversely, comparing sites of different stages in similar settings (e.g., Wallace, 1977; Hilley and Arrowsmith, 2008) can inform the rate and style of overall morphologic change in a landform type, but finding adequate sample sites and identifying specific processes is difficult.

Recently, the increasing number of remotely sensed geospatial datasets has resulted in information being available to workers studying landforms at a higher volume and resolution that ever before. Following suit, "big data" approaches, where workers use unsupervised learning algorithms and statistical tools to probe the structure of large datasets to identify, extract and classify specific features (e.g., J. Wu et al., 2021; Dyba & Jasiewicz, 2022; Kazemi Garajeh et al., 2022), have become increasingly popular. A less explored area of big data methods in landform

analysis involves using dimension reduction techniques, such as principal component analysis, to identify factors that are more likely to influence morphology (e.g., Bitencourt & Dillenburg, 2020; Martins et al., 2022; Mokarram et al., 2022), based on the amount of variance in the dataset a factor or linear combination of factors might explain. Big data methods and the availability of large amounts of data offer an opportunity to quantitatively capture and contextualize local variability in relation to big picture understanding, rather than having to try to minimize variability and find a scenario that is as simple and straightforward as possible for the natural laboratories approach. This approach is enticing when the evolution of a landform is very complex, as is the case of the profile form of fault scarps in jointed volcanic rock, which are dependent on time, position along the landform and surrounding conditions. However, much caution and user input is needed when applying big data methods before reaching an interpretation, including pre-processing data to minimize any instrument error and focus on features or locations of interest; determining the appropriate analysis method to use based on dataset characteristics; choosing appropriate datasets of comparative factors that will likely explain most of the changes in morphology based on expert knowledge; interrogating model outputs and assessing causal links based on expert knowledge; and validating inputs and outputs in the field.

In this chapter, I define a methodological framework to quantitatively investigate the relationship between form and process in the case of fault scarps in jointed volcanic rock. I incorporate aspects of both the natural laboratories and the big data approaches. I propose that questions pertaining to form and process of fault scarps in jointed volcanic rock should be considered at four distinct spatial scales (a portion of a scarp, a whole scarp, a regional group of scarps, and between regional groups) and that certain methods are better suited for both certain scales and certain use cases (Figure 5.1). Like both natural laboratories approaches, I use the

variation in scarp morphology between scarps of a single site and the variation in profile form of scarps among sites to isolate the morphologic effect of specific parameters. I also use big data statistical approaches to reproducibly and objectively quantify changes in scarp morphology and to assess the relative importance of parameters based on data structure.

As a test of this framework, I use both remotely-sensed and field-acquired data from fourteen jointed-bedrock-hosted normal fault scarps that I had observed in the field in southwest Iceland, Kilauea Volcano, Hawai'i, Owens Valley, California, and the flank of Medicine Lake Volcano, California. I quantify along-strike changes in scarp-normal profiles by adapting an algorithm proposed by Brigham and Crider (2022) to calculate the morphologic variability of a landform. I find that the along-scarp morphologic variability correlates with profile height for most scarps, but that changes in morphologic variability at broader scales are more strongly correlated with changes in vegetation and temperature. However, at the regional scale, climate data and satellite imagery are much easier to obtain than other types of datasets, such as rock mass characteristics, so no definite interpretations can be drawn without collecting measurements of many more types of parameters related to the scarp and the local environment along more scarps in different settings. In spite of current limitations, this framework offers workers a path forward to interpreting observations of fault scarps in jointed bedrock from around this planet and others in a manner that accounts for local variability.

5.2 Background

Much of the work concerning the morphology of fault scarps has focused on establishing their age. In unconsolidated material, earlier work that highlighted the possibility of morphologic dating by estimating scarp diffusion (e.g., Nash, 1980; Hanks et al., 1984; Andrews & Hanks, 1985; Mattson & Bruhn, 2001; Pelletier et al., 2006) has been applied and improved using high-

resolution data (e.g., Hilley et al., 2010; Wedmore et al., 2020; Hornsby et al., 2019) and automated methods (e.g., Sare et al., 2019; Vega-Ramírez et al., 2021). Though complicating factors do exist, such as competing erosional models (e.g., Tucker & Bradley, 2010), modification of slopes by processes that vary along strike (e.g., Avouac, 1993) and changes in material properties through time (e.g., Holtmann et al., 2023), this approach can be used to determine relative ages of Holocene scarps in cohesionless material under the same climatic conditions (Avouac, 1993). In limestone fault scarps, workers found a time-dependent evolution of fault-scarp roughness, with degradation level increasing with scarp height (Stewart, 1996), which can be remotely detected using high-resolution digital elevation models (Wiatr et al., 2015; He et al., 2016; Karamitros et al., 2020). Erosion rates can also be inferred by using geometric models (Tucker et al., 2011). These methods are adapted for the case of fault scarps in unjointed bedrock, where the slip surface of the fault is identifiable and represents the initial dip of the scarp. In jointed bedrock, fault slip surfaces can rarely be found during field investigations, so assumptions about the initial conditions in unjointed bedrock, and thus models of slip surface roughness and erosion, are not applicable.

Many conceptual models exist investigating the evolution of fault scarps in jointed bedrock (e.g., Grant & Kattenhorn, 2004; Martel & Langley, 2006; Pinzuti et al., 2010; Hardy, 2013; Bubeck et al., 2018), but a quantitative morphologic dating system has yet to be established. Algorithms quantifying scarp morphology in jointed bedrock have focused on understanding the structural characteristics and development of the fault, using scarp height, width and slope to characterize fault mechanics and potential seismic hazard (e.g., Hodge et al., 2019; Wolfe et al., 2020; Scott et al., 2022). Given that many normal fault scarps in jointed rock are located in volcanically active areas, the interplay between scarp morphology and the processes that modify it becomes even more complex, as lava flows can modify or resurface scarps at any time in their

history. Many different structural, geomorphic and volcanic processes could yield profiles of similar scarp height, width and slope, thus patterns in scarp profile form, rather than a single profile, may better reveal which processes influence scarp form at a given stage of evolution and how the forms and processes change as the scarp evolves (Chapter 2).

Brigham & Crider (2022, Chapter 3) developed an algorithm to quantify along-strike variations in scarp form, through semi-automatic classification of typical scarp profile forms and calculation of a morphologic variability metric, which measures the number and proportion of form classes in a moving window along a linear landform. The morphologic variability of the scarp can then be compared to other measurements taken along the scarp to understand how a given parameter might affect scarp morphology. This method employs a supervised learning algorithm, where the worker defines morphologic classes, constructs a representative training dataset for each class and classifies unlabeled profiles by proximity to the labeled data in principal component space. This type of approach works well for smaller datasets where all or many of the profiles can be inspected manually, or the field areas are well known and visited by the worker and the morphologic types are distinct in the field. In this scenario, the worker has a good first order understanding of the trends in profile form and the number of classes needed to adequately represent the variation in form. However, if there are too many profiles to review manually (>1k) and these profiles come from scarps or sections of scarps in areas that the worker is not familiar with, a big data approach is needed to separate profiles into different classes. For this study, I adapt and generalize the morphologic variability method to very large datasets where the range in profile form types is not well constrained by using an unsupervised learning algorithm to label profile classes (see section 5.3.3).

5.3 METHODS

5.3.1 Site selection

This study focuses on the fault scarps in jointed volcanic rock described in detail in Chapter 2. I analyzed five scarps on the east flank of Kilauea on the island of Hawai'i (United States), two scarps on the northern flank of Medicine Lake Volcano in California (United States), three scarps in the Volcanic Tablelands north of Bishop in California (United States), two scarps in the Vogar fissure swarm on the Reykjanes Peninsula (Iceland) and two scarps in the Thingvellir graben (Iceland). The scarps were chosen to represent a range of scarp ages, scarp heights, rock mass characteristics, volcanic effusion rates, structural characteristics and climatic settings to capture as large a number as possible of processes that influence the initial form and subsequent modification of the scarps (see Chapter 2 for detailed descriptions of the sites).

5.3.2 Profile extraction

I sourced our topographic data from 4 digital elevation models (DEMs) with resolutions of 1 m for Hawai'i and the Volcanic Tablelands, 2 m for Iceland and 10 m for Medicine Lake Volcano. For each scarp, I cropped the DEM to the area of interest, created a shapefile representing the general trend of the scarp and extracted scarp-normal profiles from the DEM along the line using Python Object-oriented Swath Profile (PyOSP) (Zhu et al., 2021). The spacing between the scarps is equal to the DEM resolution. I obtained a total of 56,366 profiles.

5.3.3 Clustering

5.3.3.1 Pre-processing fault scarp profiles

To remove some extraneous noise and to allow for even sampling across all profiles, no matter the original resolution of the DEM, I applied a B-spline to the positional coordinates of

each topographic profile and sampled the spline at a regular interval. To further ensure that profiles of different scales could be easily compared based on their overall form (rather than their maximum height), I normalized the height and distance values of the profiles by their maximum heights, so that all scarps had a maximum height of 1 while maintaining the aspect ratio of the original scarp. I then used the scarp height algorithm described in Brigham and Crider (2022) to automatically detect the crest and toe of the scarp and crop the profile to the area between these two points (Figure 5.2A). Since I wanted to reduce processing time and use some of the powerful feature extraction tools present in the field of computer vision to obtain clusters pertaining to scarp form, I converted my list of normalized and cropped profile coordinates into lower-resolution binary images that maintained the aspect ratio of the scarp (Figure 5.2B).

5.3.3.2 Feature extraction

To separate my profile images into clusters with meaningful distinctions between different profile forms, I need to segment our images into features that a machine learning algorithm can recognize and use to cluster profiles. This involves recognizing edges from the white pixels in our profile image and then patterns from those edges. To do this automatically, I employ the method of transfer learning, which involves applying one or more layers from a trained classification model designed to solve one problem to a different, but related, problem (Pan & Yang, 2010). Based on methodologies of image classification used in facial recognition (e.g., Dubey & Jain, 2020), vegetation identification (e.g., Wu et al., 2018; Gu et al., 2021) and agriculture (Swasono et al., 2019; Jiang, 2019), I used a pre-trained convolutional neural network (CNN) model named VGG16 (Simonyan & Zisserman, 2015) to extract these features from our binary profile images. In a simple, fully connected neural network, an input layer of neurons (in this case, the pixels from the images are assigned a value, or activation, of 0 or 1 based on pixel color) is connected to a

second layer by connections that are assigned certain weights and values termed biases. The resulting weighted sum determines the activations of the second layer, which is assigned its own set of weights and biases, determining the activations in the next layer, and so on. Each layer represents sub-components of the image, with each neuron representing a specific edge or pattern that forms the image (Figure 5.2.C). VGG16 relies on convolutional layers to classify images (Figure 5.2.D), which involves applying a filter made up of a 2D array of weights that are applied to an area of the image at a given stride, and a dot product between the filter and the pixel values of that area is calculated in each location, resulting in a feature map. Multiple convolutions are applied to the initial image, creating a hierarchical structure within the CNN. Each individual part of the scarp image makes up a lower-level pattern in the neural net, and the combination of its parts represents a higher-level pattern, creating a feature hierarchy within the CNN.

5.3.3.3 K-means clustering

Using the feature maps extracted from VGG16 layers as our input, I use a K-means clustering algorithm to separate our profile images into groups of similar form. K-means clustering is a simple unsupervised machine learning algorithm that starts with a defined number k of randomly selected centroids and iteratively calculates the optimal positions of these centroids. Unlabeled data points are allocated to each cluster by reducing the in-cluster sum of squares. I then assess the viability of these clusters by manually inspecting the first 100 members of each cluster group. I look at results of different numbers of classes and once I reach classes that begin to repeat profile types that I consider to be “similar enough” (e.g., forms that are likely the result of the same geomorphic processes), I choose the lower number of classes. I find that a value of k=7 clusters the profiles in a manner that suitably captures the variability of scarp form in the dataset (Figure 5.3). Profile form classification results by individual scarp are summarized in Figure 5.4.

5.3.3.4 Morphologic variability

To quantify along-strike changes in scarp form, I use the results of our clustering algorithm to compute the morphologic variability metric described in Brigham and Crider (2022). This metric assesses the number of classes and the proportion in which they are present in a moving window along the scarp. This value is then normalized so that the maximum variability value is equal to 1 (all classes are present in equal proportion) and the minimum value is equal to 0 (only one class is present). The size of the moving window is determined by the maximum spacing between profiles present in the group of scarps to be compared. To compare scarp form between multiple scarps, the mean morphologic variability values of each scarp can be used as a summary statistic, as shown in chapter 4. On a regional scale, I can calculate the regional mean morphologic variability value, or the mean of the mean morphologic variability values of scarps in a given region. Morphologic variability results by individual scarp are summarized in Figure 5.5.

5.3.3.5 Fault scarp parameter measurement

In this study, I focused both on parameters that were easily extracted from remote sensing data, such as aspect, scarp height, vegetation cover and climate statistics, as well as parameters that were more time- and work-intensive, such as joint plane and block statistics. I separated the analyses between parameters that varied along a portion of scarp, those that varied along a whole scarp, those that varied between scarps in the same region and those that varied between regions. At the scale of a scarp portion, I used Structure-from-Motion photogrammetry to create a digital outcrop model of a 200-m portion of the Nydri-Mosadalagja scarp (Figure 5.6). I used the CAD software Rhinoceros to manually map the extents of in situ joint-bounded blocks onto the three-dimensional model (Figure 5.6), using a field-validated method developed by Jacyn Schmidt for her undergraduate thesis at Carleton College. From these 3D joint maps, I can extract a series of

metrics describing rock mass characteristics, such as vertical and horizontal joint spacings and exposed fracture plane area, strike and dip. I bin these measurements according to the step along which morphologic variability is calculated, so that each morphologic variability value is spatially associated to a bin of joint-bounded blocks and can be directly compared to its rock mass characteristics.

At the scale of a single scarp, I measure scarp height using the algorithm described in Brigham and Crider (2022). Scarp height serves as an indicator for both position along the scarp, gravitational potential of a block to fall, and cohesive strength of the rock mass at the scale of the scarp. I measure aspect using the System for Automated Geoscientific Analyses program (SAGA; Conrad et al., 2015). To assess the level of vegetation cover, I computed Huete et al.'s (2002) enhanced vegetation index, a spectral transformation of two bands of Landsat 8 data designed to allow reliable spatial comparisons of terrestrial photosynthetic activity and canopy structural variations between different regions.

At the scale of multiple scarps, I use maximum scarp height, variations in diurnal temperature, total vegetation cover percentage and mean annual precipitation as parameters to compare to regional mean morphologic variability.

5.3.3.6 Statistical methods to compare form to parameters

My goal in using statistical methods is to understand the relationship between morphometric variability (our measure of scarp form) and parameters that vary along the fault, in order to determine the factors that are highly correlated to scarp form at the scale of an individual scarp, a group of scarps at a single site, and between different sites. The structure and strength of these relationships informs how scarp form can be interpreted in a given context. Comparing morphologic variability to a single parameter involves simple measures of statistical correlation

such as the Pearson product-moment correlation coefficient, a measure of the strength of a linear association between variables.

However, I suspect based on field observations that scarp form is a result of a wide range of parameters, so understanding which parameters are highly correlated with morphologic variability and the relative strength of their relationship is necessary. In this study, I use principal component analysis (PCA) to identify patterns in our scarp data and express them in such a way to highlight their similarities and differences. I compute principal components that are uncorrelated, ordered by their significance (amount of variance explained), and can be related back to the original characteristics by looking back at their factor loadings. These loadings indicate what percentage of the variance in an original parameter is explained by a given principal component. To increase the interpretability of the loadings, I use a varimax rotation to rotate the orthogonal basis of the principal component space so that the absolute value of the loadings approaches either 1 or 0, allowing us to clarify the relationship between parameters and components by more specifically identifying the component upon which data load. Our goal in this analysis is to divide parameters into groups, by separating those parameters that correlate highly with specific components from those that correlate less strongly. I am particularly interested in identifying parameters that load strongly on the same component as morphologic variability.

I can also use dominance analysis to assess the relative importance of these parameters in predicting morphologic variability. Dominance analysis is a method used to compare the relative importance of predictors in multiple regression (Budescu, 1993). It does so by doing pairwise comparisons of all parameters in the model as they relate to morphologic variability and computing the R-squared values of all possible combinations of parameters with morphologic variability. A parameter is dominant over another only if its predictive ability exceeds the predictive ability of

the other parameter in all possible subset models (Azen & Budescu, 2003). Dominance analysis thus allows us to quantify the contribution of scarp and environmental parameters to morphologic variability.

5.4 RESULTS

5.4.1 Variables within a single scarp

I begin by investigating the drivers of morphologic variability laterally along a scarp, first by using data derived from an SfM model on a small portion of a single scarp, then by looking at remotely sensed data that can be computed for the entire length of all the scarps in the study.

Manual joint surface mapping onto a three-dimensional digital surface model of Nydri-Mosadalagja, a post-glacial fault scarp on the Reykjanes peninsula of Iceland, yields a rich dataset from which several aspects of the relationship of rock mass characteristics to scarp form can be tested. By comparing morphologic variability to measures of block size (e.g., horizontal and vertical joint spacing), I can determine if profile form changes with rock mass characteristics in jointed volcanic rock, and if so, what are the likely processes that account for that change (e.g., increased rockfall in more unstable areas). Simple patterns in joint spacing can also be tested, by calculating metrics such as the standard deviation or the range (difference between the maximum and minimum values) of both horizontal and vertical joint spacings in a block bin. By using the facing direction of the exposed joints, I can test whether exposure, and thus thermally related processes such as frost cracking or diurnal changes in temperature, have a meaningful effect on scarp form in this scenario. I find a moderately strong positive correlation between morphologic variability and the range in strikes of the block facets in the free face of the scarp, suggesting that scarp form changes with increased variation in the facing direction of vertical cooling joints (Table 5.1). This suggests that the wider the range of sub-vertical joint orientations, the more variable the

scarp morphology. I also found a strong negative correlation between the average strike of joint facets and morphologic variability, suggesting that local aspect is a contributor to scarp form in this area. In terms of block size, morphologic variability increases when block sizes decrease, both in width and in height (R = -0.45 for block height and R = - 0.40 for block width). Furthermore, there is a moderately strong negative correlation between the ranges in block widths and heights and morphologic variability. This suggests that uniformly small blocks, rather than a range of large and small blocks, leads to increased changes in profile form along Nydri-Mosadalagja.

Using remotely sensed data, I compute the pairwise correlations between morphologic variability and the single scarp specific parameters (profile height, aspect and vegetation cover as measured through the EVI) (Table 5.2). Pearson correlation coefficient values are relatively low ($r^2 < 0.3$), indicating that these three parameters are not sufficient to explain the variance found in the morphologic variability measurements. However, the type of correlation (negative or positive) and the relative amount of variance explained by the parameters by each scarp gives us an indication of the relationship of these variables to scarp form. In the case of all scarps except for Bishop Scarp 2, height explains the largest proportion of variance in morphologic variability out of all the parameters. The highest correlations between height and morphologic variability are for the Hilina Pali (23% of variance in morphologic variability explained by profile height), the Kau Desert Fault (21%) and the Kalanaokuaiki Pali E (18%). These correlations are negative, indicating that scarp form becomes less variable as profile height increases. This is the case for all scarps except Bishop Scarp 2 (very weak positive correlation), Nydri-Mosadalagja (weak positive correlation) and Sodulholagja (weak positive correlation). Aspect shows weak correlation with profile form across all scarps, with a maximum R value of 0.15 (2% of variance explained) for Gold Digger Pass Scarp. In terms of vegetation cover, Gildruholtsgja (8% of variance explained)

and the Hilina Pali (6% of variance explained) hold the highest correlation scores, where EVI is weakly positively correlated with morphologic variability, suggesting that increased vegetation cover is slightly associated with changes in in scarp profile form. Other scarps present weak negative correlations between EVI and morphologic variability, such as the Kalanaokuaiki Pali E (5% of variance explained) and Bishop Scarp 3 (4% of variance explained), suggesting that increased vegetation cover is slightly associated with decreased morphologic variability.

5.4.2 Variables across scarps

My analysis of correlations between morphologic variability and three parameters (height, aspect and EVI) show that I need more parameters to capture the variance of the scarps' morphologic variability and that different scarps have different relationships between morphologic variability and the parameters. In this section, I explore how the relationship between morphologic variability and scarp and environmental parameters changes between different scarps, first looking at how scarps vary at each location, then comparing all the scarps to one another.

I compute summary statistics of the parameters I analyzed at the scale of a single scarp for each scarp: mean morphologic variability, maximum scarp height, standard deviation of scarp height along the scarp, mean aspect and mean EVI. I also include a minimum scarp growth rate, calculated by dividing the maximum scarp height by the maximum age of fault initiation (based on cross-cutting relationships of the scarp with dated lava flows) and the total length of the fault zone.

I start by computing the pairwise correlations between morphologic variability and the parameters described above for the scarps at each site (Table 5.3). I exclude the two scarps from the Medicine Lake Volcano site, since this group has too few data points to extract any meaningful data. I find that mean morphologic variability has strong negative correlations with maximum

scarp height at every site (Hawai'i: 90% of variance in mean morphologic variability explained by maximum scarp height; Iceland: 66% of variance explained; Bishop: 60% of variance explained). Mean aspect has very weak correlations to mean morphologic variability at Bishop and Hawai'i, but has a strong positive correlation with morphologic variability in Iceland (56% of variance explained). Mean morphologic variability has a strong negative correlation with fault zone length for the Bishop sites (79% of variance explained), and a moderate negative correlation for the Hawai'i and Iceland sites (24% and 16% of variance explained, respectively). The Bishop sites also show a strong negative correlation between mean morphologic variability and the standard deviation of profile height. The Iceland sites show a weak negative correlation with the variance in profile height (10% of variance explained) and the Hawai'i sites show a weak positive correlation with the variance in profile height (14% of variance explained). All sites show negative correlations of varying degrees with EVI (58% of variance explained for Hawai'i, 36% for Bishop and 18% for Iceland.) Finally, Hawai'i and Iceland show strong negative correlations of the minimum scarp growth rate established at each scarp with mean morphologic variability (66% and 90%, respectively), whereas Bishop shows a moderate positive correlation (12% of variance explained).

To summarize these pairwise comparisons, mean morphologic variability in Bishop tends to decrease with increasing scarp height, fault zone length standard deviation of profile height and EVI, and increase moderately with increasing scarp growth rates. In Hawai'i, mean morphologic variability tends to decrease with increasing scarp height, EVI and scarp growth rate, as well as, to a lesser extent, fault zone length, and increase moderately with increasing standard deviations of profile height. The morphologic variability of Icelandic scarps decreases strongly with increasing scarp height and scarp growth rate, decreases moderately with increasing fault zone

length, EVI and standard deviations of profile height, and increases moderately with increasing aspect. All sites have negative correlations between morphologic variability and maximum scarp height, fault zone length and EVI, but the correlation type varies between sites for the other parameters.

To understand how morphologic variability varies with the parameters at all of the sites at once, I use PCA on our data matrix to look at how the parameters vary with the principal components of variance, rather than looking at the correlations of pairwise comparisons of morphologic variability and a parameter for each scarp. I find that three principal components describe 86% of the variance in our dataset (Figure 5.7). I compute the component loadings of each of the parameters, which correspond to the Pearson correlations of the parameters with the components (Table 5.4). By using a varimax rotation, I maximize the variance between our loadings, obtaining a set of weights varying between -1 and 1 and increase our ability to interpret which parameters load strongly onto which components (Table 5.5). I establish a cutoff value of 0.75 to consider a loading to be strong, based on Tabachnick & Fidell's (2001) recommendations for interpreting significance from smaller datasets. I find that the parameters that load most strongly onto PC1 (which accounts for 35% of the variance in the scarp data) are maximum height and fault zone length. These fault-scale geometric parameters are thus most important in differentiating between different scarps, and are positively inter-related (i.e., increasing fault zone lengths are correlated with increasing maximum scarp heights). PC2 explains 30% of the variance in the dataset and the parameters that load most strongly onto it are mean morphologic variability (negative loading) and mean EVI (positive loading). This demonstrates that the shared variance between mean morphologic variability and mean EVI is important in differentiating between scarps and that, given this set of fault scarps, morphologic variability tends to be most strongly

related to vegetation cover. The difference in loading signs suggests that morphologic variability decreases with increasing vegetation cover.

In my final analysis, I look at parameters that vary between sites, but are the same for scarps in a given location. Our site-specific parameters are: annual cumulative precipitation (mm), average diurnal change in temperature (°C), estimated volcanic effusion rate during last known eruption (m/s), mean aspect (degrees), regional extension rates (mm/year), mean fault zone length of scarps in site (m), estimated age of last known scarp growth event (years), mean standard deviation of scarp heights, maximum temperature recorded in 2020, minimum temperature recorded in 2020, mean temperature recorded in 2020, mean EVI, maximum possible age of scarp initiation, minimum rate of scarp growth and mean of scarp mean morphologic variability. Given the large number of parameters and the low number of samples, I decide to use dominance analysis to assess the relative contributions of each variable to the mean morphologic variability of each site. Figure 5.8 presents the percentages of relative importance each parameter has to morphologic variability, which represents the percentage of incremental R-squared values calculated for each possible combination of parameters. I see that the mean temperature of the site and the mean EVI cover are the two most important features in explaining variations in morphologic variability between sites, suggesting that in this dataset, differences in scarp form between sites are influenced by vegetation cover and temperature-dependent processes. This is supported by the next two parameters that are important to morphologic variability: minimum annual temperature and differences in diurnal temperatures. The age of the last scarp growth event is the first listed age-related metric at 5.8% relative importance. This suggests that site-averaged scarp form primarily records geomorphic and biologic processes, rather than morphologic age.

5.5 Discussion and conclusion

This study applies three statistical techniques at four different scales to probe which methods can inform how morphology is related to a set of scarp parameters. At the scale of a single scarp, I use pairwise correlation calculations between morphologic variability and values of scarp parameters taken at the same resolution as the morphologic variability. I find that, given the granularity of the measurements that can be gleaned from high-resolution raster datasets and the high amount of variance inherent in a natural system, correlations tend to be weak. Future work at this scale should explore the resolution of parameter measurements along a scarp at which noise is reduced and signal is preserved. In the case of morphologic variability, fine-tuning a window size in which to determine class numbers and proportions relative to the resolution of the dataset and the scale of the features of interest is an essential next step to be able to make meaningful pairwise comparisons. Using the method of pairwise comparisons, I did establish that the relationship between scarp parameters and morphologic variability at one scarp can be different at another, even within the same site. For example, variations in form correlated negatively to profile height in many scarps, but this relationship was far from universal.

To consider the scarp scale, I computed summary statistics of the parameters measured along the scarp's length (e.g., mean variability, maximum scarp height). I used two approaches to examine relationships between parameters: pairwise comparisons of parameters at a single site and principal component analysis to determine the drivers of variance across all sites. The first approach allows us to compare possible drivers of scarp form between different sites, whereas the second gives a better understanding of the broader relationship of the parameters to one another across sites. I find that fault structure attributes (scarp height and fault length), which also hint at rock mass characteristics, differentiate between scarps the most, but that morphologic variability

and mean EVI account for a significant proportion of variance in the data and are inter-related. This emphasizes the need to observes scarps forms in a variety of climates to captures the possible variations in evolutionary paths of fault scarps in jointed volcanic rock.

At the scale of different sites containing multiple scarps, I use dominance analysis to inform how parameters might relate to changes in scarp form. This analysis allows us to see how parameters are inter-related and how important they are to predicting morphologic variability. I find that the most important parameters relate to vegetation cover and temperature, suggesting that differences in morphologic variability between sites might be related to geomorphic and biologic processes. This implies that more data at sites with differing climates and vegetation profiles is necessary in order to isolate how scarp form evolves through time.

This study serves as a guide on how morphologic variability can be used to glean different types of information at different scales from scarp forms. To be able to make any claims of morphometric dating of fault scarps in jointed bedrock, much more data is needed to feed these statistical models, in terms of types of parameters (e.g., parameters that can only be measured in the field, such as rock strength), of total number of scarps studied and of scarp settings.

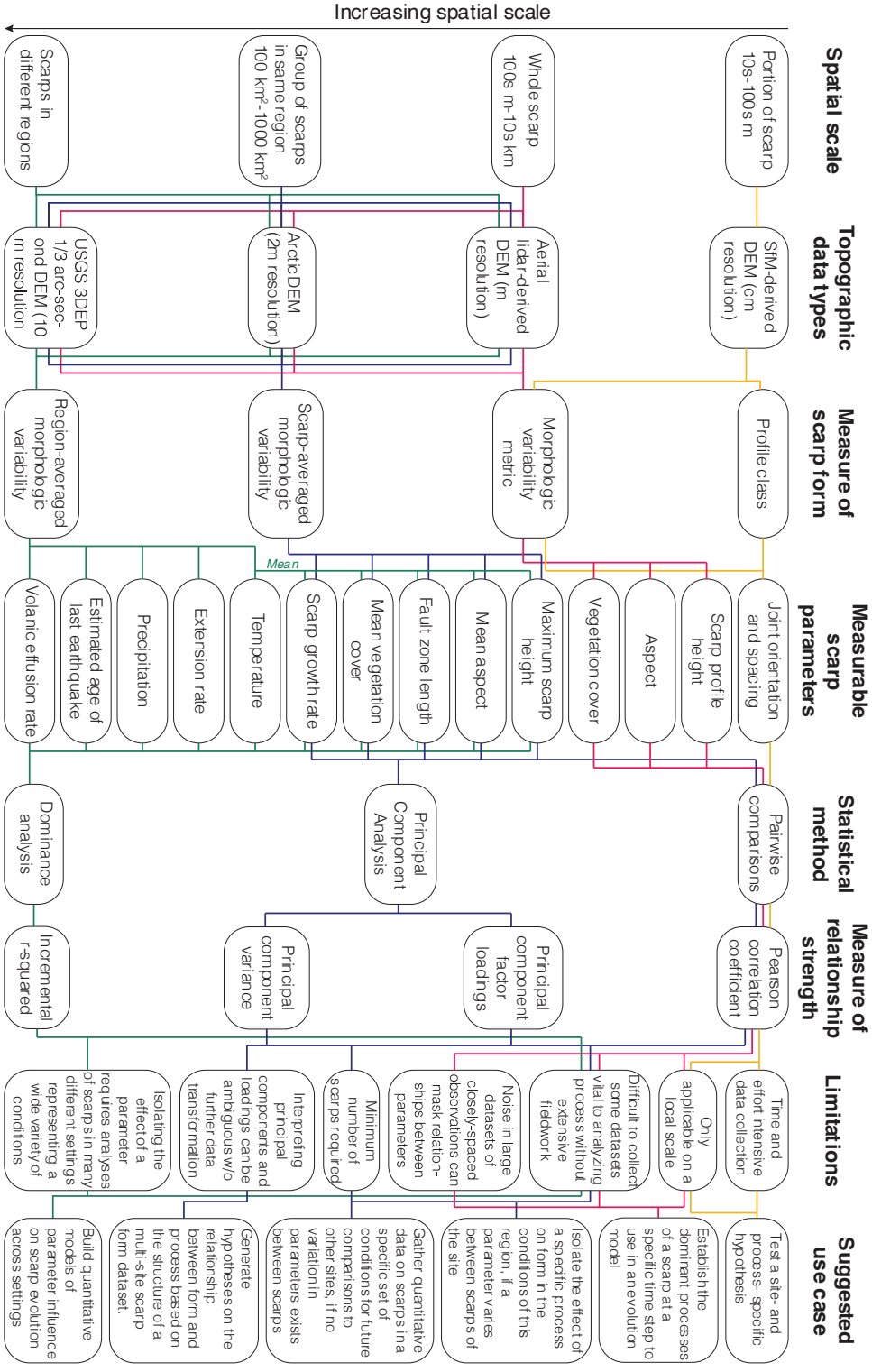

Figure 5.1. Flow chart indicating types of parameters and methods used in study based on spatial scale of analysis, and resulting suggestions for use cases.

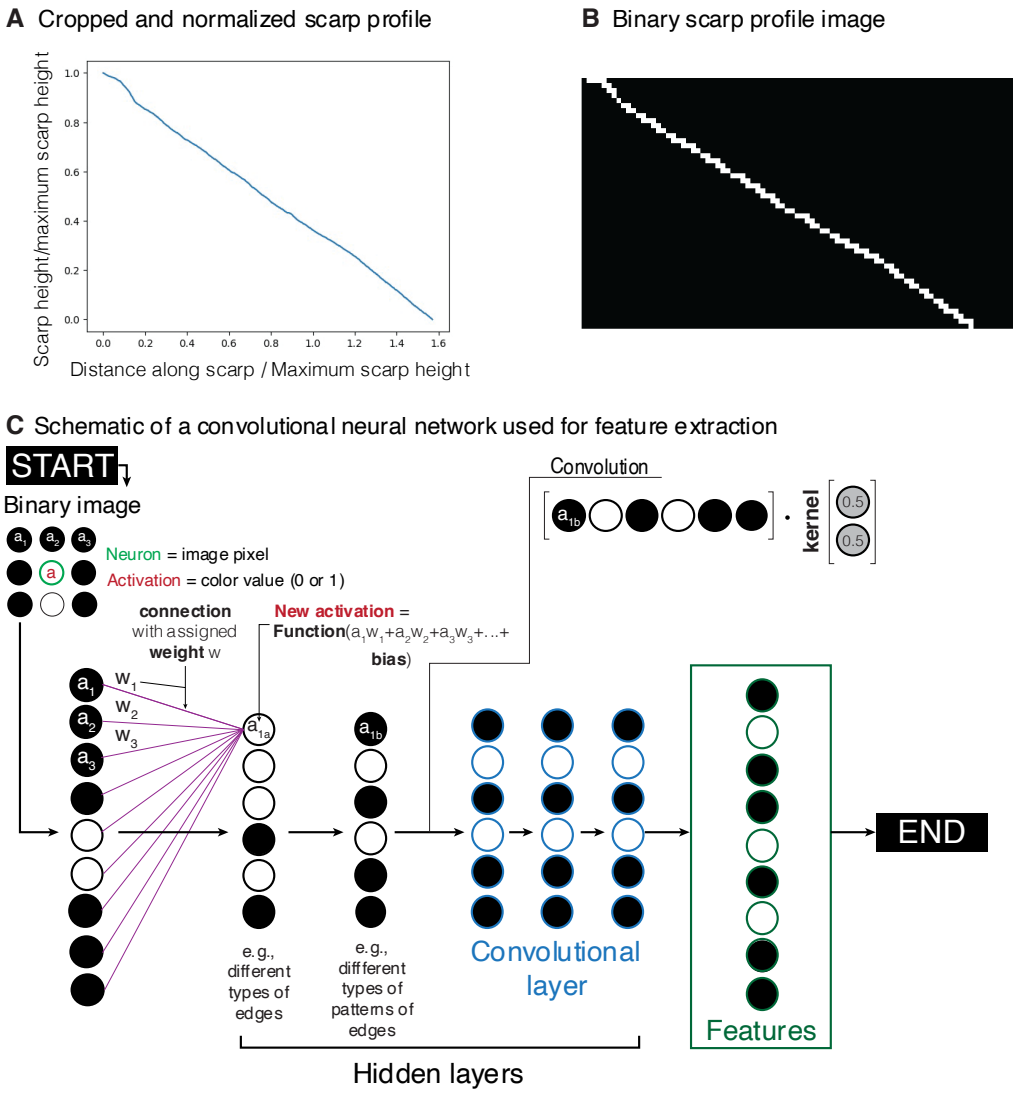

Figure 5.2. A. Scarp normal profile taken from the Hilina Pali, cropped to section between scarp crest and toe and normalized by profile height. B. Binary image of the same Hilina Pali profile. C. Schematic illustration of a neural network with both fully connected and convolutional layers used for feature extraction. D. Illustration of the VGG16 model.

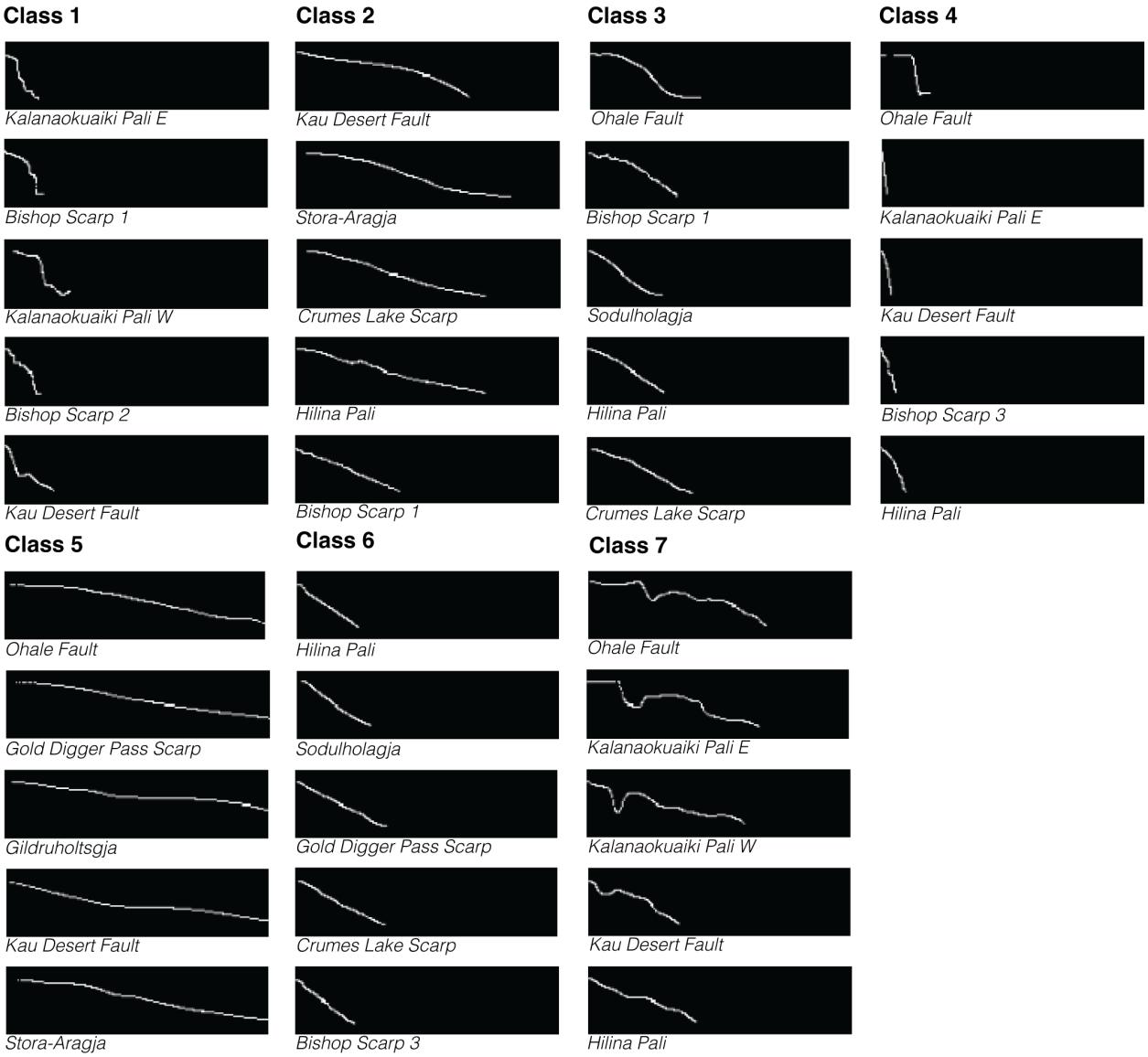

Figure 5.3. The seven morphologic classes determined by k-means clustering, as represented by 5 examples per class of cropped and normalized binary profile images from the studied scarps.

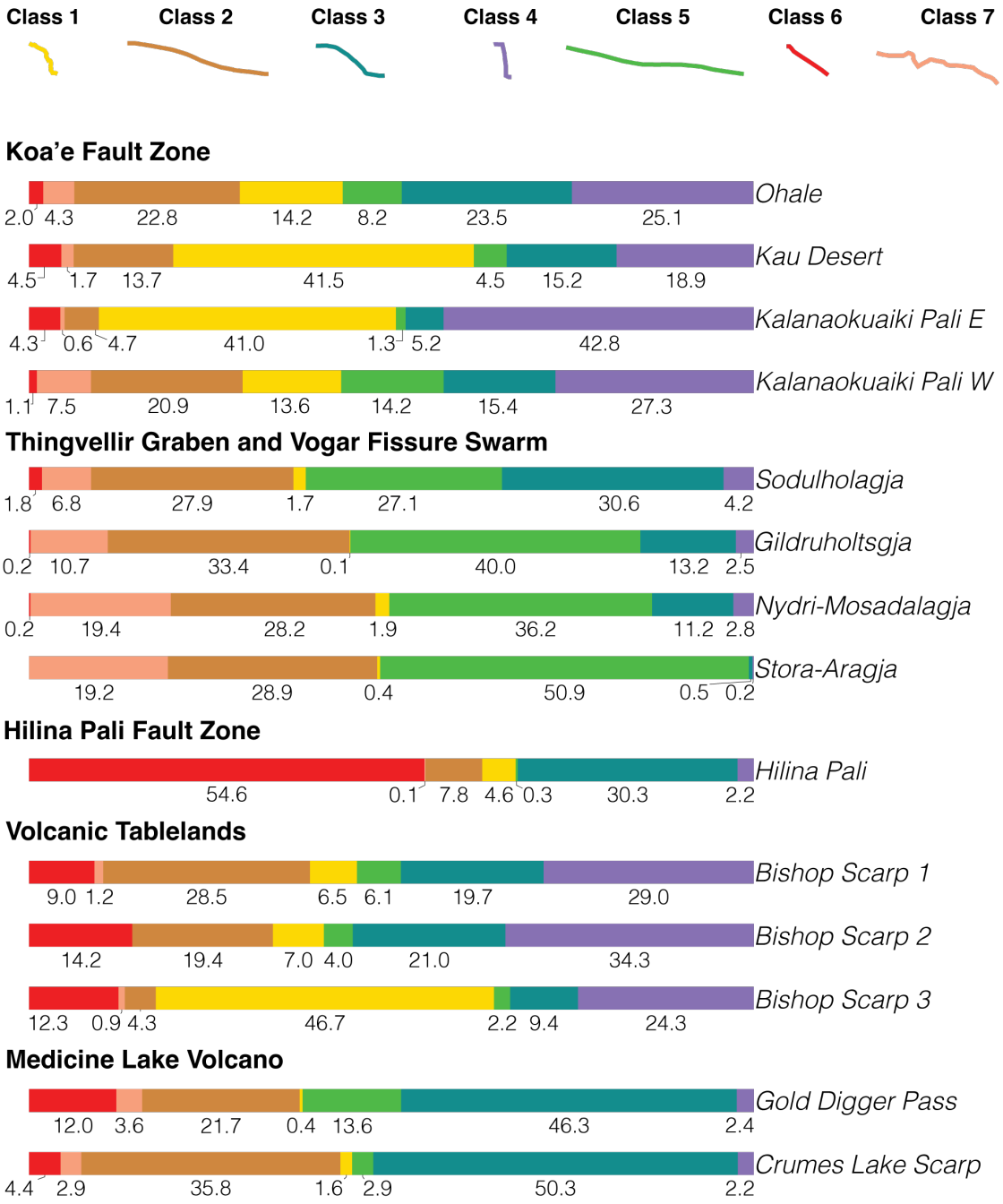

Figure 5.4. Horizontal bar plots representing the relative proportion of profiles of a given morphologic class for the fourteen scarps in the study. The seven morphologic classes are represented at the top of the page. Numbers beneath barplots indicate percentage of scarp profiles belonging to that class. Scarps are grouped by region.

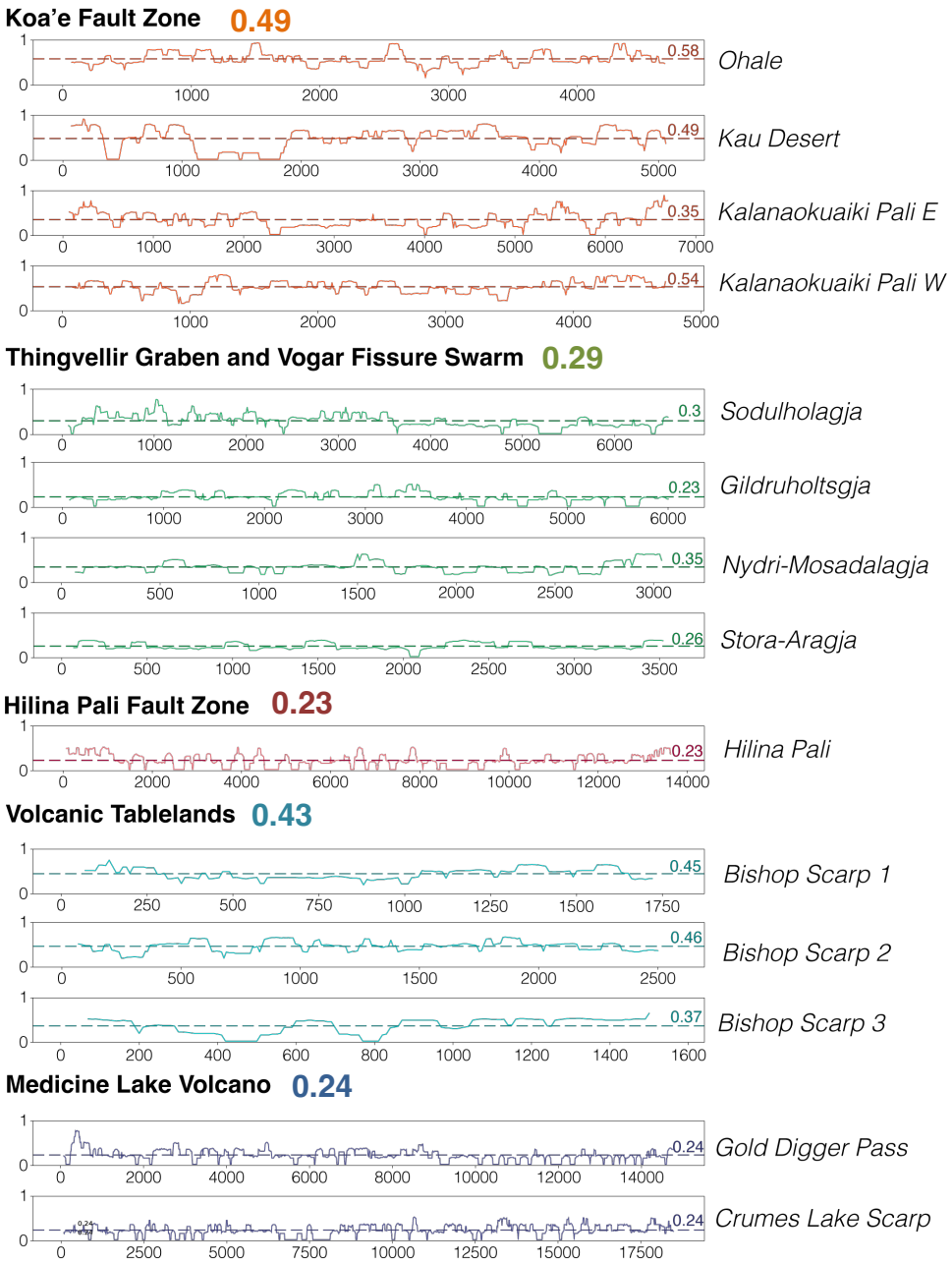

Figure 5.5. Morphometric variability values calculated along strike of each of the studied scarps. X-axis for all plots indicates distance along the scarp in meters, the Y axis indicates the morphologic variability value, which is dimensionless and varies between 0 and 1. The dashed line and associated number indicated the mean morphologic variability value calculated for the scarp. The number by the regional name indicates the regional mean morphologic variability number.

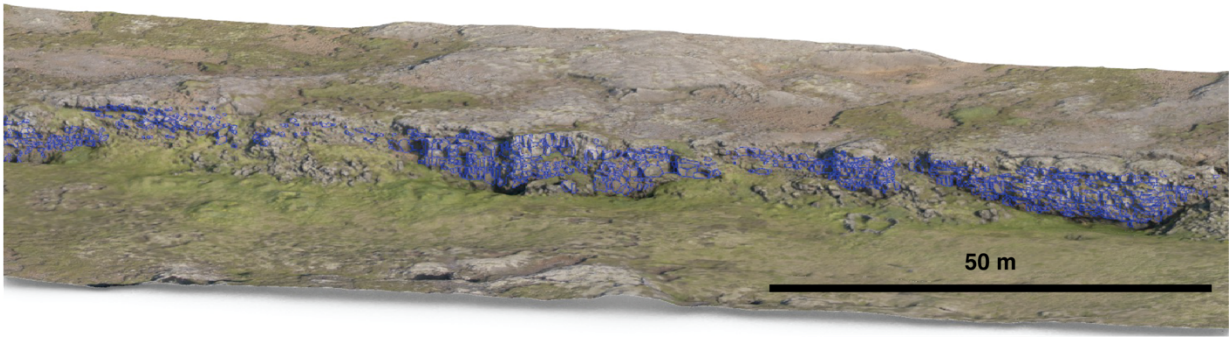

Figure 5.6. Facets (delimited by blue lines) of joint-bounded blocks contained in free face of Nydri-Mosadalagja mapped onto 3-D digital model

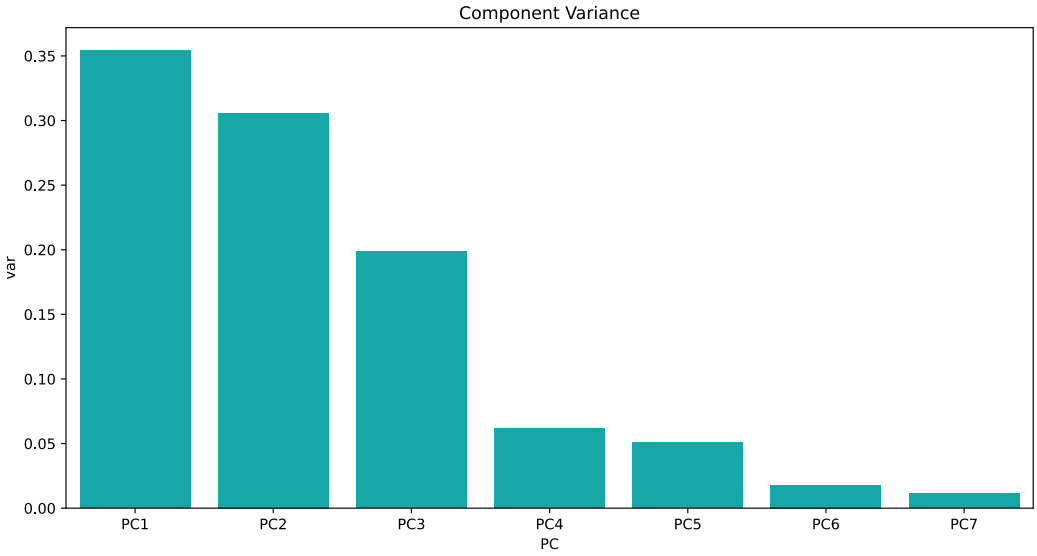

Figure 5.7. Scree plot of the proportion of dataset variance explained by the principal components

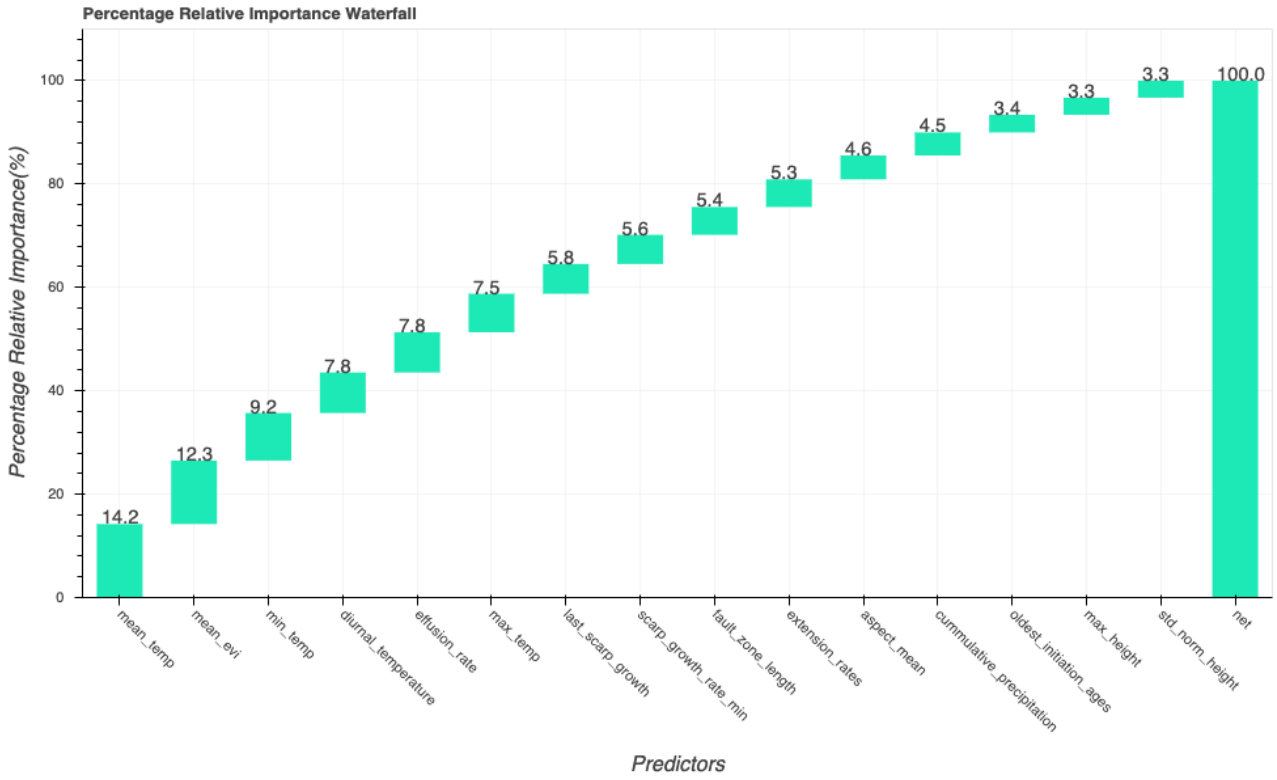

Figure 5.8. Percentages of relative importance of the scarp and environmental parameters in predicting values of morphologic variability

Table 5.1: Pearson correlation coefficients (r values) resulting from pairwise comparisons of morphologic variability values and parameters relating to rock mass characteristics of a section of the Nydri-Mosadalagja scarp.

Mean facet strike	**Facet strike range**	**Max spacing (vertical joints)**	**Max spacing (horizontal joints)**	**Spacing range (vertical joints)**	**Spacing range (horizontal joints)**	**Mean facet dip**	**Min facet dip**
-0.64	**0.49**	**-0.40**	**-0.45**	**-0.45**	**-0.50**	0.19	0.32

Table 5.2. Pairwise correlations (r values) of along-scarp morphologic variability and scarp parameters

Scarp	Height	Aspect	Vegetation cover (EVI)
Kau Desert	**-0.46**	**-0.14**	0.17
Kalanaokuaiki Pali E	**-0.42**	-0.1	**-0.22**
Ohale	-0.34	0.02	-0.05
Hilina Pali	**-0.47**	-0.0	**0.24**
Kalanaokuaiki Pali W	-0.33	0.03	-0.14
Bishop Scarp 1A	-0.21	-0.1	-0.04
Bishop Scarp 1B	-0.29	0.07	0.06
Bishop Scarp 2A	-0.07	-0.01	0.04
Bishop Scarp 2B	0.01	0.05	-0.15
Bishop Scarp3	-0.24	0.00	-0.21
Stora-Aragja	-0.12	-0.04	-0.04
Nydri-Mosadalagja	0.18	**-0.14**	-0.05
Sodulholagja	0.16	-0.02	-0.2
Gildruholtsgja	-0.28	-0.01	**0.28**
Gold Digger Pass Scarp	0.01	**0.15**	-0.2
Crumes Lake Scarp	-0.15	-0.05	-0.15

Table 5.3. Pairwise correlations (r values) of along-scarp morphologic variability and whole-scarp-scale scarp and environmental parameters

Region	**Max scarp height**	**Mean aspect**	**Fault zone length**	**Standard deviation of profile height**	**Mean vegetation cover (EVI)**	**Min scarp growth rate.**
Bishop	-0.78	-0.08	-0.89	-0.86	-0.6	0.35
Hawai'i	-0.81	-0.01	-0.49	0.37	-0.76	-0.81
Iceland	-0.95	0.75	-0.4	-0.31	-0.43	-0.95

Table 5.4. Loadings of whole-scarp-scale scarp and environmental parameters onto principal components (PCs.)

Parameter	PC1	PC2	PC3
Mean aspect	-0.64	0.65	-0.02
Fault zone length	**0.92**	0.07	0.09
Standard deviation of profile heights	0.59	-0.02	**-0.80**
Maximum scarp heights	**0.88**	-0.05	0.27
Mean EVI	-0.02	**0.94**	0.26
Minimum scarp growth rate	-0.0	-0.58	**0.79**
Mean morphologic variability	-0.53	**-0.80**	-0.28

Table 5.5. Varimax-rotated loadings of whole-scarp-scale scarp and environmental parameters onto principal components

Parameter	PC1	PC2	PC3
Mean aspect	-0.74	0.53	-0.03
Fault zone length	**0.88**	0.20	-0.17
Standard deviation of profile heights	0.40	-0.19	**-0.89**
Maximum scarp heights	**0.91**	0.14	0.04
Mean EVI	-0.14	**0.96**	-0.01
Minimum scarp growth rate	0.27	-0.31	**0.89**
Mean morphologic variability	-0.42	**-0.90**	0.10

BIBLIOGRAPHY

Abellán, A., Vilaplana, J. M., Calvet, J., García-Sellés, D., & Asensio, E. (2011). Rockfall monitoring by Terrestrial Laser Scanning – case study of the basaltic rock face at Castellfollit de la Roca (Catalonia, Spain). *Natural Hazards and Earth System Sciences*, *11*(3), 829–841. https://doi.org/10.5194/nhess-11-829-2011

Abellán, Antonio, Calvet, J., Vilaplana, J. M., & Blanchard, J. (2010). Detection and spatial prediction of rockfalls by means of terrestrial laser scanner monitoring. *Geomorphology*, *119*(3), 162–171. https://doi.org/10.1016/j.geomorph.2010.03.016

Acocella, V., Gudmundsson, A., & Funiciello, R. (2000). Interaction and linkage of extension fractures and normal faults: examples from the rift zone of Iceland. *Journal of Structural Geology*, *22*(9), 1233–1246. https://doi.org/10.1016/S0191-8141(00)00031-6

Anderson, S. P. (2019). Breaking it Down: Mechanical Processes in the Weathering Engine. *Elements*, *15*(4), 247–252. https://doi.org/10.2138/gselements.15.4.247

Andrews, D. J., & Hanks, T. C. (1985). Scarp degraded by linear diffusion: Inverse solution for age. *Journal of Geophysical Research*, *90*(B12), 10193. https://doi.org/10.1029/JB090iB12p10193

Árnadóttir, T., Geirsson, H., & Jiang, W. (2008). Crustal deformation in Iceland: Plate spreading and earthquake deformation. *Jökull*, *58*, 59–74.

Arnalds, O. (2004). Volcanic soils of Iceland. *CATENA*, *56*(1–3), 3–20. https://doi.org/10.1016/j.catena.2003.10.002

Avouac, J.-P. (1993). Analysis of scarp profiles: Evaluation of errors in morphologic dating. *Journal of Geophysical Research: Solid Earth*, *98*(B4), 6745–6754. https://doi.org/10.1029/92JB01962

Ayenew, T., & Barbieri, G. (2005). Inventory of landslides and susceptibility mapping in the Dessie area, northern Ethiopia. *Engineering Geology*, *77*(1–2), 1–15. https://doi.org/10.1016/j.enggeo.2004.07.002

Ayonghe, S. N., Mafany, G. T., Ntasin, E., & Samalang, P. (1999). Seismically Activated Swarm of Landslides, Tension Cracks, and a Rockfall after Heavy Rainfall in Bafaka, Cameroon. *Natural Hazards*, *19*(1), 13–27. https://doi.org/10.1023/A:1008041205256

Azen, R., & Budescu, D. V. (2003). The dominance analysis approach for comparing predictors in multiple regression. *Psychological Methods*, *8*(2), 129–148. https://doi.org/10.1037/1082-989X.8.2.129

Bachman, S. B. (1978). Pliocene-Pleistocene break-up of the Sierra Nevada–White-Inyo Mountains block and formation of Owens Valley. *Geology*, *6*(8), 461–463. https://doi.org/10.1130/0091-7613(1978)6<461:PBOTSN>2.0.CO;2

Bacon, C. R., & Robinson, J. E. (2019). Postglacial faulting near Crater Lake, Oregon, and its possible association with the Mazama caldera-forming eruption. *GSA Bulletin*, *131*(9–10), 1440–1458. https://doi.org/10.1130/B35013.1

Banks, M. E., Xiao, Z., Watters, T. R., Strom, R. G., Braden, S. E., Chapman, C. R., et al. (2015). Duration of activity on lobate-scarp thrust faults on Mercury. *Journal of Geophysical Research: Planets*, *120*(11), 1751–1762. https://doi.org/10.1002/2015JE004828

Bateman, P. C., Pakiser, L. C., & Kane, M. F. (1965). *Geology and tungsten mineralization of the Bishop district, California, with a section on gravity study of Owens Valley and a*

section on seismic profile (U.S. Geological Survey Professional Paper No. 470). *Professional Paper*. U. S. Govt. Print. Off.,. https://doi.org/10.3133/pp470

Beechie, T., & Imaki, H. (2014). Predicting natural channel patterns based on landscape and geomorphic controls in the Columbia River basin, USA: Predicting Channel Patterns in the Columbia Basin. *Water Resources Research*, *50*(1), 39–57. https://doi.org/10.1002/2013WR013629

Bell, J. W. (1981). *Quaternary fault map of the Reno 1° x 2° quadrangle* (No. 81–982). *Open-File Report*. U.S. Geological Survey,. https://doi.org/10.3133/ofr81982

Bell, J. W., & Katzer, T. (1990). Timing of late Quaternary faulting in the 1954 Dixie Valley earthquake area, central Nevada. *Geology*, *18*(7), 622. https://doi.org/10.1130/0091-7613(1990)018<0622:TOLQFI>2.3.CO;2

Bell, J. W., Caskey, S. J., Ramelli, A. R., & Guerrieri, L. (2004). Pattern and Rates of Faulting in the Central Nevada Seismic Belt, and Paleoseismic Evidence for Prior Beltlike Behavior. *Bulletin of the Seismological Society of America*, *94*(4), 1229–1254. https://doi.org/10.1785/012003226

Berner, R. A., & Cochran, M. F. (1998). Plant-induced weathering of Hawaiian basalts. *Journal of Sedimentary Research*, *68*(5), 723–726. https://doi.org/10.2110/jsr.68.723

Bingol, O. R., & Krishnamurthy, A. (2019). NURBS-Python: An open-source object-oriented NURBS modeling framework in Python. *SoftwareX*, *9*, 85–94. https://doi.org/10.1016/j.softx.2018.12.005

Bishop, C. M. (2016). *Pattern Recognition and Machine Learning* (Softcover reprint of the original 1st edition 2006 (corrected at 8th printing 2009)). New York, NY: Springer New York.

Bitencourt, V. J. B., & Dillenburg, S. R. (2020). Application of multivariate statistical techniques in alongshore differentiation of coastal barriers. *Marine Geology*, *419*, 106077. https://doi.org/10.1016/j.margeo.2019.106077

Blakeslee, M. W., & Kattenhorn, S. A. (2013). Revised earthquake hazard of the Hat Creek fault, northern California: A case example of a normal fault dissecting variable-age basaltic lavas. *Geosphere*, *9*(5), 1397–1409. https://doi.org/10.1130/GES00910.1

Boser, B. E., Guyon, I. M., & Vapnik, V. N. (1992). A training algorithm for optimal margin classifiers. In *Proceedings of the fifth annual workshop on Computational learning theory* (pp. 144–152). Pittsburgh Pennsylvania USA: ACM. https://doi.org/10.1145/130385.130401

Brigham, C. A. P., & Crider, J. G. (2022). A new metric for morphologic variability using landform shape classification via supervised machine learning. *Geomorphology*, *399*, 108065. https://doi.org/10.1016/j.geomorph.2021.108065

Brooks, B. A., Foster, J. H., Bevis, M., Frazer, L. N., Wolfe, C. J., & Behn, M. (2006). Periodic slow earthquakes on the flank of Kīlauea volcano, Hawai'i. *Earth and Planetary Science Letters*, *246*(3), 207–216. https://doi.org/10.1016/j.epsl.2006.03.035

Brown, D. G., Lusch, D. P., & Duda, K. A. (1998). Supervised classification of types of glaciated landscapes using digital elevation data. *Geomorphology*, *21*(3–4), 233–250. https://doi.org/10.1016/S0169-555X(97)00063-9

Bubeck, A., Walker, R. J., Imber, J., & MacLeod, C. J. (2018). Normal fault growth in layered basaltic rocks: The role of strain rate in fault evolution. *Journal of Structural Geology*, *115*, 103–120. https://doi.org/10.1016/j.jsg.2018.07.017

Bucknam, R. C., & Anderson, R. E. (1979). Estimation of fault-scarp ages from a scarp-height–slope-angle relationship. *Geology*, *7*(1), 11. https://doi.org/10.1130/0091-7613(1979)7<11:EOFAFA>2.0.CO;2

Budescu, D. V. (1993). Dominance analysis: A new approach to the problem of relative importance of predictors in multiple regression. *Psychological Bulletin*, *114*(3), 542–551. https://doi.org/10.1037/0033-2909.114.3.542

Burford, E. P., Fomina, M., & Gadd, G. M. (2003). Fungal involvement in bioweathering and biotransformation of rocks and minerals. *Mineralogical Magazine*, *67*(6), 1127–1155. https://doi.org/10.1180/0026461036760154

Callahan, O. A., Brigham, C. A. P., Heitmann, E., Sullivan, E., Jackson, A., Mat, S. R., et al. (2023). DEMs and Orthomosaics of Hydrothermal Sites in the Central NV Seismic Belt. In *Proceedings – 48th Workshop on Geothermal Reservoir Engineering*. OpenTopography. https://doi.org/10.5069/G9P26WBB

Castillo, C., Taguas, E. V., Zarco-Tejada, P., James, M. R., & Gómez, J. A. (2014). The normalized topographic method: an automated procedure for gully mapping using GIS: THE NORMALIZED TOPOGRAPHIC METHOD. *Earth Surface Processes and Landforms*, *39*(15), 2002–2015. https://doi.org/10.1002/esp.3595

Chen, K., Smith, J. D., Avouac, J.-P., Liu, Z., Song, Y. T., & Gualandi, A. (2019). Triggering of the Mw 7.2 Hawaii Earthquake of 4 May 2018 by a Dike Intrusion. *Geophysical Research Letters*, *46*(5), 2503–2510. https://doi.org/10.1029/2018GL081428

Clarke, B. A., & Burbank, D. W. (2010). Bedrock fracturing, threshold hillslopes, and limits to the magnitude of bedrock landslides. *Earth and Planetary Science Letters*, *297*(3–4), 577–586. https://doi.org/10.1016/j.epsl.2010.07.011

Collins, B. D., & Stock, G. M. (2016). Rockfall triggering by cyclic thermal stressing of exfoliation fractures. *Nature Geoscience*, *9*(5), 395–400. https://doi.org/10.1038/ngeo2686

Conrad, O., Bechtel, B., Bock, M., Dietrich, H., Fischer, E., Gerlitz, L., et al. (2015). System for Automated Geoscientific Analyses (SAGA) v. 2.1.4. *Geoscientific Model Development*, *8*(7), 1991–2007. https://doi.org/10.5194/gmd-8-1991-2015

Cowie, P. A., & Scholz, C. H. (1992). Displacement-length scaling relationship for faults: data synthesis and discussion. *Journal of Structural Geology*, *14*(10), 1149–1156. https://doi.org/10.1016/0191-8141(92)90066-6

Crider, J. G. (2001). Oblique slip and the geometry of normal-fault linkage: mechanics and a case study from the Basin and Range in Oregon. *Journal of Structural Geology*, *23*(12), 1997–2009. https://doi.org/10.1016/S0191-8141(01)00047-5

Crider, J. G. (2008). Simulating fault scarp degradation in jointed bedrock. Presented at the European Geosciences Union General Assembly, Vienna, Austria.

Crider, J. G., & Pollard, D. D. (1998). Fault linkage: Three-dimensional mechanical interaction between echelon normal faults. *Journal of Geophysical Research: Solid Earth*, *103*(B10), 24373–24391. https://doi.org/10.1029/98JB01353

Curry, A. M., & Morris, C. J. (2004). Lateglacial and Holocene talus slope development and rockwall retreat on Mynydd Du, UK. *Geomorphology*, *58*(1), 85–106. https://doi.org/10.1016/S0169-555X(03)00226-5

D'Amato, J., Hantz, D., Guerin, A., Jaboyedoff, M., Baillet, L., & Mariscal, A. (2016). Influence of meteorological factors on rockfall occurrence in a middle mountain limestone cliff.

Natural Hazards and Earth System Sciences, *16*(3), 719–735. https://doi.org/10.5194/nhess-16-719-2016

Dawers, N. H., & Anders, M. H. (1995). Displacement-length scaling and fault linkage. *Journal of Structural Geology*, *17*(5), 607–614. https://doi.org/10.1016/0191-8141(94)00091-D

Dawers, N. H., Anders, M. H., & Scholz, C. H. (1993). Growth of normal faults: Displacement-length scaling. *Geology*, *21*(12), 1107–1110. https://doi.org/10.1130/0091-7613(1993)021<1107:GONFDL>2.3.CO;2

De Blasio, F. V., & Sæter, M.-B. (2009). Small-scale experimental simulation of talus evolution. *Earth Surface Processes and Landforms*, *34*(12), 1685–1692. https://doi.org/10.1002/esp.1861

De Boer, D. H. (1992). Hierarchies and spatial scale in process geomorphology: a review. *Geomorphology*, *4*(5), 303–318. https://doi.org/10.1016/0169-555X(92)90026-K

Degraff, J. M., & Aydin, A. (1987). Surface morphology of columnar joints and its significance to mechanics and direction of joint growth. *GSA Bulletin*, *99*(5), 605–617. https://doi.org/10.1130/0016-7606(1987)99<605:SMOCJA>2.0.CO;2

Degraff, J. M., & Aydin, A. (1993). Effect of thermal regime on growth increment and spacing of contraction joints in basaltic lava. *Journal of Geophysical Research: Solid Earth*, *98*(B4), 6411–6430. https://doi.org/10.1029/92JB01709

Delaney, P. T., Denlinger, R. P., Lisowski, M., Miklius, A., Okubo, P. G., Okamura, A. T., & Sako, M. K. (1998). Volcanic spreading at Kilauea, 1976–1996. *Journal of Geophysical Research: Solid Earth*, *103*(B8), 18003–18023. https://doi.org/10.1029/98JB01665

DeLong, S. B., Hilley, G. E., Rymer, M. J., & Prentice, C. (2010). Fault zone structure from topography: Signatures of en echelon fault slip at Mustang Ridge on the San Andreas Fault, Monterey County, California. *Tectonics*, *29*(5), n/a-n/a. https://doi.org/10.1029/2010TC002673

DiBiase, R. A., Rossi, M. W., & Neely, A. B. (2018). Fracture density and grain size controls on the relief structure of bedrock landscapes. *Geology*, *46*(5), 399–402. https://doi.org/10.1130/G40006.1

Dietze, M., Turowski, J. M., Cook, K. L., & Hovius, N. (2017). Spatiotemporal patterns, triggers and anatomies of seismically detected rockfalls. *Earth Surface Dynamics*, *5*(4), 757–779. https://doi.org/10.5194/esurf-5-757-2017

Dikau, R., Brabb, E. E., & Mark, R. M. (1991). *Landform classification of New Mexico by computer* (No. 91–634). U.S. Dept. of the Interior, U.S. Geological Survey,. https://doi.org/10.3133/ofr91634

Donnelly-Nolan, J. M. (2010). *Geologic map of Medicine Lake volcano, northern California: U.S. Geological Survey Scientific Investigations Map 2927* (Pamphlet No. 2927) (p. 48). Retrieved from https://pubs.usgs.gov/sim/2927/

Donnelly-Nolan, J. M., Nathenson, M., Champion, D. E., Ramsey, D. W., Lowenstern, J. B., & Ewert, J. W. (2007). *Volcano Hazards Assessment for Medicine Lake Volcano, Northern California* (USGS Numbered Series No. 2007-5174- A). *Volcano Hazards Assessment for Medicine Lake Volcano, Northern California* (Vol. 2007-5174-A). Geological Survey (U.S.). https://doi.org/10.3133/sir20075174A

Draebing, D., & Krautblatter, M. (2019). The Efficacy of Frost Weathering Processes in Alpine Rockwalls. *Geophysical Research Letters*, *46*(12), 6516–6524. https://doi.org/10.1029/2019GL081981

Drăguţ, L., & Blaschke, T. (2006). Automated classification of landform elements using object-based image analysis. *Geomorphology*, *81*(3–4), 330–344. https://doi.org/10.1016/j.geomorph.2006.04.013

Drăguţ, L., & Eisank, C. (2012). Automated object-based classification of topography from SRTM data. *Geomorphology*, *141–142*, 21–33. https://doi.org/10.1016/j.geomorph.2011.12.001

Dubey, A. K., & Jain, V. (2020). Automatic facial recognition using VGG16 based transfer learning model. *Journal of Information and Optimization Sciences*, *41*(7), 1589–1596. https://doi.org/10.1080/02522667.2020.1809126

Duffield, W. A. (1975). *Structure and origin of the Koae fault system, Kilauea volcano, Hawaii.* (U.S. Geological Survey Professional Paper No. 856).

Duraiswami, R. A., Dole, G., & Bondre, N. (2003). Slabby pahoehoe from the western Deccan Volcanic Province: evidence for incipient pahoehoe–aa transitions. *Journal of Volcanology and Geothermal Research*, *121*(3), 195–217. https://doi.org/10.1016/S0377-0273(02)00411-0

Duraiswami, R. A., Bondre, N. R., & Managave, S. (2008). Morphology of rubbly pahoehoe (simple) flows from the Deccan Volcanic Province: Implications for style of emplacement. *Journal of Volcanology and Geothermal Research*, *177*(4), 822–836. https://doi.org/10.1016/j.jvolgeores.2008.01.048

Duraiswami, R. A., Sheth, H., Gadpallu, P., Youbi, N., & Chellai, E. H. (2020). A simple recipe for red bole formation in continental flood basalt provinces: weathering of flow-top and flow-bottom breccias. *Arabian Journal of Geosciences*, *13*(18), 953. https://doi.org/10.1007/s12517-020-05973-9

Duvall, A. (2004). Tectonic and lithologic controls on bedrock channel profiles and processes in coastal California. *Journal of Geophysical Research*, *109*(F3), F03002. https://doi.org/10.1029/2003JF000086

Dyba, K., & Jasiewicz, J. (2022). Toward geomorphometry of plains - Country-level unsupervised classification of low-relief areas (Poland). *Geomorphology*, *413*, 108373. https://doi.org/10.1016/j.geomorph.2022.108373

Easton, R. M. (1987). Stratigraphy of Kilauea Volcano. In R. W. Decker, T. L. Wright, & P. H. Stauffer (Eds.), *Volcanism in Hawaii: U.S. Geological Survey Professional Paper 1350* (p. 1667). Retrieved from https://pubs.usgs.gov/pp/1987/1350/

Einarsson, M. Á. (1984). Climate of Iceland. In H. VanLoon (Ed.), *World Survey of Climatology: Climates of the oceans* (Vol. 15, pp. 673–697).

Einarsson, P. (1991). Earthquakes and present-day tectonism in Iceland. *Tectonophysics*, *189*(1), 261–279. https://doi.org/10.1016/0040-1951(91)90501-I

Einarsson, P. (2008). Plate boundaries, rifts and transforms in Iceland. *Jökull*, *58*(12), 35–58.

Eppes, M. C., Magi, B., Hallet, B., Delmelle, E., Mackenzie-Helnwein, P., Warren, K., & Swami, S. (2016). Deciphering the role of solar-induced thermal stresses in rock weathering. *GSA Bulletin*, *128*(9–10), 1315–1338. https://doi.org/10.1130/B31422.1

Eppes, M.-C., & Keanini, R. (2017). Mechanical weathering and rock erosion by climate-dependent subcritical cracking. *Reviews of Geophysics*, *55*(2), 470–508. https://doi.org/10.1002/2017RG000557

Evans, J. P., & Bradbury, K. K. (2004). Faulting and Fracturing of Nonwelded Bishop Tuff, Eastern California: Deformation Mechanisms in Very Porous Materials in the Vadose Zone. *Vadose Zone Journal*, *3*(2), 602–623. https://doi.org/10.2113/3.2.602

Ferrill, D. A., Wyrick, D. Y., & Smart, K. J. (2011). Coseismic, dilational-fault and extension-fracture related pit chain formation in Iceland: Analog for pit chains on Mars. *Lithosphere*, *3*(2), 133–142. https://doi.org/10.1130/L123.1

Ferrill, D. A., Morris, A. P., McGinnis, R. N., Smart, K. J., Watson-Morris, M. J., & Wigginton, S. S. (2016). Observations on normal-fault scarp morphology and fault system evolution of the Bishop Tuff in the Volcanic Tableland, Owens Valley, California, U.S.A. *Lithosphere*, *8*(3), 238–253. https://doi.org/10.1130/L476.1

Fiske, R. S., & Koyanagi, R. Y. (1968). *The December 1965 eruption of Kilauea Volcano, Hawaii* (Professional Paper No. 607) (p. 21).

Fityus, S. G., Giacomini, A., & Buzzi, O. (2013). The significance of geology for the morphology of potentially unstable rocks. *Engineering Geology*, *162*, 43–52. https://doi.org/10.1016/j.enggeo.2013.05.007

Fletcher, R. C., Buss, H. L., & Brantley, S. L. (2006). A spheroidal weathering model coupling porewater chemistry to soil thicknesses during steady-state denudation. *Earth and Planetary Science Letters*, *244*(1), 444–457. https://doi.org/10.1016/j.epsl.2006.01.055

Forslund, T., & Gudmundsson, A. (1991). Crustal spreading due to dikes and faults in southwest Iceland. *Journal of Structural Geology*, *13*(4), 443–457. https://doi.org/10.1016/0191-8141(91)90017-D

de Freitas, M. H., & Watters, R. J. (1973). Some field examples of toppling failure. *Géotechnique*, *23*(4), 495–513. https://doi.org/10.1680/geot.1973.23.4.495

Gabet, E. J., & Dunne, T. (2002). Landslides on coastal sage-scrub and grassland hillslopes in a severe El Niño winter: The effects of vegetation conversion on sediment delivery. *GSA Bulletin*, *114*(8), 983–990. https://doi.org/10.1130/0016-7606(2002)114<0983:LOCSSA>2.0.CO;2

Gabet, E. J., & Mudd, S. M. (2010). Bedrock erosion by root fracture and tree throw: A coupled biogeomorphic model to explore the humped soil production function and the persistence of hillslope soils. *Journal of Geophysical Research: Earth Surface*, *115*(F4). https://doi.org/10.1029/2009JF001526

Gabet, E. J., Reichman, O. J., & Seabloom, E. W. (2003). The Effects of Bioturbation on Soil Processes and Sediment Transport. *Annual Review of Earth and Planetary Sciences*, *31*(1), 249–273. https://doi.org/10.1146/annurev.earth.31.100901.141314

Ge, S., Lin, G., Amelung, F., Okubo, P. G., Swanson, D. A., & Yunjun, Z. (2019). The Accommodation of the South Flank's Motion by the Koa'e Fault System, Kīlauea, Hawai'i: Insights From the June 2012 Earthquake Sequence. *Journal of Geophysical Research: Solid Earth*, *124*(11), 11116–11129. https://doi.org/10.1029/2018JB016961

Giaccio, B., Galli, P., Messina, P., Peronace, E., Scardia, G., Sottili, G., et al. (2012). Fault and basin depocentre migration over the last 2 Ma in the L'Aquila 2009 earthquake region, central Italian Apennines. *Quaternary Science Reviews*, *56*, 69–88. https://doi.org/10.1016/j.quascirev.2012.08.016

Giano, S. I., Danese, M., Gioia, D., Pescatore, E., Siervo, V., & Bentivenga, M. (2020). Tools for Semi-automated Landform Classification: A Comparison in the Basilicata Region (Southern Italy). In O. Gervasi, B. Murgante, S. Misra, C. Garau, I. Blečić, D. Taniar, et al. (Eds.), *Computational Science and Its Applications – ICCSA 2020* (Vol. 12250, pp. 709–722). Cham: Springer International Publishing. https://doi.org/10.1007/978-3-030-58802-1_51

Gioia, D., Danese, M., Bentivenga, M., Pescatore, E., Siervo, V., & Giano, S. I. (2020). Comparison of Different Methods of Automated Landform Classification at the Drainage Basin Scale: Examples from the Southern Italy. In O. Gervasi, B. Murgante, S. Misra, C. Garau, I. Blečić, D. Taniar, et al. (Eds.), *Computational Science and Its Applications – ICCSA 2020* (Vol. 12250, pp. 696–708). Cham: Springer International Publishing. https://doi.org/10.1007/978-3-030-58802-1_50

Golub, G. H., & Reinsch, C. (1970). Singular value decomposition and least squares solutions. *Numerische Mathematik*, *14*(5), 403–420. https://doi.org/10.1007/BF02163027

Golub, Gene H., & Van Loan, C. F. (2013). *Matrix computations* (Fourth edition). Baltimore: The Johns Hopkins University Press.

Gomez-Pazo, A., Naylor, L., & Hurst, M. D. (2022). *Semi-automated methods for analysing the parameters that controlling shore platform evolution: the example of Glamorgan, South Wales* (No. ICG2022-528). Presented at the ICG2022, Copernicus Meetings. https://doi.org/10.5194/icg2022-528

Grant, J. V., & Kattenhorn, S. A. (2004). Evolution of vertical faults at an extensional plate boundary, southwest Iceland. *Journal of Structural Geology*, *26*(3), 537–557. https://doi.org/10.1016/j.jsg.2003.07.003

Gu, J., Yu, P., Lu, X., & Ding, W. (2021). Leaf species recognition based on VGG16 networks and transfer learning. In *2021 IEEE 5th Advanced Information Technology, Electronic and Automation Control Conference (IAEAC)* (Vol. 5, pp. 2189–2193). https://doi.org/10.1109/IAEAC50856.2021.9390789

Gudmundsson, A. (1992). Formation and growth of normal faults at the divergent plate boundary in Iceland. *Terra Nova*, *4*(4), 464–471. https://doi.org/10.1111/j.1365-3121.1992.tb00582.x

Guillon, H., Byrne, C. F., Lane, B. A., Sandoval Solis, S., & Pasternack, G. B. (2020). Machine Learning Predicts Reach-Scale Channel Types From Coarse-Scale Geospatial Data in a Large River Basin. *Water Resources Research*, *56*(3). https://doi.org/10.1029/2019WR026691

Hammond, E. H. (1954). Small-Scale Continental Landform Maps. *Annals of the Association of American Geographers*, *44*(1), 33–42. https://doi.org/10.1080/00045605409352120

Hanks, T. C. (2000). The age of scarplike landforms from diffusion-equation analysis, *4*, 313–338. https://doi.org/10.1029/RF004p0313

Hanks, T. C., & Andrews, D. J. (1989). Effect of far-field slope on morphologic dating of scarplike landforms. *Journal of Geophysical Research*, *94*(B1), 565. https://doi.org/10.1029/JB094iB01p00565

Hanks, T. C., Bucknam, R. C., Lajoie, K. R., & Wallace, R. E. (1984). Modification of wave-cut and faulting-controlled landforms. *Journal of Geophysical Research: Solid Earth*, *89*(B7), 5771–5790. https://doi.org/10.1029/JB089iB07p05771

Hardy, S. (2013). Propagation of blind normal faults to the surface in basaltic sequences: Insights from 2D discrete element modelling. *Marine and Petroleum Geology*, *48*, 149–159. https://doi.org/10.1016/j.marpetgeo.2013.08.012

Hastie, T., & Tibshirani, R. (1998). Classification by pairwise coupling. *The Annals of Statistics*, *26*(2). https://doi.org/10.1214/aos/1028144844

He, H., Wei, Z., & Densmore, A. (2016). Quantitative morphology of bedrock fault surfaces and identification of paleo-earthquakes. *Tectonophysics*, *693*, 22–31. https://doi.org/10.1016/j.tecto.2016.09.032

Hengl, T., & Rossiter, D. G. (2003). Supervised Landform Classification to Enhance and Replace Photo-Interpretation in Semi-Detailed Soil Survey. *Soil Science Society of America Journal*, *67*(6), 1810–1822. https://doi.org/10.2136/sssaj2003.1810

Hibert, C., Mangeney, A., Grandjean, G., Baillard, C., Rivet, D., Shapiro, N. M., et al. (2014). Automated identification, location, and volume estimation of rockfalls at Piton de la Fournaise volcano. *Journal of Geophysical Research: Earth Surface*, *119*(5), 1082–1105. https://doi.org/10.1002/2013JF002970

Hildreth, W., & Wilson, C. J. N. (2007). Compositional Zoning of the Bishop Tuff. *Journal of Petrology*, *48*(5), 951–999. https://doi.org/10.1093/petrology/egm007

Hilley, G. E., DeLong, S., Prentice, C., Blisniuk, K., & Arrowsmith, Jr. (2010). Morphologic dating of fault scarps using airborne laser swath mapping (ALSM) data: SCARP DATING FOR THE 21ST CENTURY. *Geophysical Research Letters*, *37*(4). https://doi.org/10.1029/2009GL042044

Hilley, George E., & Arrowsmith, J. R. (2008). Geomorphic response to uplift along the Dragon's Back pressure ridge, Carrizo Plain, California. *Geology*, *36*(5), 367–370. https://doi.org/10.1130/G24517A.1

Hilley, George E., Arrowsmith, J. R., & Amoroso, L. (2001). Interaction between normal faults and fractures and fault scarp morphology. *Geophysical Research Letters*, *28*(19), 3777–3780. https://doi.org/10.1029/2001GL012876

Hobbs, K. M., & Parrish, J. T. (2016). Miocene global change recorded in Columbia River basalt–hosted paleosols. *GSA Bulletin*, *128*(9–10), 1543–1554. https://doi.org/10.1130/B31437.1

Hodge, M., Biggs, J., Fagereng, Å., Elliott, A., Mdala, H., & Mphepo, F. (2019). A semi-automated algorithm to quantify scarp morphology (SPARTA): application to normal faults in southern Malawi. *Solid Earth*, *10*(1), 27–57. https://doi.org/10.5194/se-10-27-2019

Holland, M., Urai, J. L., & Martel, S. (2006). The internal structure of fault zones in basaltic sequences. *Earth and Planetary Science Letters*, *248*(1), 301–315. https://doi.org/10.1016/j.epsl.2006.05.035

Holtmann, R., Cattin, R., Simoes, M., & Steer, P. (2023). *Revealing the hidden signature of fault slip history in the morphology of degrading scarps* (preprint). In Review. https://doi.org/10.21203/rs.3.rs-2495215/v1

Hon, K., Kauahikaua, J., Denlinger, R. P., & MacKay, K. (1994). Emplacement and inflation of pahoehoe sheet flows: Observations and measurements of active lava flows on Kilauea Volcano, Hawaii. *GSA Bulletin*, *106*(3), 351–370. https://doi.org/10.1130/0016-7606(1994)106<0351:EAIOPS>2.3.CO;2

Hornsby, K. T., Streig, A. R., Bennett, S. E. K., Chang, J. C., & Mahan, S. (2019). Neotectonic and Paleoseismic Analysis of the Northwest Extent of Holocene Surface Deformation along the Meers Fault, Oklahoma. *Bulletin of the Seismological Society of America*, *110*(1), 49–66. https://doi.org/10.1785/0120180148

Hsu, C.-H., & Chen, C.-C. (2007). SVD-based projection for face recognition. In *2007 IEEE International Conference on Electro/Information Technology* (pp. 600–603). https://doi.org/10.1109/EIT.2007.4374514

Huete, A., Didan, K., Miura, T., Rodriguez, E. P., Gao, X., & Ferreira, L. G. (2002). Overview of the radiometric and biophysical performance of the MODIS vegetation indices.

Remote Sensing of Environment, *83*(1–2), 195–213. https://doi.org/10.1016/S0034-4257(02)00096-2

Hughes, A., Escartín, J., Olive, J., Billant, J., Deplus, C., Feuillet, N., et al. (2021). Quantification of Gravitational Mass Wasting and Controls on Submarine Scarp Morphology Along the Roseau Fault, Lesser Antilles. *Journal of Geophysical Research: Earth Surface*, *126*(4). https://doi.org/10.1029/2020JF005892

Hungr, O., Leroueil, S., & Picarelli, L. (2014). The Varnes classification of landslide types, an update. *Landslides*, *11*(2), 167–194. https://doi.org/10.1007/s10346-013-0436-y

Irvin, B. J., Ventura, S. J., & Slater, B. K. (1997). Fuzzy and isodata classification of landform elements from digital terrain data in Pleasant Valley, Wisconsin. *Geoderma*, *77*(2–4), 137–154. https://doi.org/10.1016/S0016-7061(97)00019-0

Islam, Md. T., Sturkell, E., LaFemina, P., Geirsson, H., Sigmundsson, F., & Ólafsson, H. (2016). Continuous subsidence in the Thingvellir rift graben, Iceland: Geodetic observations since 1967 compared to rheological models of plate spreading. *Journal of Geophysical Research: Solid Earth*, *121*(1), 321–338. https://doi.org/10.1002/2015JB012306

Iwahashi, J., & Pike, R. J. (2007). Automated classifications of topography from DEMs by an unsupervised nested-means algorithm and a three-part geometric signature. *Geomorphology*, *86*(3–4), 409–440. https://doi.org/10.1016/j.geomorph.2006.09.012

Jackson, G., & Sheldon, J. (1949). The Vegetation of Magnesian Limestone Cliffs at Markland Grips Near Sheffield. *Journal of Ecology*, *37*(1), 38–50. https://doi.org/10.2307/2256729

Jackson, T. A., & Keller, W. D. (1970). A comparative study of the role of lichens and "inorganic" processes in the chemical weathering of Recent Hawaiian lava flows. *American Journal of Science*, *269*(5), 446–466. https://doi.org/10.2475/ajs.269.5.446

Jackson, Togwell A. (2015). Weathering, secondary mineral genesis, and soil formation caused by lichens and mosses growing on granitic gneiss in a boreal forest environment. *Geoderma*, *251–252*, 78–91. https://doi.org/10.1016/j.geoderma.2015.03.012

Jasiewicz, J., & Stepinski, T. F. (2013). Geomorphons — a pattern recognition approach to classification and mapping of landforms. *Geomorphology*, *182*, 147–156. https://doi.org/10.1016/j.geomorph.2012.11.005

Jiang, Z. (2019). A Novel Crop Weed Recognition Method Based on Transfer Learning from VGG16 Implemented by Keras. *IOP Conference Series: Materials Science and Engineering*, *677*(3), 032073. https://doi.org/10.1088/1757-899X/677/3/032073

Kappus, M. E., & Vernon, F. L. (1991). Acoustic signature of thunder from seismic records. *Journal of Geophysical Research: Atmospheres*, *96*(D6), 10989–11006. https://doi.org/10.1029/91JD00789

Karamitros, I., Ganas, A., Chatzipetros, A., & Valkaniotis, S. (2020). Non-planarity, scale-dependent roughness and kinematic properties of the Pidima active normal fault scarp (Messinia, Greece) using high-resolution terrestrial LiDAR data. *Journal of Structural Geology*, *136*, 104065. https://doi.org/10.1016/j.jsg.2020.104065

Kaven, J. O., & Martel, S. J. (2007). Growth of surface-breaching normal faults as a three-dimensional fracturing process. *Journal of Structural Geology*, *29*(9), 1463–1476. https://doi.org/10.1016/j.jsg.2007.05.007

Kazemi Garajeh, M., Feizizadeh, B., Weng, Q., Rezaei Moghaddam, M. H., & Kazemi Garajeh, A. (2022). Desert landform detection and mapping using a semi-automated object-based image analysis approach. *Journal of Arid Environments*, *199*, 104721. https://doi.org/10.1016/j.jaridenv.2022.104721

Kelley, M. L., Spiker, E. C., Lipman, P. W., Lockwood, J. P., Holcomb, R. T., & Rubin, M. (1979). US Geological Survey, Reston, Virginia, Radiocarbon Dates XV: Mauna Loa and Kilauea Volcanoes, Hawaii. *Radiocarbon*, *21*(2), 306–320. https://doi.org/10.1017/S0033822200004434

Kettermann, M., Weismüller, C., von Hagke, C., Reicherter, K., & Urai, J. L. (2019). Large near-surface block rotations at normal faults of the Iceland rift: Evolution of tectonic caves and dilatancy. *Geology*, *47*(8), 781–785. https://doi.org/10.1130/G46158.1

Kirkbride, M., & Matthews, D. (1997). The Role of Fluvial and Glacial Erosion in Landscape Evolution: The Ben Ohau Range, New Zealand. *Earth Surface Processes and Landforms*, *22*(3), 317–327. https://doi.org/10.1002/(SICI)1096-9837(199703)22:3<317::AID-ESP760>3.0.CO;2-I

Knerr, S., Personnaz, L., & Dreyfus, G. (1990). Single-layer learning revisited: a stepwise procedure for building and training a neural network. In F. F. Soulié & J. Hérault (Eds.), *Neurocomputing* (pp. 41–50). Berlin, Heidelberg: Springer Berlin Heidelberg. https://doi.org/10.1007/978-3-642-76153-9_5

Ko, T. Y., & Kemeny, J. (2007). Effect of Confining Stress And Loading Rate On Fracture Toughness of Rocks. Presented at the 1st Canada - U.S. Rock Mechanics Symposium, OnePetro. Retrieved from https://onepetro.org/ARMACUSRMS/proceedings-abstract/ARMA07/All-ARMA07/116192

Kodama, K., & Barnes, G. M. (1997). Heavy Rain Events over the South-Facing Slopes of Hawaii: Attendant Conditions. *Weather and Forecasting*, *12*(2), 347–367. https://doi.org/10.1175/1520-0434(1997)012<0347:HREOTS>2.0.CO;2

Korzeniowska, K., Pfeifer, N., & Landtwing, S. (2018). Mapping gullies, dunes, lava fields, and landslides via surface roughness. *Geomorphology*, *301*, 53–67. https://doi.org/10.1016/j.geomorph.2017.10.011

Kumar, P. S., Mohanty, R., Lakshmi, K. J. P., Raghukanth, S. T. G., Dabhu, A. C., Rajasekhar, R. P., & Menon, R. (2019). The Seismically Active Lobate Scarps and Coseismic Lunar Boulder Avalanches Triggered by 3 January 1975 (MW 4.1) Shallow Moonquake. *Geophysical Research Letters*, *46*(14), 7972–7981. https://doi.org/10.1029/2019GL083580

Kuriakose, S. L., & van Beek, L. P. H. (2011). Plant Root Strength and Slope Stability. In J. Gliński, J. Horabik, & J. Lipiec (Eds.), *Encyclopedia of Agrophysics* (pp. 622–627). Dordrecht: Springer Netherlands. https://doi.org/10.1007/978-90-481-3585-1_222

LaFemina, P. C., Dixon, T. H., Malservisi, R., Árnadóttir, T., Sturkell, E., Sigmundsson, F., & Einarsson, P. (2005). Geodetic GPS measurements in south Iceland: Strain accumulation and partitioning in a propagating ridge system. *Journal of Geophysical Research: Solid Earth*, *110*(B11). https://doi.org/10.1029/2005JB003675

Lamb, M. P., & Dietrich, W. E. (2009). The persistence of waterfalls in fractured rock. *GSA Bulletin*, *121*(7–8), 1123–1134. https://doi.org/10.1130/B26482.1

Lambers, H., Chapin, F. S., & Pons, T. L. (2008). *Plant Physiological Ecology*. New York, NY: Springer New York. https://doi.org/10.1007/978-0-387-78341-3

Larose, E., Carrière, S., Voisin, C., Bottelin, P., Baillet, L., Guéguen, P., et al. (2015). Environmental seismology: What can we learn on earth surface processes with ambient noise? *Journal of Applied Geophysics*, *116*, 62–74. https://doi.org/10.1016/j.jappgeo.2015.02.001

Lin, Z., & Oguchi, T. (2006). DEM analysis on longitudinal and transverse profiles of steep mountainous watersheds. *Geomorphology*, *78*(1–2), 77–89. https://doi.org/10.1016/j.geomorph.2006.01.017

Lipman, P., Sisson, T., Ui, T., Naka, J., & Smith, J. (2002). Ancestral Submarine Growth of Kïlauea Volcano and Instability of its South Flank. *Washington DC American Geophysical Union Geophysical Monograph Series*, *128*. https://doi.org/10.1029/GM128p0161

Lipman, P. W., Lockwood, J. P., Okamura, R. T., Swanson, D. A., & Yamashita, K. M. (1985). *Ground deformation associated with the 1975 magnitude-7.2 earthquake and resulting changes in activity of Kilauea Volcano, Hawaii* (U.S. Geological Survey Professional Paper No. 1276).

Long, P. E., & Wood, B. J. (1986). Structures, textures, and cooling histories of Columbia River basalt flows. *GSA Bulletin*, *97*(9), 1144–1155. https://doi.org/10.1130/0016-7606(1986)97<1144:STACHO>2.0.CO;2

Lott, F. F., Ritter, J. R. R., Al-Qaryouti, M., & Corsmeier, U. (2017). On the Analysis of Wind-Induced Noise in Seismological Recordings: Approaches to Present Wind-Induced Noise as a Function of Wind Speed and Wind Direction. *Pure and Applied Geophysics*, *174*(3), 1453–1470. https://doi.org/10.1007/s00024-017-1477-2

Lueddecke, S. B., Pinter, N., & Gans, P. (1998). Plio-Pleistocene Ash Falls, Sedimentation, and Range-Front Faulting along the White- Inyo Mountains Front, California. *The Journal of Geology*, *106*(4), 511–522. https://doi.org/10.1086/516038

Lutz, S. J., Caskey, S. J., Mildenhall, D. D., Browne, P. R. L., & Johnson, S. D. (2002). Dating sinter deposits in northern Dixie Valley, Nevada - the paleoseismic record and implications for the Dixie Valley geothermal system. In *Twenty-Seventh Workshop on Geothermal Reservoir Engineering*.

Lyle, P. (2000). The eruption environment of multi-tiered columnar basalt lava flows. *Journal of the Geological Society*, *157*(4), 715–722. https://doi.org/10.1144/jgs.157.4.715

Macdonald, G. A. (1957). Faults and monoclines on Kilauea Volcano, Hawaii. *Geological Society of America Bulletin*, *68*(2), 269. https://doi.org/10.1130/0016-7606(1957)68[269:FAMOKV]2.0.CO;2

MacGregor, K. R., Anderson, R. S., & Waddington, E. D. (2009). Numerical modeling of glacial erosion and headwall processes in alpine valleys. *Geomorphology*, *103*(2), 189–204. https://doi.org/10.1016/j.geomorph.2008.04.022

Mackey, B. H., & Quigley, M. C. (2014). Strong proximal earthquakes revealed by cosmogenic 3He dating of prehistoric rockfalls, Christchurch, New Zealand. *Geology*, *42*(11), 975–978. https://doi.org/10.1130/G36149.1

MacMillan, R. A., Pettapiece, W. W., Nolan, S. C., & Goddard, T. W. (2000). A generic procedure for automatically segmenting landforms into landform elements using DEMs, heuristic rules and fuzzy logic. *Fuzzy Sets and Systems*, *113*(1), 81–109. https://doi.org/10.1016/S0165-0114(99)00014-7

MacMillan, R. A., Jones, R. K., & McNabb, D. H. (2004). Defining a hierarchy of spatial entities for environmental analysis and modeling using digital elevation models (DEMs). *Computers, Environment and Urban Systems*, *28*(3), 175–200. https://doi.org/10.1016/S0198-9715(03)00019-X

Martel, S. J., & Langley, J. S. (2006). Propagation of normal faults to the surface in basalt, Koae fault system, Hawaii. *Journal of Structural Geology*, *28*(12), 2123–2143. https://doi.org/10.1016/j.jsg.2005.12.004

Martins, B., Nunes, A., Meira-Castro, A., Lourenço, L., & Hermenegildo, C. (2022). Local Factors Controlling Gully Development in a Mediterranean Environment. *Land*, *11*(2), 204. https://doi.org/10.3390/land11020204

Mason, J., Schneiderwind, S., Pallikarakis, A., Mechernich, S., Papanikolaou, I., & Reicherter, K. (2017). Hanging-wall colluvial cementation along active normal faults. *Quaternary Research*, *88*(1), 39–59. https://doi.org/10.1017/qua.2017.32

Massey, C. I., Olsen, M. J., Wartman, J., Senogles, A., Lukovic, B., Leshchinsky, B. A., et al. (2022). Rockfall Activity Rates Before, During and After the 2010/2011 Canterbury Earthquake Sequence. *Journal of Geophysical Research: Earth Surface*, *127*(3), e2021JF006400. https://doi.org/10.1029/2021JF006400

Mateos, R. M., García-Moreno, I., & Azañón, J. M. (2012). Freeze–thaw cycles and rainfall as triggering factors of mass movements in a warm Mediterranean region: the case of the Tramuntana Range (Majorca, Spain). *Landslides*, *9*(3), 417–432. https://doi.org/10.1007/s10346-011-0290-8

Matsuoka, N., & Sakai, H. (1999). Rockfall activity from an alpine cliff during thawing periods. *Geomorphology*, *28*(3), 309–328. https://doi.org/10.1016/S0169-555X(98)00116-0

Matthews, B. W. (1975). Comparison of the predicted and observed secondary structure of T4 phage lysozyme. *Biochimica et Biophysica Acta (BBA) - Protein Structure*, *405*(2), 442–451. https://doi.org/10.1016/0005-2795(75)90109-9

Mattson, A., & Bruhn, R. L. (2001). Fault slip rates and initiation age based on diffusion equation modeling: Wasatch Fault Zone and eastern Great Basin. *Journal of Geophysical Research: Solid Earth*, *106*(B7), 13739–13750. https://doi.org/10.1029/2001JB900003

McFadden, L. D., Eppes, M. C., Gillespie, A. R., & Hallet, B. (2005). Physical weathering in arid landscapes due to diurnal variation in the direction of solar heating. *Geological Society of America Bulletin*, *117*(1), 161. https://doi.org/10.1130/B25508.1

Melillo, M., Gariano, S. L., Peruccacci, S., Sarro, R., Mateos, R. M., & Brunetti, M. T. (2020). Rainfall and rockfalls in the Canary Islands: assessing a seasonal link. *Natural Hazards and Earth System Sciences*, *20*(8), 2307–2317. https://doi.org/10.5194/nhess-20-2307-2020

Mokarram, M., Pourghasemi, H. R., & Tiefenbacher, J. P. (2022). Identification of morphometric features of alluvial fan and basins in predicting the erosion levels using ANN. *Environmental Earth Sciences*, *81*(3), 95. https://doi.org/10.1007/s12665-022-10219-w

Montgomery-Brown, E. K., Segall, P., & Miklius, A. (2009). Kilauea slow slip events: Identification, source inversions, and relation to seismicity. *Journal of Geophysical Research: Solid Earth*, *114*(B6). https://doi.org/10.1029/2008JB006074

Moody, J. A., & Troutman, B. M. (2002). Characterization of the spatial variability of channel morphology. *Earth Surface Processes and Landforms*, *27*(12), 1251–1266. https://doi.org/10.1002/esp.403

Muller, N., Magaia, L., & Herbst, B. M. (2004). Singular Value Decomposition, Eigenfaces, and 3D Reconstructions. *SIAM Review*, *46*(3), 518–545. https://doi.org/10.1137/S0036144501387517

Murphy, B. P., Johnson, J. P. L., Gasparini, N. M., & Sklar, L. S. (2016). Chemical weathering as a mechanism for the climatic control of bedrock river incision. *Nature*, *532*(7598), 223–227. https://doi.org/10.1038/nature17449

Nash, D. B. (1980). Morphologic Dating of Degraded Normal Fault Scarps. *The Journal of Geology*, *88*(3), 353–360. https://doi.org/10.1086/628513

Navarre-Sitchler, A., Steefel, C. I., Yang, L., Tomutsa, L., & Brantley, S. L. (2009). Evolution of porosity and diffusivity associated with chemical weathering of a basalt clast. *Journal of Geophysical Research: Earth Surface*, *114*(F2). https://doi.org/10.1029/2008JF001060

Neal, C. A., & Lockwood, J. P. (2003). *Geologic Map of the Summit Region of Kilauea Volcano, Hawaii* (Pamphlet). https://doi.org/10.3133/i2759

Obanawa, H., Hayakawa, Y. S., & Matsukura, Y. (2009). Rates of slope decline, talus growth and cliff retreat along the shomyo river in central japan: a space-time substitution approach. *Geografiska Annaler: Series A, Physical Geography*, *91*(4), 269–278. https://doi.org/10.1111/j.1468-0459.2009.00369.x

O'Grady, D. B., Syvitski, J. P. M., Pratson, L. F., & Sarg, J. F. (2000). Categorizing the morphologic variability of siliciclastic passive continental margins. *Geology*, *28*(3), 207. https://doi.org/10.1130/0091-7613(2000)28<207:CTMVOS>2.0.CO;2

Olaya, V. (2009). Chapter 6 Basic Land-Surface Parameters. In *Developments in Soil Science* (Vol. 33, pp. 141–169). Elsevier. https://doi.org/10.1016/S0166-2481(08)00006-8

Othman, A., & Gloaguen, R. (2014). Improving Lithological Mapping by SVM Classification of Spectral and Morphological Features: The Discovery of a New Chromite Body in the Mawat Ophiolite Complex (Kurdistan, NE Iraq). *Remote Sensing*, *6*(8), 6867–6896. https://doi.org/10.3390/rs6086867

Owen, S., Segall, P., Freymueller, J., Miklius, A., & al, et. (1995). Rapid deformation of the south flank of Kilauea volcano, Hawaii. *Science*, *267*(5202), 1328.

Owen, S., Segall, P., Lisowski, M., Miklius, A., Murray, M., Bevis, M., & Foster, J. (2000). January 30, 1997 eruptive event on Kilauea Volcano, Hawaii, as monitored by continuous GPS. *Geophysical Research Letters*, *27*(17), 2757–2760. https://doi.org/10.1029/1999GL008454

Owen, S. E., & Bürgmann, R. (2006). An increment of volcano collapse: Kinematics of the 1975 Kalapana, Hawaii, earthquake. *Journal of Volcanology and Geothermal Research*, *150*(1), 163–185. https://doi.org/10.1016/j.jvolgeores.2005.07.012

Pan, S. J., & Yang, Q. (2010). A Survey on Transfer Learning. *IEEE Transactions on Knowledge and Data Engineering*, *22*(10), 1345–1359. https://doi.org/10.1109/TKDE.2009.191

Pawlik, Ł. (2013). The role of trees in the geomorphic system of forested hillslopes — A review. *Earth-Science Reviews*, *126*, 250–265. https://doi.org/10.1016/j.earscirev.2013.08.007

Pawlik, Ł., Phillips, J. D., & Šamonil, P. (2016). Roots, rock, and regolith: Biomechanical and biochemical weathering by trees and its impact on hillslopes—A critical literature review. *Earth-Science Reviews*, *159*, 142–159. https://doi.org/10.1016/j.earscirev.2016.06.002

Peacock, D. C. P., & Parfitt, E. A. (2002). Active relay ramps and normal fault propagation on Kilauea Volcano, Hawaii. *Journal of Structural Geology*, *24*(4), 729–742. https://doi.org/10.1016/S0191-8141(01)00109-2

Peacock, D. C. P., & Sanderson, D. J. (1994). Geometry and Development of Relay Ramps in Normal Fault Systems. *AAPG Bulletin*, *78*(2), 147–165. https://doi.org/10.1306/BDFF9046-1718-11D7-8645000102C1865D

Pearthree, P. A. (1990). *Geomorphic analyses of young faulting and fault behavior in central Nevada* (Ph.D.). The University of Arizona, United States -- Arizona. Retrieved from https://www.proquest.com/docview/303816649/abstract/28ABD8B50AAB4DECPQ/1

Pelletier, J. D., DeLong, S. B., Al-Suwaidi, A. H., Cline, M., Lewis, Y., Psillas, J. L., & Yanites, B. (2006). Evolution of the Bonneville shoreline scarp in west-central Utah: Comparison of scarp-analysis methods and implications for the diffusion model of hillslope evolution. *Geomorphology*, *74*(1), 257–270. https://doi.org/10.1016/j.geomorph.2005.08.008

Pender, D., & Karunarathna, H. (2013). A statistical-process based approach for modelling beach profile variability. *Coastal Engineering*, *81*, 19–29. https://doi.org/10.1016/j.coastaleng.2013.06.006

Pennock, D. J., Zebarth, B. J., & De Jong, E. (1987). Landform classification and soil distribution in hummocky terrain, Saskatchewan, Canada. *Geoderma*, *40*(3–4), 297–315. https://doi.org/10.1016/0016-7061(87)90040-1

Pérez, F. L. (1985). Surficial Talus Movement in an Andean Paramo of Venezuela. *Geografiska Annaler: Series A, Physical Geography*, *67*(3–4), 221–237. https://doi.org/10.1080/04353676.1985.11880148

Pezzopane, S. K., & Weldon, R. J. (1993). Tectonic role of active faulting in central Oregon. *Tectonics*, *12*(5), 1140–1169. https://doi.org/10.1029/92TC02950

Phillips, F. M., & Majkowski, L. (2011). The role of low-angle normal faulting in active tectonics of the northern Owens Valley, California. *Lithosphere*, *3*(1), 22–36. https://doi.org/10.1130/L73.1

Pinter, N., & Keller, E. A. (1995). Geomorphological analysis of neotectonic deformation, northern Owens Valley, California. *Geologische Rundschau*, *84*(1), 200–212. https://doi.org/10.1007/BF00192251

Pinzuti, P., Mignan, A., & King, G. C. P. (2010). Surface morphology of active normal faults in hard rock: Implications for the mechanics of the Asal Rift, Djibouti. *Earth and Planetary Science Letters*, *299*(1–2), 169–179. https://doi.org/10.1016/j.epsl.2010.08.032

Podolsky, D. M. W., & Roberts, G. P. (2008). Growth of the volcano-flank Koa'e fault system, Hawaii. *Journal of Structural Geology*, *30*(10), 1254–1263. https://doi.org/10.1016/j.jsg.2008.06.006

Raschka, S. (2018). Model Evaluation, Model Selection, and Algorithm Selection in Machine Learning. https://doi.org/10.48550/ARXIV.1811.12808

Raška, P., & Oršulák, T. (2009). Biogeomorphic effects of trees on rock-mantled slopes: searching for dynamic equilibrium. *Geograficky Casopis*, *61*, 19–28.

Rasmussen, C., Dahlgren, R. A., & Southard, R. J. (2010). Basalt weathering and pedogenesis across an environmental gradient in the southern Cascade Range, California, USA. *Geoderma*, *154*(3–4), 473–485. https://doi.org/10.1016/j.geoderma.2009.05.019

Riley, C. M., Diehl, J. F., Kirschvink, J. L., & Ripperdan, R. L. (1999). Paleomagnetic constraints on fault motion in the Hilina Fault System, south flank of Kilauea Volcano, Hawaii. *Journal of Volcanology and Geothermal Research*, *94*(1), 233–249. https://doi.org/10.1016/S0377-0273(99)00105-5

Rodriguez, A. B., Anderson, J. B., Siringan, F. P., & Taviani, M. (2004). Holocene Evolution of the East Texas Coast and Inner Continental Shelf: Along-Strike Variability in Coastal Retreat Rates. *Journal of Sedimentary Research*, *74*(3), 405–421. https://doi.org/10.1306/092403740405

Roering, J. J., Kirchner, J. W., & Dietrich, W. E. (1999). Evidence for nonlinear, diffusive sediment transport on hillslopes and implications for landscape morphology. *Water Resources Research*, *35*(3), 853–870. https://doi.org/10.1029/1998WR900090

Roering, J. J., Schmidt, K. M., Stock, J. D., Dietrich, W. E., & Montgomery, D. R. (2003). Shallow landsliding, root reinforcement, and the spatial distribution of trees in the Oregon Coast Range. *Canadian Geotechnical Journal*, *40*(2), 237–253. https://doi.org/10.1139/t02-113

Rood, D. H., Amidon, W. H., McKeon, R. E., Baldwin, J. N., Gray, B., Page, W. D., & Farley, K. A. (2015). Paleoseismic assessment of the Hat Creek fault using cosmogenic He-3 surface exposure dating in basalt, northeastern California: A proof of concept study, *2015*, T42A-01. Presented at the AGU Fall Meeting Abstracts.

Rowland, J. V., Baker, E., Ebinger, C. J., Keir, D., Kidane, T., Biggs, J., et al. (2007). Fault growth at a nascent slow-spreading ridge: 2005 Dabbahu rifting episode, Afar. *Geophysical Journal International*, *171*(3), 1226–1246. https://doi.org/10.1111/j.1365-246X.2007.03584.x

Rowland, S. K., & Walker, G. P. L. (1988). Mafic-crystal distributions, viscosities, and lava structures of some Hawaiian lava flows. *Journal of Volcanology and Geothermal Research*, *35*(1), 55–66. https://doi.org/10.1016/0377-0273(88)90005-4

Sæmundsson, K., Sigurgeirsson, M. Á., & Friðleifsson, G. Ó. (2020). Geology and structure of the Reykjanes volcanic system, Iceland. *Journal of Volcanology and Geothermal Research*, *391*, 106501. https://doi.org/10.1016/j.jvolgeores.2018.11.022

Safran, E. B., Anderson, S. W., Mills-Novoa, M., House, P. K., & Ely, L. (2011). Controls on large landslide distribution and implications for the geomorphic evolution of the southern interior Columbia River basin. *GSA Bulletin*, *123*(9–10), 1851–1862. https://doi.org/10.1130/B30061.1

Sare, R., Hilley, G. E., & DeLong, S. B. (2019). Regional-Scale Detection of Fault Scarps and Other Tectonic Landforms: Examples From Northern California. *Journal of Geophysical Research: Solid Earth*, *124*(1), 1016–1035. https://doi.org/10.1029/2018JB016886

Sarro, R., Riquelme, A., García-Davalillo, J. C., Mateos, R. M., Tomás, R., Pastor, J. L., et al. (2018). Rockfall Simulation Based on UAV Photogrammetry Data Obtained during an Emergency Declaration: Application at a Cultural Heritage Site. *Remote Sensing*, *10*(12), 1923. https://doi.org/10.3390/rs10121923

Sass, O., & Krautblatter, M. (2007). Debris flow-dominated and rockfall-dominated talus slopes: Genetic models derived from GPR measurements. *Geomorphology*, *86*(1), 176–192. https://doi.org/10.1016/j.geomorph.2006.08.012

Scarciglia, F., Marsico, A., & Capolongo, D. (2022). Weathering processes and rates of scarp retreat in a Mediterranean mountain environment: A multi-analytical approach from terrestrial laser scanning to microscale surveys. *Geomorphology*, *413*, 108356. https://doi.org/10.1016/j.geomorph.2022.108356

Schwartz, D. M., Harpp, K., Kurz, M. D., Wilson, E., & Van Kirk, R. (2022). Low-volume magmatism linked to flank deformation on Isla Santa Cruz, Galápagos Archipelago, using cosmogenic 3He exposure and 40Ar/39Ar dating of fault scarps and lavas. *Bulletin of Volcanology*, *84*(9), 82. https://doi.org/10.1007/s00445-022-01575-3

Scott, C. P., Giampietro, T., Brigham, C., Leclerc, F., Manighetti, I., Arrowsmith, J. R., et al. (2022). Semiautomatic Algorithm to Map Tectonic Faults and Measure Scarp Height

from Topography Applied to the Volcanic Tablelands and the Hurricane Fault, Western US. *Lithosphere*, *2021*(Special 2), 9031662. https://doi.org/10.2113/2021/9031662

Self, S., Keszthelyi, L., & Thordarson, T. (1998). The importance of pāhoehoe. *Annual Review of Earth and Planetary Sciences*, *26*, 81–110. https://doi-org.offcampus.lib.washington.edu/10.1146/annurev.earth.26.1.81

Senthil Kumar, P., Krishna, N., Prasanna Lakshmi, K. J., Raghukanth, S. T. G., Dhabu, A., & Platz, T. (2019). Recent seismicity in Valles Marineris, Mars: Insights from young faults, landslides, boulder falls and possible mud volcanoes. *Earth and Planetary Science Letters*, *505*, 51–64. https://doi.org/10.1016/j.epsl.2018.10.008

Sheldon, N. D. (2003). Pedogenesis and geochemical alteration of the Picture Gorge subgroup, Columbia River basalt, Oregon. *GSA Bulletin*, *115*(11), 1377–1387. https://doi.org/10.1130/B25223.1

Sherrod, D. R., Sinton, J. M., Watkins, S. E., & Brunt, K. M. (2021). Geologic map of the State of Hawai‘i: U.S. Geological Survey Scientific Investigations Map 3143. https://doi.org/10.3133/sim3143

Simonyan, K., & Zisserman, A. (2015). Very Deep Convolutional Networks for Large-Scale Image Recognition. arXiv. Retrieved from http://arxiv.org/abs/1409.1556

Simpson, R. H. (1952). Evolution of the Kona Storm, a subtropical cyclone. *Journal of the Atmospheric Sciences*, *9*(1), 24–35. https://doi.org/10.1175/1520-0469(1952)009<0024:EOTKSA>2.0.CO;2

Sinton, J., Grönvold, K., & Sæmundsson, K. (2005). Postglacial eruptive history of the Western Volcanic Zone, Iceland. *Geochemistry, Geophysics, Geosystems*, *6*(12). https://doi.org/10.1029/2005GC001021

Sirovich, L., & Kirby, M. (1987). Low-dimensional procedure for the characterization of human faces. *Journal of the Optical Society of America A*, *4*(3), 519. https://doi.org/10.1364/JOSAA.4.000519

Skidmore, A. K. (1990). Terrain position as mapped from a gridded digital elevation model. *International Journal of Geographical Information Systems*, *4*(1), 33–49. https://doi.org/10.1080/02693799008941527

Smart, K. J., & Ferrill, D. A. (2018). Discrete element modeling of extensional fault-related monocline formation. *Journal of Structural Geology*, *115*, 82–90. https://doi.org/10.1016/j.jsg.2018.07.009

Sonnette, L., Angelier, J., Villemin, T., & Bergerat, F. (2010). Faulting and fissuring in active oceanic rift: Surface expression, distribution and tectonic–volcanic interaction in the Thingvellir Fissure Swarm, Iceland. *Journal of Structural Geology*, *32*(4), 407–422. https://doi.org/10.1016/j.jsg.2010.01.003

Spry, A. (1962). The origin of columnar jointing, particularly in basalt flows. *Journal of the Geological Society of Australia*, *8*(2), 191–216. https://doi.org/10.1080/14400956208527873

Srivastava, P., Sangode, S. J., Meshram, D. C., Gudadhe, S. S., Nagaraju, E., Kumar, A., & Venkateshwarlu, M. (2012). Paleoweathering and depositional conditions in the inter-flow sediment units (bole beds) of Deccan Volcanic Province, India: A mineral magnetic approach. *Geoderma*, *177–178*, 90–109. https://doi.org/10.1016/j.geoderma.2012.01.034

Stahl, T., & Tye, A. (2020). Schmidt hammer and terrestrial laser scanning (TLS) used to detect single-event displacements on the Pleasant Valley fault (Nevada, USA). *Earth Surface Processes and Landforms*, *45*(2), 473–483. https://doi.org/10.1002/esp.4748

van Steijn, H., Bertran, P., Francou, B., Texier, J.-P., & Hétu, B. (1995). Models for the genetic and environmental interpretation of stratified slope deposits: Review. *Permafrost and Periglacial Processes*, *6*(2), 125–146. https://doi.org/10.1002/ppp.3430060210

Steven Wesnousky, S. John Caskey, & John W. Bell. (2003). *Recency of Faulting and Neotechtonic Framework in the Dixie Valley Geothermal Field and Other Geothermal Fields of the Basin and Range* (No. DOE/ID/13620, 808727) (p. DOE/ID/13620, 808727). https://doi.org/10.2172/808727

Stewart, I. (1996). A rough guide to limestone fault scarps. *Journal of Structural Geology*, *18*(10), 1259–1264. https://doi.org/10.1016/S0191-8141(96)00049-1

Stewart, I. S., & Hancock, P. L. (1990). What is a fault scarp? *Episodes*, *13*(4), 256–263. https://doi.org/10.18814/epiiugs/1990/v13i4/005

Stoddart, D. (2013). *Process and Form in Geomorphology* (1st ed.). Routledge. https://doi.org/10.4324/9780203769850

Strecker, M. R., Blisniuk, P. M., & Eisbacher, G. H. (1990). Rotation of extension direction in the central Kenya Rift. *Geology*, *18*(4), 299. https://doi.org/10.1130/0091-7613(1990)018<0299:ROEDIT>2.3.CO;2

Swanson, D. A., Fiske, R. S., Thornber, C. R., & Poland, M. P. (2018). Dikes in the Koa ʻe fault system, and the Koa ʻe–east rift zone structural grain at Kīlauea Volcano, Hawai ʻi. *Field Volcanology: A Tribute to the Distinguished Career of Don Swanson: Geological Society of America Special Paper*, *538*, 247–274.

Swasono, D. I., Tjandrasa, H., & Fathicah, C. (2019). Classification of Tobacco Leaf Pests Using VGG16 Transfer Learning. In *2019 12th International Conference on Information & Communication Technology and System (ICTS)* (pp. 176–181). https://doi.org/10.1109/ICTS.2019.8850946

Syracuse, E. M., Thurber, C. H., Wolfe, C. J., Okubo, P. G., Foster, J. H., & Brooks, B. A. (2010). High-resolution locations of triggered earthquakes and tomographic imaging of Kilauea Volcano's south flank. *Journal of Geophysical Research: Solid Earth*, *115*(B10). https://doi.org/10.1029/2010JB007554

Tabachnick, B. G., & Fidell, L. S. (2001). *Computer-assisted research design and analysis*. Boston: Allyn and Bacon.

Tangari, A. C., Scarciglia, F., Piluso, E., Marinangeli, L., & Pompilio, L. (2018). Role of weathering of pillow basalt, pyroclastic input and geomorphic processes on the genesis of the Monte Cerviero upland soils (Calabria, Italy). *CATENA*, *171*, 299–315. https://doi.org/10.1016/j.catena.2018.07.015

Taylor, L. L., Leake, J. R., Quirk, J., Hardy, K., Banwart, S. A., & Beerling, D. J. (2009). Biological weathering and the long-term carbon cycle: integrating mycorrhizal evolution and function into the current paradigm. *Geobiology*, *7*(2), 171–191. https://doi.org/10.1111/j.1472-4669.2009.00194.x

Teanby, N., Laj, C., Gubbins, D., & Pringle, M. (2002). A detailed palaeointensity and inclination record from drill core SOH1 on Hawaii. *Physics of the Earth and Planetary Interiors*, *131*(2), 101–140. https://doi.org/10.1016/S0031-9201(02)00032-8

Tesson, J., & Benedetti, L. (2019). Seismic history from in situ 36Cl cosmogenic nuclide data on limestone fault scarps using Bayesian reversible jump Markov chain Monte Carlo. *Quaternary Geochronology*, *52*, 1–20. https://doi.org/10.1016/j.quageo.2019.02.004

Thompson, G. A., & Burke, D. B. (1973). Rate and Direction of Spreading in Dixie Valley, Basin and Range Province, Nevada. *GSA Bulletin*, *84*(2), 627–632. https://doi.org/10.1130/0016-7606(1973)84<627:RADOSI>2.0.CO;2

Trucco, E., & Verri, A. (1998). *Introductory techniques for 3-D computer vision*. Upper Saddle River, NJ: Prentice Hall.

Trudgill, B., & Cartwright, J. (1994). Relay-ramp forms and normal-fault linkages, Canyonlands National Park, Utah. *GSA Bulletin*, *106*(9), 1143–1157. https://doi.org/10.1130/0016-7606(1994)106<1143:RRFANF>2.3.CO;2

Tucker, G. E., & Bradley, D. N. (2010). Trouble with diffusion: Reassessing hillslope erosion laws with a particle-based model. *Journal of Geophysical Research: Earth Surface*, *115*(F1). https://doi.org/10.1029/2009JF001264

Tucker, G. E., McCoy, S. W., Whittaker, A. C., Roberts, G. P., Lancaster, S. T., & Phillips, R. (2011). Geomorphic significance of postglacial bedrock scarps on normal-fault footwalls. *Journal of Geophysical Research: Earth Surface*, *116*(F1), n/a-n/a. https://doi.org/10.1029/2010JF001861

Tuğrul, A. (2004). The effect of weathering on pore geometry and compressive strength of selected rock types from Turkey. *Engineering Geology*, *75*(3), 215–227. https://doi.org/10.1016/j.enggeo.2004.05.008

Turk, M., & Pentland, A. (1991). Eigenfaces for Recognition. *Journal of Cognitive Neuroscience*, *3*(1), 71–86. https://doi.org/10.1162/jocn.1991.3.1.71

Turowski, J. M., Dietze, M., Schöpa, A., Burtin, A., & Hovius, N. (2016). Vom Flüstern, Raunen und Grollen der Landschaft : Seismische Methoden in der Geomorphologie. *System Erde; 6*. https://doi.org/10.2312/GFZ.SYSERDE.06.01.9

Vadman, M. J., & Bemis, S. P. (2019). Active fault mapping and reconnaissance paleoseismic investigations in the La Pine graben, Oregon Cascades, USA. *Geomorphology*, *326*, 6–16. https://doi.org/10.1016/j.geomorph.2018.10.003

Vega-Ramírez, L. A., Spelz, R. M., Negrete-Aranda, R., Neumann, F., Caress, D. W., Clague, D. A., et al. (2021). A New Method for Fault-Scarp Detection Using Linear Discriminant Analysis in High-Resolution Bathymetry Data From the Alarcón Rise and Pescadero Basin. *Tectonics*, *40*(12), e2021TC006925. https://doi.org/10.1029/2021TC006925

Villemin, T., & Bergerat, F. (2013). From surface fault traces to a fault growth model: The Vogar Fissure Swarm of the Reykjanes Peninsula, Southwest Iceland. *Journal of Structural Geology*, *51*, 38–51. https://doi.org/10.1016/j.jsg.2013.03.010

Villemin, T., Bergerat, F., Angelier, J., & Lacasse, C. (1994). Brittle deformation and fracture patterns on oceanic rift shoulders: the esja peninsula, SW Iceland. *Journal of Structural Geology*, *16*(12), 1641–1654. https://doi.org/10.1016/0191-8141(94)90132-5

Vitousek, P. M., & Chadwick, O. A. (2013). Pedogenic Thresholds and Soil Process Domains in Basalt-Derived Soils. *Ecosystems*, *16*(8), 1379–1395. https://doi.org/10.1007/s10021-013-9690-z

Walker, S. J., Wilkinson, S. N., Van Dijk, A. I. J. M., & Hairsine, P. B. (2020). A multi-resolution method to map and identify locations of future gully and channel incision. *Geomorphology*, *358*, 107115. https://doi.org/10.1016/j.geomorph.2020.107115

Wallace, R. E. (1977). Profiles and ages of young fault scarps, north-central Nevada. *Geological Society of America Bulletin*, *88*(9), 1267. https://doi.org/10.1130/0016-7606(1977)88<1267:PAAOYF>2.0.CO;2

Wallace, R. E., & Whitney, R. A. (1984). Late quaternary history of the Stillwater seismic gap, Nevada. *Bulletin of the Seismological Society of America*, *74*(1), 301–314. https://doi.org/10.1785/BSSA0740010301

Watters, T. R., Daud, K., Banks, M. E., Selvans, M. M., Chapman, C. R., & Ernst, C. M. (2016). Recent tectonic activity on Mercury revealed by small thrust fault scarps. *Nature Geoscience*, *9*(10), 743–747. https://doi.org/10.1038/ngeo2814

Watters, T. R., Weber, R. C., Collins, G. C., Howley, I. J., Schmerr, N. C., & Johnson, C. L. (2019). Shallow seismic activity and young thrust faults on the Moon. *Nature Geoscience*, *12*(6), 411–417. https://doi.org/10.1038/s41561-019-0362-2

Wedmore, L. N. J., Biggs, J., Williams, J. N., Fagereng, Å., Dulanya, Z., Mphepo, F., & Mdala, H. (2020). Active Fault Scarps in Southern Malawi and Their Implications for the Distribution of Strain in Incipient Continental Rifts. *Tectonics*, *39*(3), e2019TC005834. https://doi.org/10.1029/2019TC005834

Weismüller, C., Urai, J. L., Kettermann, M., von Hagke, C., & Reicherter, K. (2019). Structure of massively dilatant faults in Iceland: lessons learned from high-resolution unmanned aerial vehicle data. *Solid Earth*, *10*(5), 1757–1784. https://doi.org/10.5194/se-10-1757-2019

Westoby, M. J., Brasington, J., Glasser, N. F., Hambrey, M. J., & Reynolds, J. M. (2012). 'Structure-from-Motion' photogrammetry: A low-cost, effective tool for geoscience applications. *Geomorphology*, *179*, 300–314. https://doi.org/10.1016/j.geomorph.2012.08.021

White, I. R., & Crider, J. G. (2006). Extensional fault-propagation folds: mechanical models and observations from the Modoc Plateau, northeastern California. *Journal of Structural Geology*, *28*(7), 1352–1370. https://doi.org/10.1016/j.jsg.2006.03.028

Wiatr, T., Papanikolaou, I., Fernández-Steeger, T., & Reicherter, K. (2015). Bedrock fault scarp history: Insight from t-LiDAR backscatter behaviour and analysis of structure changes. *Geomorphology*, *228*, 421–431. https://doi.org/10.1016/j.geomorph.2014.09.021

Wilkins, A., Subbarao, K. V., Ingram, G., & Walsh, J. N. (1994). Weathering regimes within the Deccan basalts. In K. V. Subbarao (Ed.), *Volcanism* (pp. 217–223). Wiley Eastern Ltd.

Willemse, E. J. M. (1997). Segmented normal faults: Correspondence between three-dimensional mechanical models and field data. *Journal of Geophysical Research: Solid Earth*, *102*(B1), 675–692. https://doi.org/10.1029/96JB01651

Wilson, P. (1990). Clast size variations on talus: Some observations from northwest Ireland. *Earth Surface Processes and Landforms*, *15*(2), 183–188. https://doi.org/10.1002/esp.3290150209

Wolfe, F. D., Stahl, T. A., Villamor, P., & Lukovic, B. (2020). Short communication: A semiautomated method for bulk fault slip analysis from topographic scarp profiles. *Earth Surface Dynamics*, *8*(1), 211–219. https://doi.org/10.5194/esurf-8-211-2020

Wu, J., Liu, H., Wang, Z., Ye, L., Li, M., Peng, Y., et al. (2021). Channel head extraction based on fuzzy unsupervised machine learning method. *Geomorphology*, *391*, 107888. https://doi.org/10.1016/j.geomorph.2021.107888

Wu, Y., Qin, X., Pan, Y., & Yuan, C. (2018). Convolution Neural Network based Transfer Learning for Classification of Flowers. In *2018 IEEE 3rd International Conference on Signal and Image Processing (ICSIP)* (pp. 562–566). https://doi.org/10.1109/SIPROCESS.2018.8600536

Wyss, M., & Koyanagi, R. Y. (1992). Seismic gaps in Hawaii. *Bulletin of the Seismological Society of America*, *82*(3), 1373–1387. https://doi.org/10.1785/BSSA0820031373

Yingkui, L., Gengnian, L., & Zhijiu, C. (2001). Longitudinal variations in cross-section morphology along a glacial valley: a case-study from the Tien Shan, China. *Journal of Glaciology*, *47*(157), 243–250. https://doi.org/10.3189/172756501781832278

Zhu, Y., Dortch, J. M., Massey, M. A., Haneberg, W. C., & Curl, D. (2021). An intelligent swath tool to characterize complex topographic features: Theory and application in the Teton Range, Licking River, and Olympus Mons. *Geomorphology*, *387*, 107778. https://doi.org/10.1016/j.geomorph.2021.107778

Zielke, O., Benedetti, L., Mai, P. M., Fleury, J., Rizza, M., & Viseur, S. (2022). Bedrock fault roughness resolves slip increments of large earthquakes: Case studies from Central Italy. *Tectonophysics*, *838*, 229502. https://doi.org/10.1016/j.tecto.2022.229502

Zou, J., He, H., Yokoyama, Y., Sproson, A. D., Shirahama, Y., Zhou, Y., et al. (2021). Identification of Paleoearthquakes and Coseismic Slips on a Normal Fault Using High-Precision Quantitative Morphology: Application to the Jiaocheng Fault in the Shanxi Rift, China. *Lithosphere*, *2021*(Special 2), 2550879. https://doi.org/10.2113/2021/2550879